OPEN ACCESS
IOP Publishing
Nanotechnology

Nanotechnology **32** (2021) 132004 (60pp)
https://doi.org/10.1088/1361-6528/abcf6d

Topical Review

Perovskite-inspired materials for photovoltaics and beyond—from design to devices

Yi-Teng Huang[1], **Seán R Kavanagh**[2,3,4], **David O Scanlon**[2,4,5], **Aron Walsh**[3,6] and **Robert L Z Hoye**[3]

[1] Department of Physics, University of Cambridge, JJ Thomson Ave, Cambridge CB3 0HE, United Kingdom
[2] Department of Chemistry, University College London, 20 Gordon Street, London WC1H 0AJ, United Kingdom
[3] Department of Materials, Imperial College London, Exhibition Road, London SW7 2AZ, United Kingdom
[4] Thomas Young Centre, University College London, Gower Street, London WC1E 6BT, United Kingdom
[5] Diamond Light Source Ltd., Diamond House, Harwell Science and Innovation Campus, Didcot, Oxfordshire OX11 0DE, United Kingdom
[6] Department of Materials Science and Engineering, Yonsei University, Seoul 120-749, Republic of Korea

E-mail: r.hoye@imperial.ac.uk

Received 29 January 2020, revised 14 October 2020
Accepted for publication 1 December 2020
Published 8 January 2021

Abstract

Lead-halide perovskites have demonstrated astonishing increases in power conversion efficiency in photovoltaics over the last decade. The most efficient perovskite devices now outperform industry-standard multi-crystalline silicon solar cells, despite the fact that perovskites are typically grown at low temperature using simple solution-based methods. However, the toxicity of lead and its ready solubility in water are concerns for widespread implementation. These challenges, alongside the many successes of the perovskites, have motivated significant efforts across multiple disciplines to find lead-free and stable alternatives which could mimic the ability of the perovskites to achieve high performance with low temperature, facile fabrication methods. This Review discusses the computational and experimental approaches that have been taken to discover lead-free perovskite-inspired materials, and the recent successes and challenges in synthesizing these compounds. The atomistic origins of the extraordinary performance exhibited by lead-halide perovskites in photovoltaic devices is discussed, alongside the key challenges in engineering such high-performance in alternative, next-generation materials. Beyond photovoltaics, this Review discusses the impact perovskite-inspired materials have had in spurring efforts to apply new materials in other optoelectronic applications, namely light-emitting diodes, photocatalysts, radiation detectors, thin film transistors and memristors. Finally, the prospects and key challenges faced by the field in advancing the development of perovskite-inspired materials towards realization in commercial devices is discussed.

Keywords: lead-halide perovskites, perovskite-inspired materials, materials discovery, defects, non-radiative recombination, nanocrystals, density functional theory

(Some figures may appear in colour only in the online journal)

1. Introduction

Sunlight is a vast, reliable and ubiquitous source of renewable energy [1]. Each year, terrestrial solar energy amounts to 1500 exawatt-hours [2], whereas global electrical energy demand was only 0.03 exawatt-hours in 2018. Arguably the most promising method to convert solar energy to electricity with no carbon-based by-products is through photovoltaics (PVs) [1]. However, solar energy production only reached 440 terawatt-hours in 2018, with 500 gigawatts of PV capacity installed worldwide by the end of 2018 [1]. Although PV deployment is projected to soon reach the terawatt level [1], it is predicted that 37–180 TW of PV capacity would be needed by 2050 in order to fulfil the ambitions of over 60 nations to achieve net-zero carbon emissions [3].

Numerous technoeconomic analyses have examined the challenges that must be addressed to enable the required scaling of PV capacity, some of which are covered in [1, 3, 4]. Notably, this will require reductions in the levelized cost of electricity (LCOE) and capital-intensity of manufacturing [4], which could be achieved through the use of thin film solar cells, particularly in tandem devices. Tandem solar cells combine two sub-cells which absorb in complementary parts of the solar spectrum, thus surpassing the theoretical limit of a single-junction device. Thin film solar cells are also suitable for integration in buildings (e.g. solar windows), or use indoors to power small standalone gadgets, forming part of the Internet of Things [5].

While thin film PVs have been developed for decades, lead-halide perovskites (LHPs) have recently emerged, demonstrating higher device learning-rates than any other PV material [5]. Since their first report in PVs in 2009 (with 3.8% efficiency [6]), LHP PVs have now reached a certified efficiency of 25.5% (as of the end of 2020) [7] for small area cells, exceeding the efficiency of multi-crystalline silicon and approaching the certified record efficiency of crystalline silicon solar cells (26.7% [7]). Tandems between LHP top-cells and silicon bottom-cells have already reached a certified efficiency of 29.15% after only 6 years of development [8, 9]. The LHP band gap can be easily tuned over a wide range through manipulation of the composition. As a result, perovskite-perovskite tandems have been realized, with 25% efficiency already achieved [10]. Both tandem structures are projected to achieve lower LCOEs than single-junction silicon solar cells [5]. Single-junction perovskite devices have also demonstrated 35.2% efficiency under indoor lighting [11]. Critically, these high efficiencies can be achieved through low-temperature and facile processing, namely solution-processing and thermal evaporation. LHPs therefore hold significant potential for reducing the LCOE and capital-intensity of PVs.

However, there remains debate over whether the toxicity of lead (present in a soluble form in LHPs) could present a barrier to terawatt-scale deployment [12]. In addition, most LHPs are unstable in ambient air. While there has been significant effort to address this, with encapsulated perovskite solar cells now having met industry stability protocols (IEC 61215-1-3:2016) [13], LHPs used on the utility scale would ultimately need to have a field stability exceeding 25 years. More broadly, the success of LHPs defies conventional wisdom regarding the role of defects, in which high efficiencies are achieved despite thin films exhibiting large defect concentrations, several orders of magnitude greater than in traditional silicon or gallium arsenide materials [14]. This prompts the question of how such tolerance to defects arises, and whether this property could be generalized and designed in other classes of materials, especially those composed of abundant, non-toxic elements, and which are stable in air.

Broadly, three strategies have been used to identify perovskite-inspired materials (PIMs): (1) searching for chemically-analogous materials, (2) investigating materials with a perovskite crystal structure, and (3) inverse design of materials based on defect tolerance [15–18]. This effort spans across multiple academic disciplines. The key questions focus not only on structure-mechanism-property relationships of the materials and their performance in devices, but also how computational tools are being developed to accelerate the design and discovery of novel materials for high-performance optoelectronic devices.

In this Topical Review, we bring computational and theoretical research together with experimental efforts to engineer the properties and performance of these materials (figure 1). Our Review begins with a discussion of the high-throughput materials discovery process, alongside the challenges of this research method. Following this, the chemical origins of defect tolerance are explored in detail, before relating these properties to the remarkable photovoltaic performance of LHPs and the inverse design of advanced perovskite-inspired materials (PIMs) that may also achieve defect tolerance. Additionally, a brief introduction to the practical implementation, challenges and frontiers of computational defect investigations is provided. We next discuss the classes of materials that have been considered, their properties, and synthesis methods developed. This is followed by a discussion on the performance of these materials in photovoltaic devices, as well as the opportunities found in using the materials for alternative applications (including light-emitting diodes and radiation detectors). Finally, we discuss the key frontiers and challenges in discovering high-performance PIMs, and the important questions that urgently need to be answered in order to achieve commercial application.

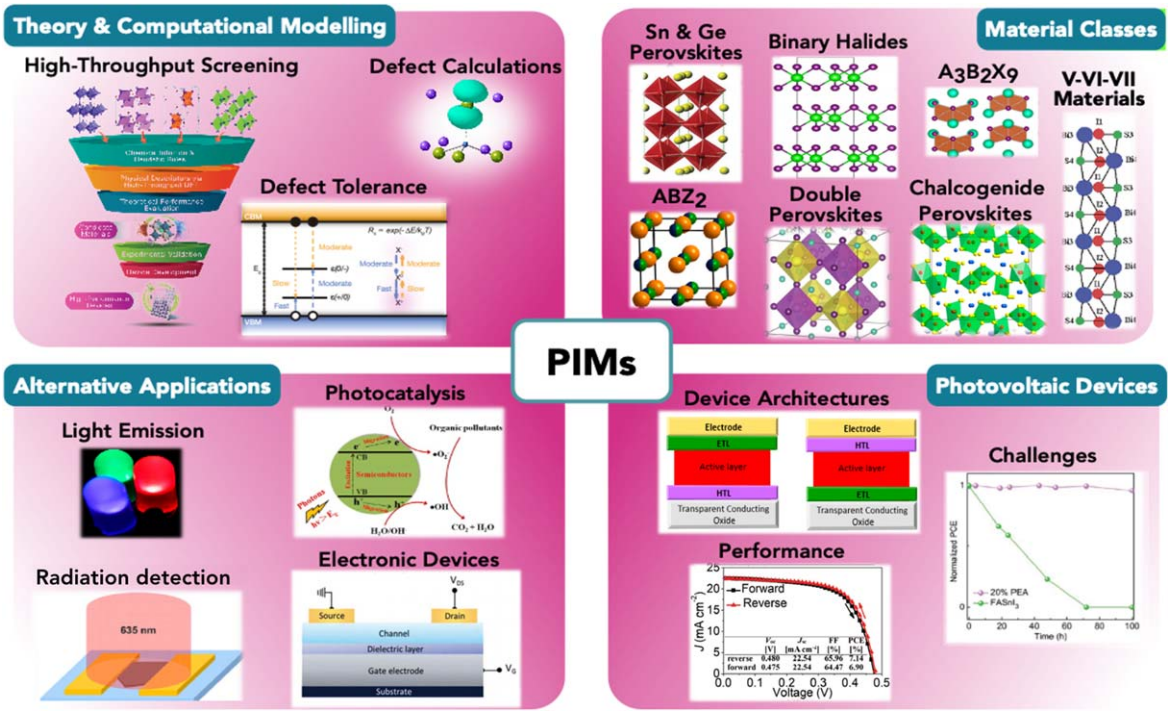

Figure 1. Overview of this Topical Review, which covers computational investigations into defect tolerance and tools developed for the screening of perovskite-inspired materials (PIMs), the properties of the materials developed and how they can be grown, and their applications in photovoltaics and beyond. (Sn and Ge perovskites) [19] John Wiley & Sons. © 2018 WILEY-VCH Verlag GmbH & Co. KGaA, Weinheim. Copyright 2018 Wiley. (Double Perovskites) [20] John Wiley & Sons. © 2019 WILEY-VCH Verlag GmbH & Co. KGaA, Weinheim. Copyright 2019 Wiley. ($A_3B_2X_9$) Reprinted with permission from [21]. Copyright (2018) American Chemical Society. (ABZ_2) Reprinted with permission from [22]. Copyright (2018) American Chemical Society. (Chalcogenide Perovskites) Reprinted with permission from [23]. Copyright (2019) American Chemical Society. (Binary Halides) Reprinted with permission from [24]. Copyright (2020) American Chemical Society. (V–VI–VII Materials) Reprinted from [25], Copyright (2007), with permission from Elsevier. (Performance and Challenges) [19] John Wiley & Sons. © 2018 WILEY-VCH Verlag GmbH & Co. KGaA, Weinheim. Copyright 2019 Wiley. (Photodetection) Reprinted with permission from [26]. Copyright (2018) American Chemical Society. (Photocatalysis) Reprinted from [27], Copyright (2015), with permission from Elsevier.

2. Computational and theoretical approaches to accelerate the discovery of perovskite-inspired materials

2.1. Computational materials discovery

Materials modelling is a rapidly expanding scientific field, most notably in the realm of materials discovery and design, where computational methods have significantly accelerated research efforts [29]. While computational materials science has flourished as a fertile research field since the 1970s, with a rich history of Nobel laureates, rapid technological advancements alongside financial investment have supported a renaissance in this area in recent times. Long-established approximations are no longer necessary and simulation size/time constraints can be overcome, providing the capability to perform increasingly quantitative and realistic calculations. Historically, computer simulations have played a responsive, augmentative role in relation to experiment. However, these recent advances have facilitated the ability of computational predictions to guide experiment, representing a critical component in the efficient discovery of novel high-performance materials.

The fundamental challenge of materials discovery is to identify promising candidate materials (for the specified application) from the near-infinite chemical space of possible compounds. To illustrate the scale of this physical search space, one can simply look at the Inorganic Crystal Structure Database (ICSD; icsd.cds.rsc.org), which contains over 150 000 entries for unique materials. Taking a more fundamental combinatorial approach, the number of possible two-, three- and four-element combinations, each with specific oxidation states and stoichiometries, in fact exceeds the trillions (10^{12} possibilities). This indicates the presence of a vast unexplored compositional space, which may very well contain hidden 'wonder materials', patiently waiting for the opportunity to revolutionize modern technologies.

The exploration of such a broad physical space is evidently intractable to experiment or *ab-initio* calculations. However, high-throughput screening procedures involving a tiered, 'funnel' approach (as depicted schematically in figure 2) offer a promising pathway to efficiently probe this raw chemical landscape.

2.1.1. Reducing the search space. The first step in a materials discovery process is to apply certain universal constraints to immediately filter out unrealistic and irrelevant candidates. It is common practice to restrict the search space to specific material classes (compositions, structures, symmetries, motifs, etc) such as, *inter alia*, layered compounds, perovskite structures or

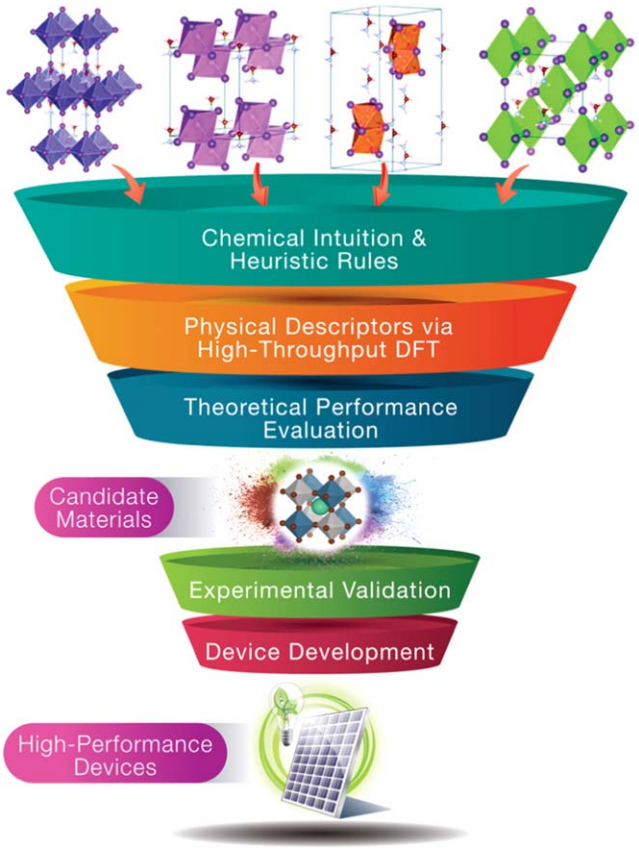

Figure 2. Simplified procedural outline of a typical high-throughput screening investigation, with a large input material space reduced to a small selection of promising candidates for further experimental verification and device development.

metal-organic frameworks, based on the intended application and chemical intuition. A pragmatic choice is to further restrict the search to abundant non-toxic elements, which are suitable candidates for wide-scale deployment in devices. Moreover, application of inexpensive charge neutrality, valency and electronegativity filters to remove chemically-implausible materials can reduce the combinatorial search space by two orders of magnitude [30].

A prerequisite for a viable candidate material is that it be synthesizable and (meta-)stable. Hence, this constraint is commonly applied at an early stage of the screening process, before any predictions of material properties and/or performance metrics are made. For instance, in a search for photoelectrochemically-active semiconductors, Davies *et al* employed Shannon ionic radii and Goldschmidt tolerance factors to predict the stability of inorganic elemental combinations in the cubic or orthorhombic perovskite structure, reducing their input dataset from 176 851 to 26 567 possible candidates [30].

2.1.2. Electronic structure theory. After reducing the material search space to a computationally-tractable subset, electronic structure techniques may be invoked to apply a more rigorous evaluation of the remaining candidate materials. A widespread choice is Density Functional Theory (DFT), due to its well-established accuracy (in predicting ground-state structures and formation energies) at relatively moderate computational cost. From high-throughput DFT calculations, theoretical predictions of relevant material properties and structure are performed, alongside validation of stability/synthesizability. While certain higher levels of theory, such as the inclusion of many-body effects within the Random Phase Approximation (RPA), yield improved predictions for the ground-state structural polymorphs of materials (relative to semi-local DFT) [17], the computational expense of such approaches typically render them infeasible for high-throughput investigations, for which speed must be prioritized over accuracy. This becomes increasingly apparent when one considers the success of semi-local DFT in predicting ground-state structures of typical chemical compounds, with only a handful of specific material classes requiring higher levels of theory.

Within DFT, there remains the choice of the vital ingredient: the exchange-correlation functional, which describes the quantum mechanical electron–electron interactions. Two common forms are the Local Density Approximation (LDA) and the Generalized Gradient Approximations (GGA). Decades of practical experience have revealed clear favorites for various material types or structural motifs, such as PBEsol (GGA) for standard inorganic solid compounds [31], DFT + U for materials with magnetic interactions or localized *d* orbitals [32], and dispersion-corrected functionals such as optB86b-vdW or Grimme's D3 for layered structures [33–35].

Databases of material simulations, such as the Materials Project (materialsproject.org), NOMAD repository (nomad-repository.eu) or MatNavi (mits.nims.go.jp), can often be of benefit in accelerating these initial screening steps and reducing the computational demand by providing calculated material structures and properties (e.g. formation energy). However, care must be exercised in these cases, as standardized calculation parameters (e.g. the choice of exchange-correlation functional) may not be suitable for certain material classes (e.g. layered compounds with van der Waals interactions). Thus, knowledge and experience of material simulations is required to judge the applicability of database information for a given screening investigation.

2.1.3. Chemical descriptors. At this point, the use of appropriate, well-informed, application-specific chemical descriptors is crucial in aiding both the efficiency and efficacy of the materials discovery process. In particular, these descriptors should be both central to performance and accessible by calculation. In the case of next-generation PV absorbers, relevant material properties would include the magnitude and nature (direct or indirect) of the electronic band gap E_g, charge-carrier mobilities $\mu_{e/h}$, minority-carrier lifetimes $\tau_{e/h}$, absorption coefficient α and the photoluminescence quantum efficiency (PLQE) η [36]. These are summarized in table 1. Recently, chemical descriptors of carrier effective mass, static polaron binding energy and Fröhlich electron–phonon coupling were used to predict 10 candidate p-type metal oxides [37]. These properties can be measured or predicted through various

Table 1. A collection of material properties and associated measurable/calculable descriptors relevant to the study and performance-prediction of materials for application in solar energy conversion. Reproduced with permission from [38].

Property	Descriptor	Calculation	Experiment
Optical Absorption	Band gap	Electronic Structure (e.g. DFT, *GW*)	Absorption Spectroscopy
	High-Frequency Dielectric Constant	Solid-state Energy Scale (SSE)	Ellipsometry
	Spectroscopically Limited Maximum Efficiency (SLME)	Tight Binding Analysis	
Electrical Conductivity	Effective Mass Tensor	Electronic Structure (e.g. DFT, *GW*)	Hall Measurements
			Four-Point Probe
	Mobility (lifetimes)	Lattice Dynamics	Van der Pauw Measurements
Bulk Radiative Recombination Rate	Electronic Band Structure	Electronic Structure (e.g. DFT, *GW*) with Spin–Orbit Coupling	Time Resolved Photoluminescence
	Relativistic Rashba Splitting		
Defect Tolerance/Non-Radiative Recombination	Dielectric Constant	Electronic Structure (e.g. DFT, *GW*)	Time Resolved Absorption Spectroscopy
	Bonding Analysis		
	Defect Transition Levels	Explicit Defect Calculations	
Bulk Photovoltaic Effect	Shift Current	Electronic Structure (e.g. DFT, *GW*)	Terahertz Emission Spectroscopy
			Current-Voltage Relationships
Contact Resistance	Band Offsets	Electronic Structure (e.g. DFT, *GW*)	Transmission Line Measurements
			Four-Point Probe
			Photoemission Spectroscopy
Surface/Interface Recombination	Surface Defect Density	Electronic Structure (e.g. DFT, *GW*)	Pump-Probe Reflectivity
Sustainability	Crystal/Elemental Abundance	Database (e.g. implemented in *SMACT* package) [39]	N/A

experimental or theoretical techniques, each with an associated cost, researcher-effort and accuracy. Judicious choice of appropriate descriptors is thus vital to the success of the screening procedure in accurately and efficiently determining potential candidate materials for the application in question.

Crucially, the level of theory, and hence computational overhead, required for sufficiently-accurate calculations can vary depending on both the property and material in question. For instance, standard DFT functionals exhibit a systematic underestimation of electronic band gaps in insulating crystals, as a consequence of the 'derivative-discontinuity' and self-interaction errors [29, 38]. Consequently, expensive techniques, *viz.* hybrid non-local DFT or many-body GW theory are necessary for the accurate determination of certain electronic properties, such as the band gap and optical absorption. At present, these costly methods are not readily applicable to high-throughput studies of large material datasets, despite recent advances in computational power. On the other hand, relatively-cheap standard DFT methods (such as LDA/GGA) are capable of accurately predicting the shape of electronic bands and thus determining related descriptors such as the charge carrier effective masses and mobilities [29].

In many cases, while the electronic band gap may be the more fundamental, performance-defining property (in relation to the specific application of e.g. a battery electrode material), it may be more prudent to use standard DFT methods to calculate other relevant descriptors first (e.g. carrier mobility), ruling out any inappropriate candidates before implementing higher-order, expensive techniques. In this manner, the most burdensome procedures, both in terms of computational demand and researcher effort, are restricted to only the most promising of candidates.

The presence of heavy elements is another case for which more sophisticated treatments are required, necessitating the description of relativistic effects. In particular, spin–orbit coupling (SOC) effects scale approximately with the square of the atomic mass, and so these contributions become increasingly significant as one moves down the periodic table [17]. Further down the line, proper accounting of non-radiative recombination for the determination of charge-carrier lifetimes and non-ideal quantum luminescence efficiencies requires explicit defect calculations. As discussed in further detail in section 2.3, these investigations demand substantial researcher effort and computational overhead, due to the number of

distinct calculations involved and the mandatory use of large simulation supercells.

After calculating the chosen descriptors for the material dataset, pre-determined selection criteria are applied so that only those materials with appropriate values for each property are considered. These candidate materials which successfully emerge from the chemical-descriptor screening stage should themselves be diligently analyzed in terms of crystal structure and chemical bonding. If similar characteristics evolve independently across multiple systems, design principles may be elucidated to accelerate materials discovery efforts and guide future investigations.

2.1.4. Performance metrics and figures of merit. Finally, a figure of merit or 'selection metric' is typically determined for each of the remaining candidates, such as the popular zT for thermoelectrics, yielding a final prediction of their potential success in the designated application. The ultimate purpose of the high-throughput materials discovery process is to identify promising candidates from vast input chemical space, based on the limited information available with finite resources (of time and CPU power). Accordingly, intelligent choice of selection metric is imperative to the success of these preliminary investigations.

For PV, there is still ongoing work in this regard, and several potential figures of merit have been put forward, as discussed below.

SQ Limit: In 1961, Shockley and Queisser derived the band gap-dependent radiative efficiency limit of a photovoltaic absorber ('SQ Limit'), using the principle of detailed balance [40]. This represented a tremendously significant development in the field of PV research, enabling predictions of maximum absorber performance, solely on the basis of the fundamental electronic band gap.

However, a number of large approximations are invoked in the SQ model, such as the assumption of perfect step-function absorption above the band gap E_g and neglect of non-radiative recombination (i.e. finite charge-carrier lifetimes) and material thickness. Consequently, several models have since been developed which go beyond the ideal SQ radiative efficiency limit [36, 41]. With each additional level of detail and complexity in these models, the predicted maximum efficiency decreases marginally from the SQ value, approaching a reasonable upper limit to the PV efficiency of a real-world device.

SLME: One extension was the 'spectroscopic limited maximum efficiency' (SLME) proposed by Yu and Zunger [41], which has seen considerable use in the literature since its introduction in 2012 [42, 43]. The SLME extends the SQ model to include the thickness and real, non-ideal absorbance of materials. Additionally, the SLME has the capacity to account for finite charge-carrier lifetimes, through specification of the internal quantum luminescence efficiency $Q_{\mathrm{lum,\,int}}$, though this requires prior knowledge of the rate of non-radiative recombination.

Blank *et al*: In 2017, Blank *et al* went a step further by describing the solar material using bulk properties, namely the refractive index and external (rather than internal) quantum luminescence yield $Q_{\mathrm{lum,ext}}$, thereby including the effects of light outcoupling and photon recycling [36]. The authors applied this metric to a range of emerging thin-film PV materials, including CZTS (Cu_2ZnSnS_4), $CuSbSe_2$ and Sb_2Se_3, finding that $CuSbSe_2$ exhibits the highest efficiency for ideal quantum luminescence efficiencies ($Q_{\mathrm{lum,ext}} = 1$), but that CZTS takes the lead at more realistic values ($Q_{\mathrm{lum,ext}} < 10^{-2}$). At present, this method entails a certain degree of manual calculation analysis, and so the development of a user-friendly open-source package to automate and streamline the process would substantially aid both the popularity of this performance metric and its applicability to high-throughput screening investigations.

TLC: In 2020, Kim *et al* developed a 'trap-limited conversion' efficiency (TLC) model to explicitly incorporate equilibrium populations of native defects, their carrier-capture coefficients, and the associated non-radiative recombination rates (figure 3) [44]. The TLC model relies on Shockley–Read–Hall (SRH) recombination statistics and the principle of detailed balance. Such an approach can provide a 'gold standard' of maximum efficiency prediction for assessing candidate PV absorber materials. However, it also entails significant computational expense, and so it is only applied to the most promising materials.

For example, the TLC model was recently applied to the kesterite family of quaternary thin-film photovoltaic materials, including CZTS, AZTSe ($Ag_2ZnSnSe_4$) and others, revealing intrinsic defect-limited maximum efficiencies in the range of 20%. In this case, the primary culprits are native tin-based defects, in particular the tin-on-zinc antisite Sn_{Zn}. These defects produce electronic states deep in the band gap, which act as 'killer' recombination centers, severely reducing charge-carrier lifetimes (as further discussed in section 2.2.1). This work offered valuable insight regarding the physical origins of poor experimentally-observed PV performance of these materials, which despite years of intense research and SQ radiative limits of ~33% [45], have as-yet failed to exceed power-conversion efficiencies of 12% [46].

In light of the fact that the efficiencies of actual PV devices are in most cases limited by non-radiative recombination (the effects of which are illustrated in figure 4) [47, 48], it is imperative that this loss mechanism is treated in first-principles investigations of PV performance. Indeed, champion materials from each respective generation of solar absorbers (c-Si, CdTe, $MAPbI_3$) demonstrate slow non-radiative electron–hole recombination kinetics which, in combination with large PLQE η and small Urbach tails, affords solar energy conversion efficiencies close to their radiative limits [49]. Extending the scope of materials discovery procedures to include these defect-governed properties will lead to improved predictions of successful next-generation photovoltaic materials.

2.2. Perovskite-inspired design principles and defect tolerance

Following the impressive optoelectronic performance of LHPs, recent efforts in the field have focused on leveraging theory to understand the physical properties underpinning their success [17]. From these chemical insights, design rules

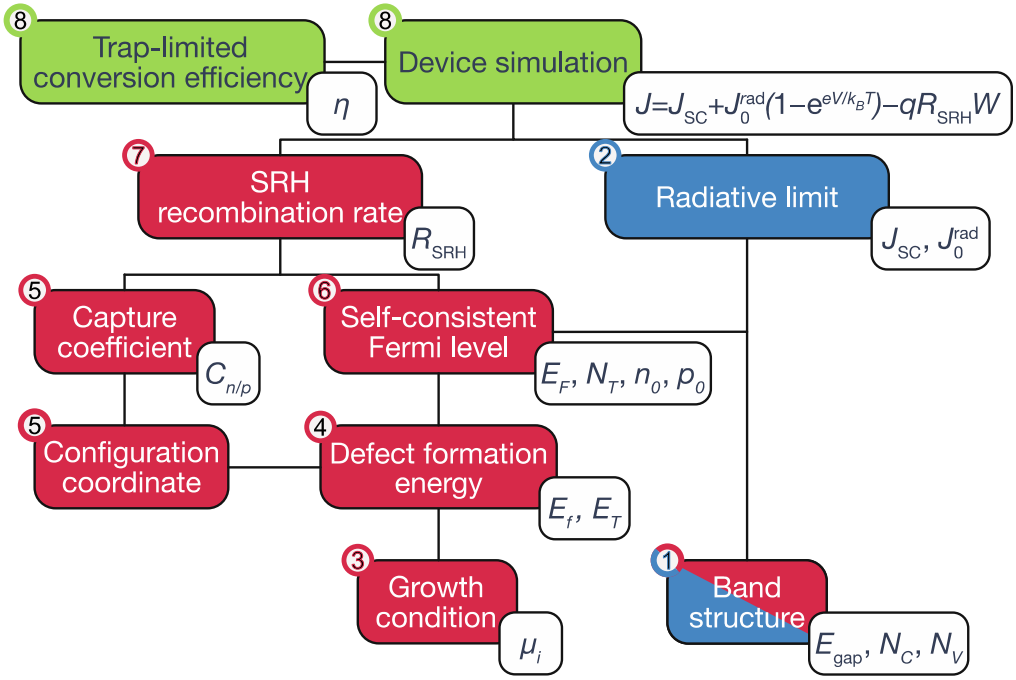

Figure 3. Schematic diagram of the calculation of the trap-limited conversion efficiency (TLC) metric. The dependent calculations are numbered and connected by lines, with the relevant calculated quantities appended. The red and blue boxes represent calculations for radiative and non-radiative electron–hole recombination, respectively. The combined device simulations are marked in green. Reproduced from [44]. CC BY 3.0.

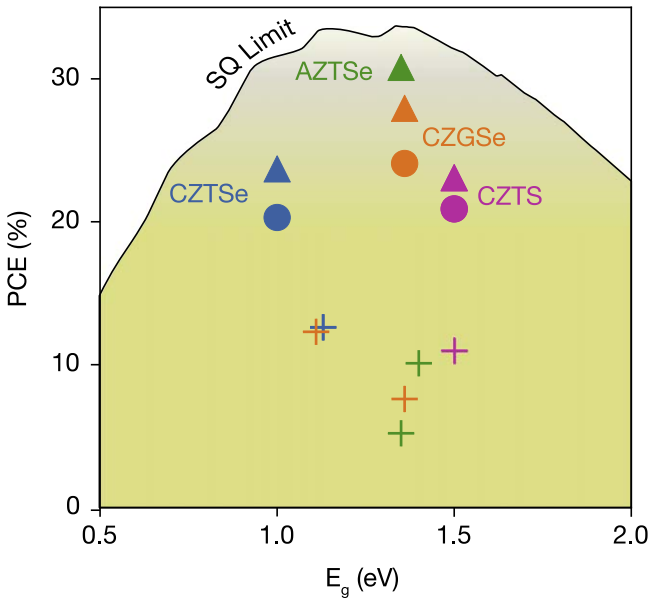

Figure 4. Shockley–Queisser limit and trap-limited-conversion (TLC) efficiencies for the kesterite family of thin-film PV materials. Filled symbols represent the TLC power-conversion efficiency and the black line is the SQ limit. TLCs with doping (triangles) show improved performances over TLCs without doping (circles). Plus signs indicate experimental data for kesterite solar cells. Reproduced from [44]. CC BY 3.0.

and screening criteria may be developed to guide the search for high-performance 'perovskite-inspired materials' (PIMs).

Undoubtedly, a defining feature of lead-halide perovskites (LHPs) is a remarkable tolerance to non-stoichiometry and crystalline defects, which facilitates their high PV efficiencies despite low-cost, solution-based synthesis routes. While deliberate implementation of defects plays an essential role in many relevant technological applications, such as topological insulators, quantum materials and, of course, doped semiconductors [50], the unintentional presence of defects can often trigger serious degradation in device performance [44]. In fact, as previously mentioned, provided the electronic band gap is in the appropriate range for an efficient PV material (~0.8 to 1.8 eV) [40], the most common performance-limiting factor for new absorbers is non-radiative recombination [47, 48]. By reducing the minority charge-carrier lifetime, non-radiative recombination impedes the collection of photo-generated carriers at the device terminals, thereby decreasing the open-circuit voltage.

We define defect tolerance as the tendency of a material to exhibit long minority carrier lifetimes (due to slow electron–hole recombination kinetics) despite the presence of crystallographic defects. This phenomenon has been definitively identified as a crucial factor in the success of LHPs [18, 50]. Many high-efficiency systems, such as single-crystal GaAs, are known to be extremely intolerant to the presence of point defects, necessitating a series of sophisticated and expensive procedures (in a clean room, or at high temperature) to fabricate pristine crystals for efficient PV devices. In contrast, perovskite solar cells may be synthesized via solution-based processing in normal laboratory environments at lower temperatures, which are typically up to only 100 °C. Nevertheless, LHPs manage to exhibit remarkably long minority carrier lifetimes and high PV efficiencies. Characterizing and understanding the physical mechanisms behind this extraordinary defect tolerance is thus a key research focus

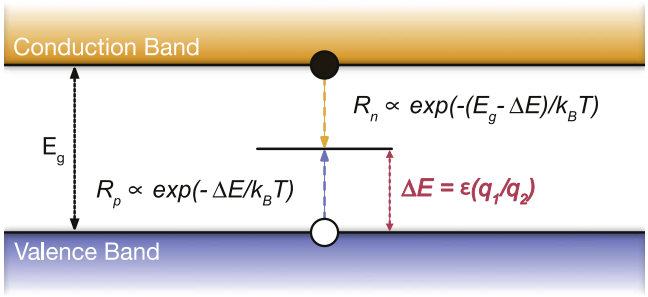

Figure 5. Electronic energy diagram of Shockley–Read–Hall recombination at a defect level $\Delta E = \varepsilon(q_1/q_2)$ above the valence-band maximum (VBM) (More on charge transition levels in section 2.3.3). Electron and hole capture rates, R_n and R_p, are exponentially dependent on the energy separation between trap level and band-edge.

for the discovery, design and development of low-cost, high-efficiency next-generation solar cells.

2.2.1. SRH theory of non-radiative recombination. From SRH theory, it is predicted that traps most likely to facilitate non-radiative recombination are those near the center of the electronic band gap [51]. Within this model, carrier-capture rates decrease exponentially with increasing energy separation between the defect transition level and the respective band-edge (i.e. the 'depth' of the defect level). Electron–hole recombination is a two-(quasi)particle process, and so a defect must sequentially capture both an electron and a hole for non-radiative recombination to occur, as depicted in figure 5. The total recombination rate is limited by the slower of the two capture processes. Thus, the closer a defect level is to the mid-gap region, the more rapid the recombination kinetics expected for an intrinsic semiconductor. Beyond the depth of the trap levels, there are several other important factors that contribute to the recombination activity of a particular defect (*vide* section 2.3), including the accessible charge states, concentration, and capture coefficient.

Shallow and deep defect states

Point defects are typically classified as 'shallow' or 'deep' according to a variety of criteria, such as the localization of the donor/acceptor wavefunction [52], the relative magnitudes of the carrier capture and emission coefficients [53], or, most commonly, the energetic position(s) of the defect charge transition level(s) in the band gap [18, 44, 50]. Deep defects typically exhibit localized electronic wavefunctions and charge transition levels 'deep' within the band gap. Shallow defect states, on the other hand, produce delocalized wavefunctions with charge transition levels near or within the continuum electron bands, thereby remaining innocuous with respect to carrier lifetimes and PV performance.

2.2.2. What makes a material defect tolerant?

2.2.2.1. Orbital character In an elemental semiconductor such as Si, there is a bonding valence band maximum (VBM) and an anti-bonding conduction band minimum (CBM), as depicted in figure 6(a). A point defect, such as a vacancy, can therefore produce non-bonding states at the center of the band

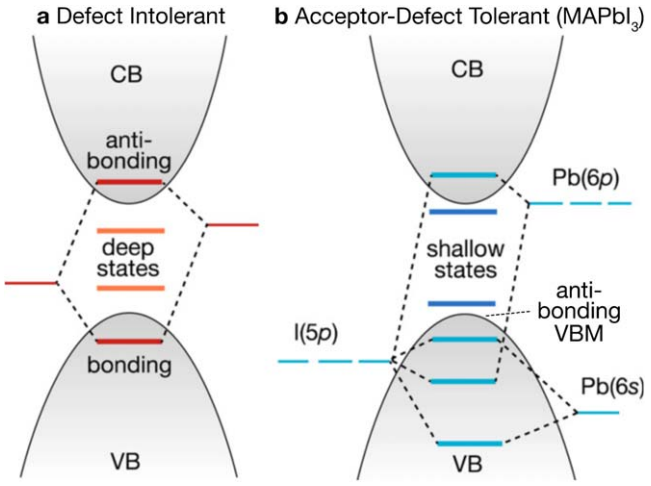

Figure 6. Electronic structure of typical 'defect intolerant' III–V, II–VI, or group IV semiconductors (left), prone to the formation of deep defect levels, compared to the 'defect tolerant' anti-bonding valence band of the lead halide perovskites (right). Reprinted with permission from [18]. Copyright (2017) American Chemical Society.

gap. Initially, defect tolerance was attributed to a change in the bonding character of the band-edges [50, 54]. This concept posited that the formation of shallow traps would be favored if the VBM originated from anti-bonding interactions and the CBM from bonding interactions. Non-bonding defect states would therefore fall in the valence or conduction band continua, rather than the band gap. This type of bonding is often associated with the presence of d^{10} cations (e.g. Cu^+), and has been, for example, observed in Cu_3N [55]. In Cu_3N, *p-d* orbital repulsion (due to the presence of filled Cu *3d* states) produces anti-bonding character at the VBM, with similar interactions leading to a bonding-type CBM.

Analogously, a similar phenomenon has been observed for LHPs, in which orbital repulsion between the halide anion *p* states and cation s^2 lone-pair acts as the source of anti-bonding interactions at the valence band-edge. However, in LHPs, the hybridization of the Pb 6*p* and anion *p* orbitals results in the formation of an anti-bonding state forming at the CBM (as opposed to the bonding-character CBM of Cu_3N), with the bonding orbital forming within the valence band [18]. This orbital arrangement is illustrated in figure 6(b), and is conducive to shallow defect formation because the original atomic orbitals (from which non-bonding defect states arise) are close to the band-edges or within the continuum bands, rather than deep within the band gap (figure 6).

A similar 'defect-tolerant' electronic structure can occur in the case of substantial band-edge splitting and dispersion, whether by spin–orbit or crystal-field effects. Through shifting and broadening the continuum electronic bands, the band-edges are pushed toward (if not beyond) the atomic orbital energy levels, in a manner analogous to that depicted in figure 6. Likewise, this situation promotes the formation of shallow defect states.

2.2.2.2. Coordination environment. Charge-carriers may be trapped at a deep defect state by long-range electrostatic and/

or short-range (orbital overlap and hybridization) potentials, with the former dominating in ionic materials and the latter more relevant for covalent compounds [56, 57]. In covalent semiconductors, hybridization of dangling-bonds at a defect center is thus a governing factor for the depth of the resultant charge transition level [58–60], as alluded to in the original defect tolerance concept above.

In the case of an anion vacancy, which is positively-charged in the fully ionized state (e.g. V_I^+ in $CsPbI_3$), the donor-type defect can trap a free electron by localizing it in the unoccupied *p* orbitals of the surrounding cations. The addition of an electron will cause these neighboring cations to slightly contract, on account of Coulomb attraction, thereby lowering the energy of the localized electron (due to increased hybridization of the dangling *p* orbitals). The strength of this electronic stabilization, relative to the strain energy from nearby stretched bonds, determines the trapping energy of the defect (i.e. depth of the defect transition level). If the orbital hybridization is not sufficiently strong, this localized electronic state will be unstable and the defect will instead adopt the energetically-favored shallow hydrogenic donor state, with the electron located at the defect-perturbed CBM.

The strength of this cation–cation interaction at the anion vacancy site will be dependent on both the anion coordination environment and the cation–cation distances, with low coordination numbers and large inter-cationic distances associated with weak hybridization and shallow defect levels. Thus, the presence of large anions and bond lengths with low anion coordination is predicted to aid defect tolerance, particularly in the case of chalcogenides, halides and chalcohalides, since anion vacancies are typically the primary native donor defects in these materials [59, 60].

In [60], Kim *et al* provide an instructive example of this behavior; employing an 'inorganic frame model' to decouple the chemical and structural effects of halide substitution on the anion-vacancy defect level for inorganic lead-halide perovskites. They demonstrate that the halide vacancy (V_X, X = I, Br, Cl) transforms from a delocalized shallow state in $[PbI_3]^-$ and $[PbBr_3]^-$ to a localized deep state in $[PbCl_3]^-$ (figure 7), as a result of lattice contraction (hence increased hybridization) from the smaller anionic radius, alongside band-shifting effects.

Analogous behavior could hypothetically occur for cation vacancy sites, with the strength of anion-anion dangling bond hybridization contributing to the depth of the acceptor defect level. That said, to the knowledge of the authors, this mechanism has not yet been ascribed to the formation of shallow acceptor states in a defect tolerant material. One likely reason for this is the fact that band-structure defect tolerance effects (section 2.2.2.1) are not always independent of structural effects. For instance, in the hypothetical cubic PbI_2, tetrahedral Pb coordination and shorter Pb–I distances strengthen the anti-bonding orbital interaction at the VBM, yielding shallow cation vacancies, as opposed to the deep states found in ground-state layered PbI_2 [61]. However, this coordination environment implies greater dangling-bond hybridization, and deeper defect states. The fact that, in this case, the energy upshift of the VBM outweighs that of the dangling-bond defect states, results in overall shallow cation vacancies.

In a similar manner, defect tolerance has been partially ascribed to ionic bonding in certain perovskite materials [57, 62, 63], with reduced covalency yielding lower energy dangling bonds and hence shallower defect levels. However, as mentioned earlier, long-range electrostatics may also induce charge localization and hence deep defect formation in heteropolar/ionic systems; the strength of this interaction being mediated by the dielectric constant of the material [56]. Thus, one should be wary of suggesting decreased covalency as an indication of potential defect tolerance in a candidate material, as it is a delicate balance of several competing effects (ion coordination, bond length, hybridization, bonding character, crystal symmetry, oxidation state, Jahn–Teller distortion, etc), which ultimately determine the energetic position of the defect charge transition level.

These points serve to highlight the intricacy of the physics governing the defect wavefunction, which must be carefully maneuvered when attempting to construct robust defect tolerance design principles.

2.2.2.3. Defect-carrier Coulomb interactions. An electron or hole in a semiconducting material may be attracted or repelled from a charged point defect due to simple Coulomb interactions, increasing or decreasing the carrier-trapping rate relative to the neutral case. This electrostatic effect is incorporated via the Sommerfeld enhancement factor $\langle s \rangle$, which for the attractive case is given by [64, 65]:

$$\langle s \rangle = 4 \left| \frac{Q}{q} \right| \sqrt{\frac{\pi E_R}{k_B T}} \propto \frac{|Q|}{\varepsilon} \sqrt{\frac{m^*}{T}}, \tag{1}$$

where $|Q|$ is the absolute charge of the point defect, q and m^* are, respectively, the carrier charge and effective mass, ε is the (low-frequency) dielectric constant, T is the temperature and E_R is the effective Rydberg energy:

$$E_R = \frac{m^* q^4}{2\hbar^2 \varepsilon^2}. \tag{2}$$

Depending on the dielectric and conductive properties of the material, the Sommerfeld factor $\langle s \rangle$ can range from anywhere between ~0.1 and 20, therefore strongly influencing electron–hole recombination kinetics and subsequent charge-carrier lifetimes. From visual inspection of equation (1), it is evident that several material properties can influence the magnitude of this carrier-capture enhancement factor, thereby contributing to the defect (in)tolerance of a material.

Enhanced dielectric screening: The dielectric constant reflects the ability of a compound to screen an electrostatic perturbation. Numerous material properties critical to the physics of a PV device, such as the rates of carrier-capture and ionized impurity scattering, the depth of shallow defect levels and exciton binding energies, are dependent on the dielectric constant [50]. For a given defect concentration, a larger dielectric constant corresponds to stronger Coulombic screening and hence diminished defect carrier-capture

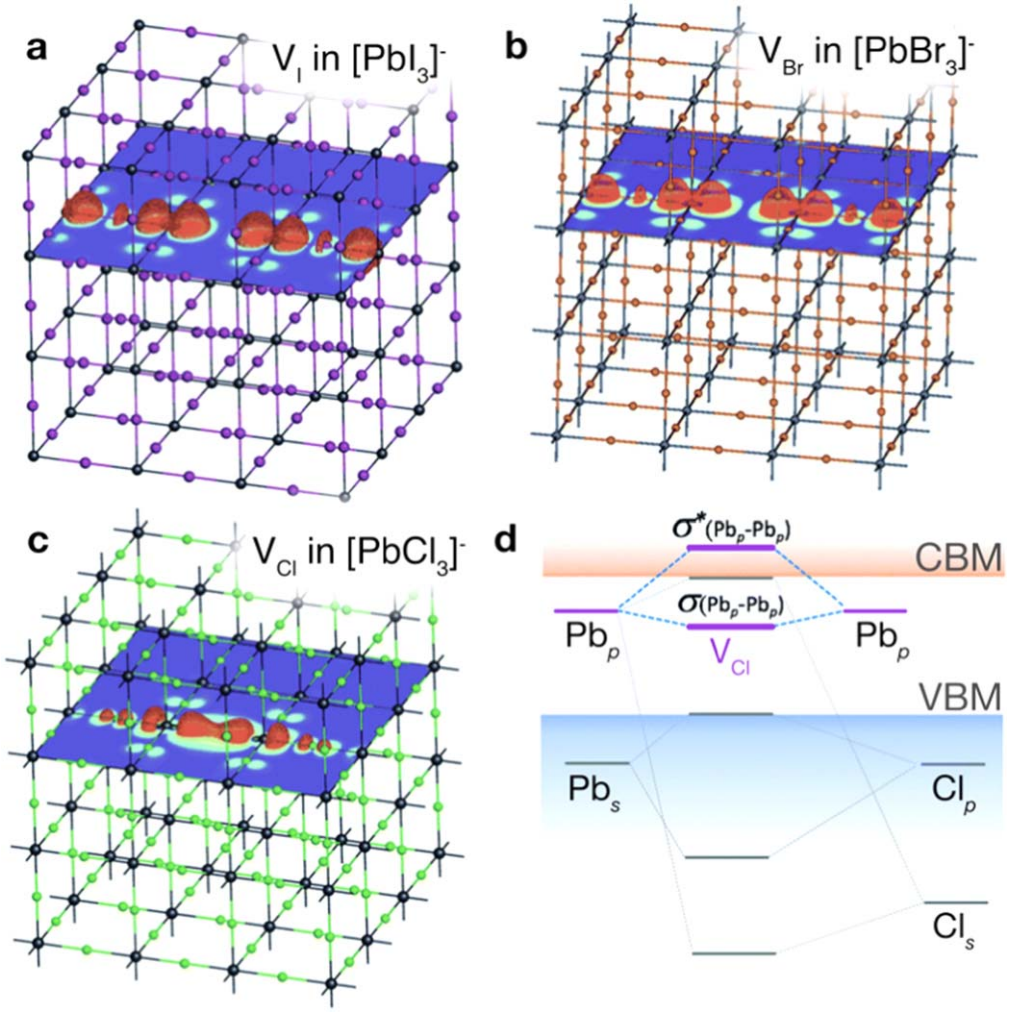

Figure 7. Charge density isosurfaces of V_X (X = I, Br, Cl) in (a) $[PbI_3]^-$, (b) $[PbBr_3]^-$ and (c) $[PbCl_3]^-$. For $[PbI_3]^-$ and $[PbBr_3]^-$ in (a) and (b), the orbital configuration of the halide anion vacancy V_X is primarily Pb 6*p*-X *p* anti-bonding character, matching that of the CBM (i.e. a shallow perturbed CBM state). For $[PbCl_3]^-$ in (c), however, a localized Pb 6*p* bonding state is formed. In (d), the orbital configuration for the formation of deep halide vacancy defects in $[PbCl_3]^-$ is shown. Reproduced from [60] with permission of The Royal Society of Chemistry.

cross-sections ($\langle s \rangle \propto 1/\varepsilon$), thereby suppressing the rate of non-radiative recombination.

Oxidation states: The oxidation states of species in a material determines the relative likelihood of different charge states for a given defect [66]. For instance, in CdTe, cadmium is formally in the +2 oxidation state, and so a cadmium vacancy V_{Cd} can take on the neutral and −2 charge states; $V_{Cd}{}^x$ and V_{Cd}'' in the Kröger–Vink formalism [67]. For a highly-charged defect, the kinetics of carrier-capture, and hence electron–hole recombination, can be accelerated relative to the neutral case ($\langle s \rangle \propto |Q|$). Thus, low oxidation-state materials may be more likely to contain low-charge defects with reduced carrier-trapping rates.

Effective mass: Spatial localization of electron and hole wavefunctions at defect sites can slow charge-carrier transport and is associated with thermal losses. A small effective mass will favor delocalized, nearly-free charge-carriers with decreased defect capture cross-sections ($\langle s \rangle \propto m^*$). Of course, a small effective mass is also beneficial for the carrier mobility and electrical conductivity of the device, as well as preventing the formation of small polarons [50].

2.2.2.4. Benign complex formation. Another proposed technique for the design of defect-tolerant materials is the passivation of 'killer' defect centers via the deliberate formation of benign defect complexes [50, 63, 68]. In this case, defect-defect interactions are leveraged to shift deep-levels closer to (or even into) the continuum bands, 'bleaching the gap' of deleterious trap states. The main adversary in this situation, however, is the entropic cost associated with defect-complex formation, which must be overcome either by an adequate enthalpy gain or the creation of metastable arrangements via intelligent synthesis strategies. Due to the inherent difficulty in engineering this state, this strategy remains largely unexplored for the design of novel defect tolerant materials.

2.2.2.5. Self-inhibiting defect levels. If a defect center produces multiple levels in the band gap, rather than

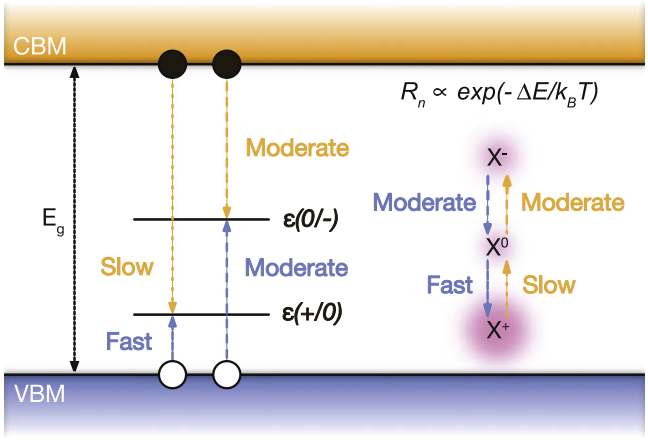

Figure 8. Energy level diagram of carrier capture and SRH recombination at two defect levels in the band gap, demonstrating 'self-inhibiting' behavior. (More on charge transition levels in section 2.3.3). Under the SRH model, the exponential dependence of carrier capture rate $\mathbf{R_n}$ on the energy separation between trap level and band-edge leads to a buildup of defects in the X^+ state. This defect charge state exhibits weak carrier capture kinetics, thus suppressing non-radiative recombination.

accelerate the recombination kinetics as one might initially expect, these extra levels often 'self-inhibit', reducing the overall rate of recombination [69, 70]. In this situation, it is likely that one of the defect levels is near a band-edge, far from the gap center. Due to the exponential dependence of charge-capture rate on the energetic separation of the defect level and corresponding band-edge (i.e. the 'depth' of the defect level), enormous imbalances in charge transition rates can arise in this case, leading to defects becoming 'stuck' in extreme charge states. Being near a continuum band, the near-edge defect level efficiently captures and re-emits the corresponding charge carrier (hole if near the VBM or electron if near the CBM). However, as depicted in figure 8, capture of the opposite charge carrier is exceptionally slow. Consequently, the majority of defects adopt the extreme charge state, exhibiting sluggish carrier capture and recombination kinetics.

On the other hand, the highly recombination-active charge states (which produce the mid-gap transition level) have almost negligible concentration and thus minimal overall recombination activity. Another way to conceptualize this mechanism is to recall that the total recombination rate for a given defect species is dictated by the slowest capture process involved (section 2.2.1). Hence, the incredibly slow capture rate of the extreme charge state introduces a bottleneck in the recombination cycle, greatly diminishing the overall recombination activity of the defect. Such tolerance can similarly occur in the case of strong anharmonicity, whereby transition rate imbalances are driven by a lack of symmetry in potential energy surfaces and charge capture barriers [70].

2.2.2.6. Related defect tolerant characteristics. **Crystal structure:** In any material, the crystal structure is a governing factor in the resultant electronic structure. Highly-symmetric crystal structures (viz. cubic phases such as halites, CsCl-type structures and cubic perovskites) tend to exhibit isotropic bonding and transport properties. Often, this behavior produces a direct fundamental gap (though the optical gap may still be indirect, due to strong selection rules) and relatively disperse band extrema, resulting in low effective masses [71, 72]. On the other hand, highly-anisotropic compounds such as layered materials often exhibit heavy effective masses and relatively flat electronic bands. More importantly, the crystal structure significantly influences the strength of both dangling-bond hybridization (section 2.2.2.2) and orbital repulsion at band-edges (section 2.2.2.1).

Cation electronic configuration: The electronic configuration of the cation is associated with a number of defect-tolerant properties in a material. In halide perovskites, an important case is the formation of the $6s^2$ lone pair configuration of Pb^{2+} in $MAPbI_3$, which has a partially oxidized valence electron shell relative to the fully-ionized $6s^06p^0$ Pb^{4+} ion. The resulting large, polarizable cation induces large Born effective charges (and thus a high dielectric constant) alongside stronger SOC of the unoccupied cation *p* states in the conduction band (hence increased band dispersion, favoring shallow donor defects, and reduced electron effective mass) [72, 73]. Moreover, filled s^2 orbitals can partially hybridize with the valence-band-dominated anion p orbitals, introducing anti-bonding character in the VBM (encouraging the formation of shallow acceptor defects) and broadening the valence bandwidth (thus reducing the hole effective mass).

This stable 'N-2' lone-pair oxidation state, and accompanying effects, is most commonly observed for the heavy post-transition metals in the sixth row of the periodic table (i.e. Tl^+, Pb^{2+} and Bi^{3+}), due to the relativistic contraction (and consequent stabilization) of the valence s orbital [74, 75]. Nonetheless, lighter cations (namely In^+, Sn^{2+} and Sb^{3+}) may also adopt these oxidation states in PV materials [72, 75, 76]. Moreover, strongly electronegative anions (F^-, Cl^-, O^{2-} etc) are more likely to fully oxidize the cations, hence softer elements (S^{2-}, Se^{2-}, I^- etc) are often required to stabilize the cation lone-pair.

A salient point, regarding the valence band anion p-cation s hybridization, is that the strength of this interaction (hence degree of dispersion and anti-bonding character at the band-edge) is dependent on the alignment and overlap of the atomic orbitals. If the cation lone-pair is much deeper than the higher-energy anion *p* orbitals, there will be minimal interaction between these states, with a consequently negligible contribution from the cation states to the band-edge. Indeed, this has been observed for certain Bi^{3+} lone-pair materials which were recently investigated as potential solar absorbers, including BiI_3 and $Cs_2AgBiBr_6$ [18, 42, 75].

This point provides an instructive example of the specificity of certain defect tolerance mechanisms, which unfortunately prevents the decoupling of elemental contributions to this phenomenon. Rather than simply searching for materials with stable lone-pair cations, one must also consider

their pairing with compatible anions to achieve the desired response.

2.2.3. Defect tolerance in lead halide perovskites. There has been much research on the atomistic origins of the strong defect tolerance exhibited by lead-halide perovskites (LHPs) [18, 50, 53, 60, 70–73, 77, 78]. Despite some disagreement in the literature [70, 77, 78], likely due to the multi-faceted origin of this phenomenon in LHPs, several material properties have now been definitively identified to contribute to the remarkable defect tolerance of these materials.

2.2.3.1. Defect tolerant band structure. Firstly, as depicted for the valence band in figure 6, perovskites exhibit a unique band structure in which interaction between the B-site cation ns^2 lone-pair and the anion p orbitals produces a dispersive, anti-bonding VBM. As discussed above, this situation is predicted to yield predominantly shallow acceptor-type defects, such as cation vacancies, alongside small hole effective masses and thus a decreased hole capture rate, per (1) [18, 53, 72].

In addition, for a heavy cation, such as Pb^{2+} in $MAPbI_3$, strong SOC broadens the bandwidth of the CBM, reducing the occurrence of deep donor defects in a similar manner to the bonding-character CBM in figure 6. Greater conduction band dispersion also lowers the electron effective mass, thus decreasing the rate of electron trapping per (1).

2.2.3.2. Cationic lone pair. The $6s^2$ electronic configuration of Pb^{2+} also aids defect tolerance in $MAPbI_3$ through a dramatic contribution to the dielectric properties of the material [58]. Born effective charges, describing the ionic polarizability, are enhanced by the presence of the Pb^{2+} cationic lone-pair. The resulting increase in mixed ionic-covalent bonding character leads to a massively-increased dielectric constant ($\varepsilon_r > 25$), which is approximately three times greater than that of other thin-film solar absorbers, such as CdTe and CZTS [50, 53, 73]. By effectively screening charged defect centers and enhancing carrier mobility, the highly-polarizable lone-pair emphatically suppresses non-radiative recombination and improves photovoltaic performance.

To illustrate the influence of a small effective mass m^*, large permittivity ε_r and low absolute oxidation states (+1, +2 and −1 respectively for the prototypical ABX_3 perovskite) on defect tolerance in LHPs, one can inspect the attractive Sommerfeld enhancement factor $\langle s \rangle$ for carrier capture. For a typical singly-charged defect in $MAPbI_3$ (e.g. V_I^+), $\langle s \rangle \simeq 2$, compared to $\langle s \rangle \simeq 10$ for a triply-charged defect in GaAs (e.g. $V_{As}{}^{3+}$), using values for m^* and ε_r quoted in [53].

2.2.3.3. Anion coordination environment. Beyond the effects of the valence s^2 lone pair, the low coordination number (2) of iodine, in conjunction with the expanded lattice constant from the methylammonium A-site cation, gives rise to weak Pb–Pb hybridization at the iodine anion vacancy center. This weak interaction is insufficient to create a deep bound state, further aiding defect tolerance in this material [58, 59]. Despite the presence of partial ionic character, long-range electrostatic effects are also unable to localize charge in this case, due to the small band gap and effective dielectric screening [56, 57].

The success of $MAPbI_3$ in combining weak cation–cation dangling-bond hybridization with a defect-tolerant electronic structure (section 2.2.3.1) indicates that ternary or multinary compounds may provide a fruitful search space for the discovery of new defect-tolerant materials [61]. In particular, materials which exhibit 'pseudobinary' behavior, containing a spectator ion which does not contribute to the band-edge states (see MA^+ cation in $MAPbI_3$), may be more likely to simultaneously exhibit low ion coordination and orbital repulsion at band-edges.

2.2.3.4. Inactive deep states. On the other hand, the few deep intrinsic defects that do still exist in LHPs, including iodine antisites I_{Pb} and I_{MA}, lead–iodine antisite Pb_I and interstitial lead Pb_i, have been shown to demonstrate weak recombination activity [70, 79]. The physical reason behind this inactivity has been debated. Initially, it was attributed to large predicted formation enthalpies, which would result in low concentrations with little to no adverse effect on carrier lifetimes [18, 79].

Recently however, this finding has been challenged, with 'self-inhibition' (as a result of multiple intra-gap defect levels) predicted to be the origin of slow recombination kinetics for I_{Pb} and Pb_I antisites [70]. The authors suggest that both anharmonic carrier-capture barriers and the presence of additional near-edge defect levels introduce bottlenecks in the non-radiative recombination cycle (*vide* section 2.2.2.5), thereby rendering LHPs tolerant to these deep traps.

2.2.3.5. Low Schottky defect formation energies. In addition, theoretical and experimental investigations have found low formation enthalpies of intrinsic Schottky-type defects (i.e. cation vacancy—anion vacancy complexes) [63, 68], suggesting high concentrations of benign defect complexes.

2.2.3.6. Self-healing. Finally, the soft crystal framework and relatively low melting temperature of LHPs points at the possibility of appreciable ion diffusion and 'self-healing' of defects at typical processing temperatures, resulting in fewer recombination-active defect center [80, 81]. Moreover, this leads to small phonon energies in $MAPbI_3$, which also contribute to a reduction in carrier capture rates [53, 82].

Evidently, the Pb^{2+} cation in lead-halide perovskites plays a pivotal role in the exceptional optoelectronic properties of these materials. Through its effects on the electronic band structure, dielectric screening and bonding behavior (as discussed above), the ns^2 cation contributes to an unfortunately rare combination of defect tolerance characteristics. This accomplishment has spurred extensive research efforts in the field of 'perovskite-inspired materials', which may be

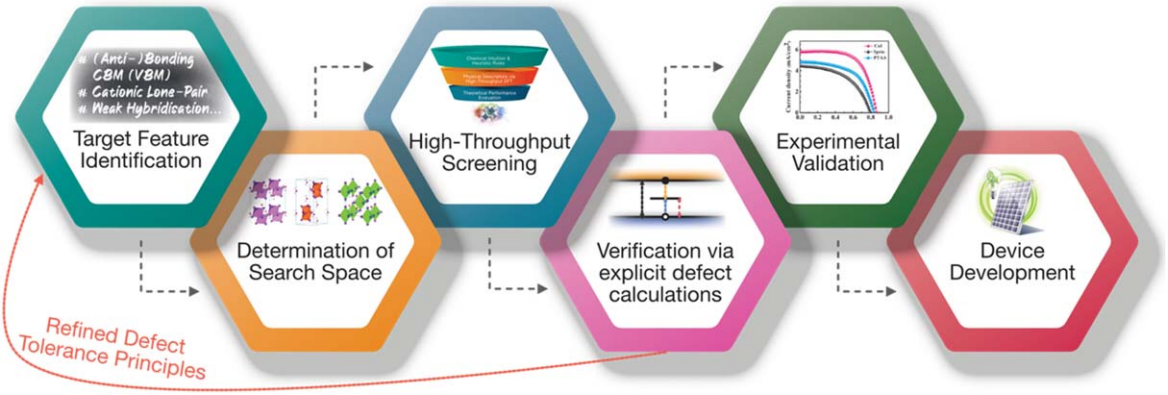

Figure 9. Outline of the synergistic combination of high-throughput screening, detailed theoretical investigation and experimental characterization to yield accelerated pathways to the discovery of defect-tolerant materials for low-cost high-efficiency devices. Red arrow indicates the feedback loop between target features for material screening and explicit defect investigations, affording refined design principles and screening criteria for efficient materials discovery.

capable of replicating the astonishing success of LHPs while overcoming the barriers of toxicity and stability.

2.2.4. Target features for defect tolerance. Through thorough investigation and enhanced understanding of the physical origins of defect tolerance in LHPs, it is hoped that general design principles may be developed for 'perovskite-inspired' defect-tolerant materials.

Such target material features include: (i) band-edge orbital repulsion (bonding character); (ii) large polarizable cation(s) (aiding dielectric screening of charged defects, band dispersion and anti-bonding valence band interactions—assuming sufficient spatial overlap and energetic alignment with anionic states); (iii) low atomic coordination alongside large ionic radii and lattice constants (reducing dangling-bond hybridization); (iv) mixed ionic-covalent bonding character (strengthening dielectric screening and suppressing dangling-bond hybridization); (v) crystal anharmonicity and/or multiple intra-gap defect levels (promoting 'self-inhibition'); (vi) low formation enthalpies for innocuous defect complexes; and (vii) soft crystal framework (to allow 'self-healing').

There is a plethora of ongoing research focusing on the implementation of these design principles as target features for high-throughput materials screening, with the goal of discovering next-generation defect-tolerant PV materials which are capable of rivalling the performance of the LHP prototype [18, 42, 53, 60, 70–73, 77, 78]. While there are likely few materials that match the wealth of defect-tolerant properties exhibited by lead-halide perovskites, with intelligent discovery techniques driven by detailed understanding of the underlying chemistry (as depicted in figure 9), one can hope that further successful absorber materials may be unearthed.

In the context of materials screening, some of these material properties are relatively simple to predict *a priori*, for example the cation electronic configuration, bonding covalency and ionic radii, while others, such as those involving orbital interactions or carrier-capture kinetics, can be tremendously challenging. For instance, accurate calculation of the energetic alignment of cation lone-pair and anion *p* states (to predict anti-bonding interactions at the VBM in a perovskite-structured material) is often a computationally taxing procedure, requiring a high level of theory. Identification of 'self-inhibition', whether by crystal anharmonicity or multiple intra-gap levels, requires defect-specific, quantitative investigations [70]. Likewise, prediction of benign defect complexes is not readily amenable to high-throughput computation, due to the enormous configurational space and inherent complexity involved, on top of the substantial cost of defect calculations. This point serves to reinforce the importance of strategic organization of materials screening steps, alongside the judicious selection of chemical descriptors and success criteria, on the basis of relevance, cost, accuracy and researcher-effort.

After applying these design principles at an intermediate stage of the screening process (through the use of appropriate chemical descriptors), explicit defect calculations may then be performed on the most promising remaining candidates at the bottom of 'screening funnel' (figure 2), in order to fully assess their defect tolerance potential and to yield an accurate performance figure of merit (*SLME, Blank et al, TLC...*). In section 2.3, we provide a brief overview of the practical calculation of relevant defect properties from first-principles.

2.3. Ab-initio defect calculations

A wide range of defect properties (including formation energies, equilibrium concentrations, charge transition energy levels, carrier capture coefficients, etc) are now accessible to theoretical investigation, due in no small part to the aforementioned advances in theory and computational capacity. By elucidating the physical underpinnings of defect behavior in solids, chemical models of improved accuracy may be constructed in order to better predict, describe and design defect-related material properties. Such insights can enable researchers to tune material properties via strategic manipulation of defect concentrations (through carefully-controlled synthesis conditions), whether to deliberately introduce defects (e.g. for doping-induced conductivity or enhanced

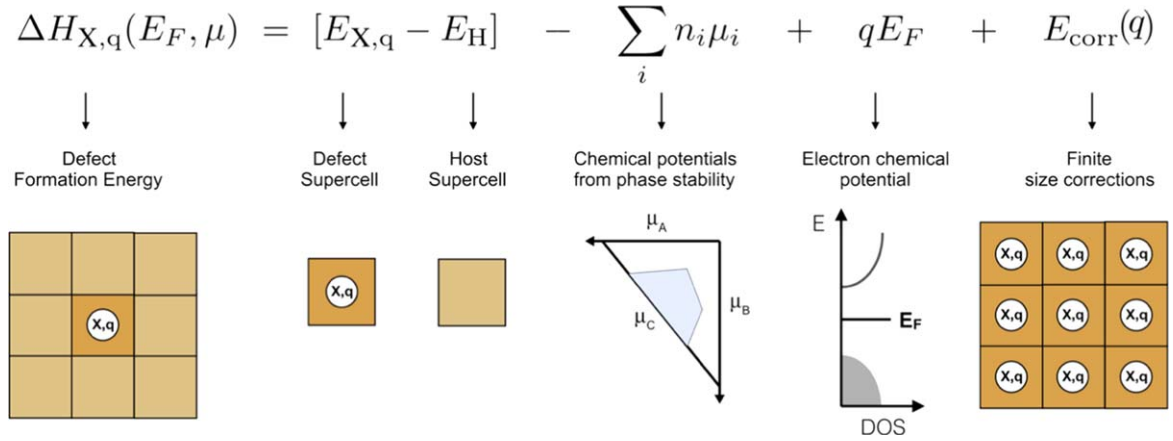

Figure 10. Contribution of various terms in the calculation of defect formation energy. Reprinted from [90], Copyright (2017), with permission from Elsevier.

lasing action [83]) or to mitigate the effects of deleterious defects (e.g. for improved PV efficiency or battery lifetime [50, 84, 85]).

The purpose of this section is to give a brief flavor of the practical implementation, frontiers and challenges of this research. For a more detailed overview of the theory, state-of-the-art and practical aspects of defect calculations, the keen reader is directed elsewhere [52, 86, 87].

2.3.1. Supercell approach. DFT has established itself as the most powerful technique for first-principles investigations in solid-state physics [88, 89], including point-defect calculations [86]. Within DFT, the most widely employed method for defect calculations is, by far, the 'supercell' approach with a plane wave basis set [52, 86, 87]. This involves placing a defect in an expanded crystal unit cell of the 'host' material (termed a 'supercell') with anywhere from ~50 to 200 atoms, which is then periodically repeated through space. In doing so, researchers may exploit the power and versatility of periodic DFT codes, while also guaranteeing an accurate description of the host material in most cases.

2.3.2. Defect formation energy. Both equilibrium concentrations and charge transition energy levels are determined by the formation energies of the corresponding defect states. The formation energy $\Delta H_{X,q}(E_F, \mu)$ of a defect X in charge state q is given by:

$$\Delta H_{X,q}(E_F, \mu) = [E_{X,q} - E_H] - \sum_i n_i\mu_i + qE_F + E_{\mathrm{Corr}}(q). \quad (3)$$

The contribution of each of these terms to the calculated defect formation energy $\Delta H_{X,q}(E_F, \mu)$ is illustrated diagrammatically in figure 10. $E_{X,q}$ is the calculated energy of the *defect-containing* finite-sized supercell, while E_H is the energy of an equivalent *pristine* host supercell. The second term $(-\sum_i n_i\mu_i)$ accounts for the thermodynamic cost of exchanging n_i atoms with their reservoir chemical potential(s) μ_i, to form the defect X_q from the ideal bulk material. Analogously, qE_F represents the energetic cost of removal or addition of charge q to the defect site, from the electronic reservoir of the system (i.e. the Fermi energy E_F). Finally, $E_{\mathrm{Corr}}(q)$ is a correction for any spurious finite-size supercell effects.

As mentioned previously, the dependence of defect formation energy $\Delta H_{X,q}(E_F, \mu)$, and hence equilibrium concentration, on atomic chemical potentials μ_i allows for the manipulation of defect populations, via controlled synthesis conditions. Indeed, high-efficiency perovskite solar cells have relied on the strategic manipulation of iodine chemical potentials during crystal growth in order to suppress non- radiative recombination channels [84].

2.3.3. Charge transition energy levels. Defects in semiconductors typically introduce electronic levels near or within the band gap, which determine the interaction of the defect site with charge carriers in the material. These electronic levels are the 'thermodynamic charge transition levels' $\varepsilon(q_1/q_2)$, defined as the Fermi level position for which the formation energies of the defect in charge states q_1 and q_2 are equal [86]:

$$\varepsilon(q_1/q_2) = \{E_F | \Delta H_{X,q_1}(E_F) = \Delta H_{X,q_2}(E_F)\}. \quad (4)$$

As illustrated in figure 11, charge state $\boldsymbol{q}_1$ is stable for Fermi level below $\varepsilon(\boldsymbol{q}_1/\boldsymbol{q}_2)$, while for Fermi levels above $\varepsilon(\boldsymbol{q}_1/\boldsymbol{q}_2)$, charge state $\boldsymbol{q}_2$ is stable ($\boldsymbol{q}_1 > \boldsymbol{q}_2$, by convention). Charge transition levels are crucial to the electronic behavior of defects, as their energetic position within the host band structure is a dominant factor in the recombination activity of defect centers (*vide* section 2.2.1).

Employing the computational methods described in sections 2.3.1 and 2.3.2, charge transition levels may be theoretically predicted via equations (3), (4), as illustrated in figure 11. Moreover, these levels may be experimentally detected via techniques such as Deep-level Transient Spectroscopy (DLTS) [86]. This highlights the importance of these properties in defect investigations, as they allow for the powerful combination of theory and experiment to yield enhanced understanding of defect behavior. Through comparison of theoretical and experimental results, computational

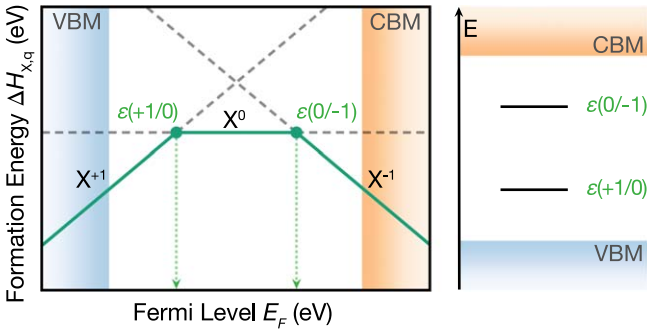

Figure 11. Defect charge transition levels from a formation energy (with respect to Fermi level) plot (left) and on an energy band diagram (right). Reproduced with permission from [91].

methods may be validated, and experimental observations may be interpreted and understood in detail.

2.3.4. Computational overhead. While standard DFT methods (i.e. LDA/GGA) are capable of producing reliable crystal structures (in most cases), systematic failures in the prediction of band gaps (section 2.1.2) and charge localization render them unsuitable for investigations of defect electronic structure. These electronic properties are crucial to defect behavior, determining the position of charge transition levels in the host band structure and hence the nature of the defect trap state. This issue is tackled via the use of 'beyond-DFT' methods, the most popular choice being hybrid DFT, which inevitably entail significant inflation of the computational demand. This requirement of expensive, high-level electronic structure theory, in conjunction with large simulation supercells (section 2.3.1), is the primary culprit behind the substantial computational cost associated with defect calculations.

2.3.5. Frontiers and challenges of defect modelling

2.3.5.1. Automation and databases. At present, defect investigations entail exorbitant levels of manual researcher effort, due to the large number of individual calculations required. Fortunately, a number of computational packages have been released (including PyCDT [92], PyLada [90], COFFEE [93], sxdefectalign [94], CarrierCapture.jl [95], CPLAP [96], SC-Fermi [97]...), which can assist with efficient pre- and post-processing of these calculations. Through continued development of comprehensive, flexible, user-friendly computational tools, researchers hope to accelerate the efficiency of defect studies and expand their applicability to high-throughput materials discovery.

Furthermore, powered by a rapid growth in computational power and availability of automation frameworks such as AiiDA [98] and FireWorks [99], databases of material simulations are being extended to include *ab-initio* defect calculations. These invaluable resources will provide the opportunity to gain powerful chemical insights, especially when combined with machine learning (ML) models and data science techniques.

2.3.5.2. Carrier capture. A crucial step in the process of non-radiative electron–hole recombination is the capture of delocalized charge carriers by defect traps, via electron–phonon coupling. Recent years have seen the development of theory and computational tools to quantitatively model this process [95, 100, 101], though further improvements in efficiency, versatility, and reliability are necessary to extend this approach to general application.

2.3.5.3. Additional hurdles. Further challenges faced by defect studies include transferability issues (due to inconsistent realizations of electronic structure theory and finite-size corrections), accurate treatment of finite-temperature effects (demanding substantial computational and researcher effort [86]) and modelling of diffusion/transport properties (limited by the length- and time-scales of molecular dynamics simulations).

3. Classes of perovskite-inspired materials explored

Halide perovskites have the general formula ABX_3, where A is a monovalent organic or inorganic cation, B is an octahedrally coordinated divalent cation, and X is a monovalent halide such as Cl, Br, or I. Chemical substitution of Pb^{2+} for alternative, less-toxic B-site cations has been widely explored. However, the perovskite crystal structure can only be maintained if the cation has a +2 oxidation state and if the ionic radius can fit within the crystal structure. The latter is described by the Goldschmidt tolerance factor, $t = \frac{(r_A + r_X)}{\sqrt{2}(r_B + r_X)}$, where r_A, r_B, and r_X are the ionic radii of the A, B, and X site ions, respectively. Empirically, stable perovskite structures have t ranging from 0.8 to 1.1 [102], which can only be achieved by a limited number of compositions [103]. Substitution of Pb(II) for other metal Group 14 cations with sufficiently large ionic radii (e.g. Sn^{2+} and Ge^{2+}) can result in t values within the required range, forming perovskite structures (i.e. $ASnX_3$ and $AGeX_3$), as shown in figure 12. An alternative that allows metal cations without a stable +2 oxidation state to be used is to combine a monovalent and trivalent cation (e.g. Ag^+ and Bi^{3+}), which occupy alternating octahedra, to form double perovskites. But beyond identifying materials with perovskite crystal structures, efforts have also focused on the inverse design of defect-tolerant materials, as described in section 2.

This section discusses the synthesis routes and optoelectronic properties of several classes of PIMs considered, including Sn- and Ge-based perovskites, double perovskites, as well as other potentially defect-tolerant compounds ($A_3B_2X_9$, ABZ_2, binary halides, and V–VI–VII materials). Crystal structures and some important features of the PIMs discussed here will be illustrated in figure 13 below and table 2 at the end of this section, respectively.

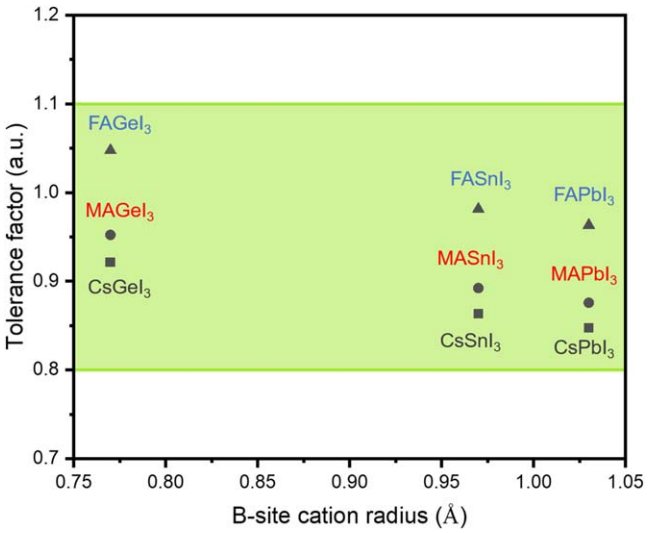

Figure 12. The geometric tolerance factors of three classes of perovskites with different B-site cations based on their ionic radii [103–105].

3.1. Sn-based perovskites

As with lead-halide perovskites, Sn-based perovskites can have $CH_3NH_3^+$ (MA), $CH(NH_2)_2^+$ (FA), Cs^+ and other alkali cations in the A-site. Though most Sn-based perovskites have a perovskite structure with a high symmetry α cubic phase (figure 13), some $CsSnX_3$ perovskites may transform into the γ orthorhombic phase with distorted octahedra at room temperature [213], which is mainly due to their smaller tolerance factors.

Although many fabrication methods have been developed for LHPs, these methods are usually not directly compatible with their Sn-based counterparts. Sn-based perovskites crystallize much faster than Pb-based perovskites due to the lower solubility of SnI_2 in typical solvents such as *N*,*N*–dimethylformamide (DMF) [214]. Therefore, Sn-based perovskite thin films are often fabricated by modified solution methods with the addition of reagents to the precursors.

The one-step solution method was first developed by Hao *et al* [215]. It has been found that replacing DMF with dimethyl sulfoxide (DMSO) as the solvent can reduce the crystallization rate of Sn-based perovskites by the formation of the intermediate product SnI_2:3DMSO (figure 14(a)), leading to pinhole-free films [214]. Film morphology has been further enhanced using solvent engineering methods (figure 14(b)). In this method, perovskite precursors are dissolved in mixed solvents, such as γ-butyrolactone (GBL)/DMSO [216] and GBL/1-methyl-2pyrolidinone (NMP) [217]. During spin-coating, a non-polar 'antisolvent' is dropped. Common antisolvents include toluene and chlorobenzene, which the ionic perovskite precursors are insoluble in. Dropping the antisolvent causes the intermediate phase to nucleate and form. After annealing, a uniform thin film can be obtained. Faster reaction between precursors and following nucleation can significantly improves the uniformity of thin films. The morphology of fabricated thin films is also strongly related to the antisolvent used and how it is dropped onto the spinning substrate.

Sn-based perovskites can also be fabricated by vapor deposition methods [218, 219], which are advantageous for depositing multiple layers of over large areas. For instance, $MASnI_3$ showing complete coverage over the substrate has been grown through co-evaporation of MAI and SnI_2 [220]. Vapor deposition can also be combined with solution deposition to make films with higher quality. For example, low-temperature vapor-assisted solution processing (LT-VASP) [221] has been developed to deposit ultrasmooth $MASnI_3$ thin films (figure 14(c)). Two steps were involved in this method. Firstly, SnI_2 thin films were spin-coated onto mesoporous TiO_2 substrates. Secondly, the substrates kept at 60 ℃ were placed over MAI powder heated at 150 ℃ and $MASnI_3$ films would then form as MAI was evaporated onto SnI_2 films.

In addition, some tin-halide additives such as SnF_2 and $SnCl_2$ have been introduced into the above methods to promote the film quality in many aspects. For example, SnF_2 added in $CsSnI_3$ can reduce the Sn vacancies and enhance the stability of perovskites without changing the lattice parameters [222, 223]. On the other hand, $SnCl_2$ may form an ultrathin hole transport layer at the ITO/$CsSnI_3$ interface and improve the carrier extraction [121].

Similar to lead-halide perovskites, Sn-based perovskites also have direct band gaps ranging from 1.3 to 2.1 eV with high absorption coefficients of around 10^4 cm^{-1} in visible region [224]. Band gap tunability is crucial for the design of tandem solar cells, where semiconductors with different band gaps are stacked sequentially in order to absorb different regions of the solar spectrum. It has been shown that different X-site halides can greatly affect the band gap of Sn-based perovskites [215, 225]. For instance, the band gap can be tuned from 1.3 to 3.61 eV from by changing the X anion in $MASnX_3$ from I^- to Cl^-. Also, Sn/Pb hybrid perovskites were found to exhibit significant band gap bowing, where the alloy band gaps are smaller than the band gap of both end compounds. Recently, $MA(Pb_{1-x}Sn_x)I_3$ has demonstrated a band gap below 1.2 eV at $x = 0.5$ [226]. Goyal *et al* showed through computations that this extraordinary feature is primary due to the energy mismatch between the *s* and *p* orbitals between Sn and Pb and their nonlinear mixing (figure 15) [227].

Sn-based perovskites tend to become *p*-type due to the self-doping. Although the oxidation of Sn^{2+} to Sn^{4+} should release electrons (*n*-doping), the lower formation energies of Sn vacancies [122] and some processes such as the reaction of Sn^{2+} with O_2 may create holes and lead to *p*-doping [213]. However, the mechanism behind *p*-type doping is not fully understood yet. *p*-type self-doping leads to high mobilities and metal-like conductivity of Sn-based perovskites. Relatively small effective masses (0.01–0.11m_0, m_0: rest mass of an electron) caused by the dispersive VBM further improve their carrier transport. A hole mobility of 585 and 322 cm^2 V^{-1} s^{-1} have been reported in $CsSnI_3$ and $MASnI_3$ polycrystalline ingots, respectively [110, 122], based on Hall-effect and resistivity measurement. Interestingly, Stoumpos

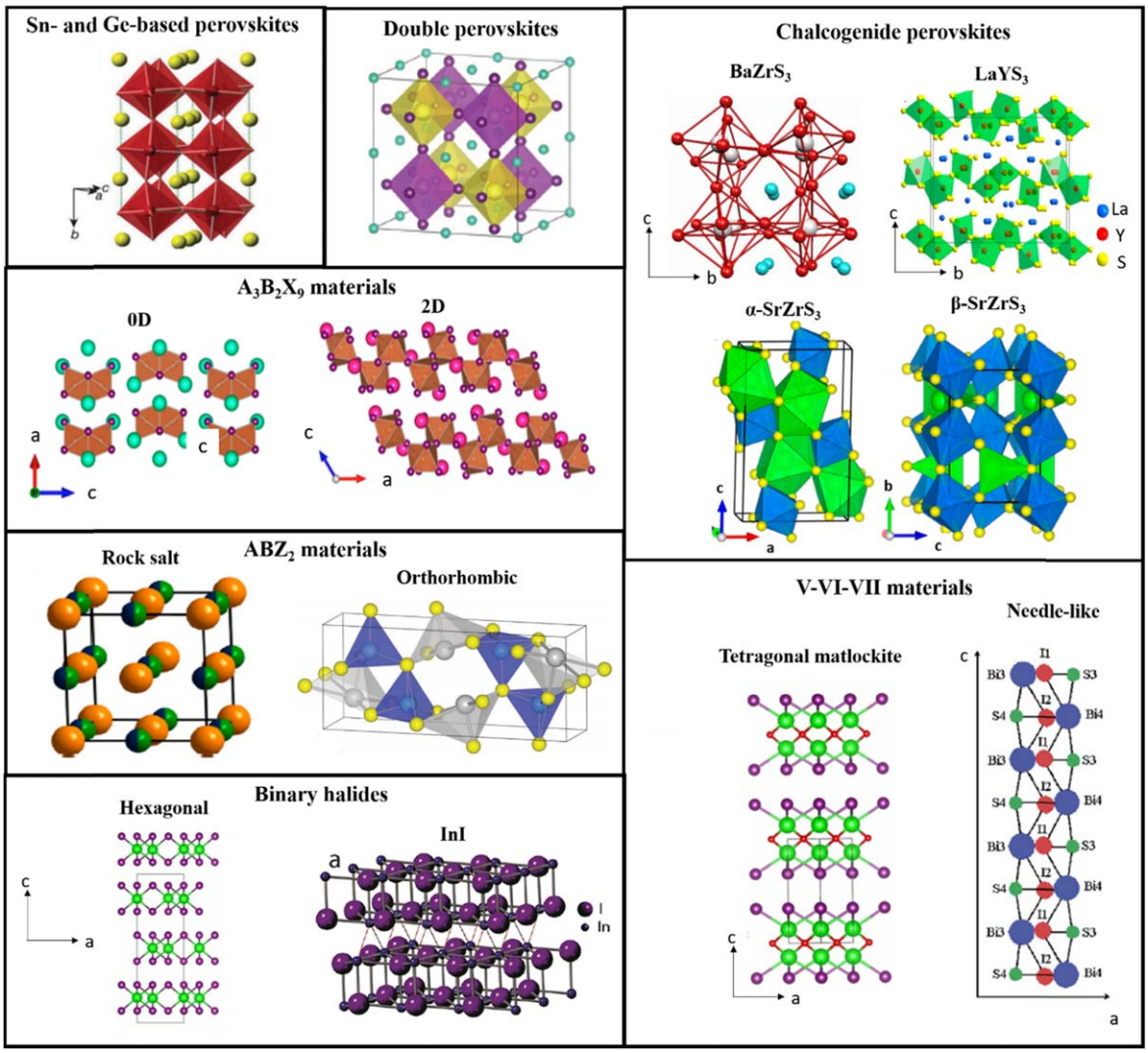

Figure 13. Crystal structures of various PIMs discussed in this Review. The axes for the crystal structures of each material follows the axes in the upper left corner if not otherwise marked. (Sn- and Ge-based Perovskites) [19] John Wiley & Sons. © 2018 WILEY-VCH Verlag GmbH & Co. KGaA, Weinheim. (Double Perovskites) [20] John Wiley & Sons. © 2019 WILEY-VCH Verlag GmbH & Co. KGaA, Weinheim. (0D and 2D) Reprinted with permission from [21]. Copyright (2018) American Chemical Society. (Rock salt) Reprinted with permission from [22]. Copyright (2018) American Chemical Society. (Orthorhombic) Reproduced from [106] with permission of The Royal Society of Chemistry. (Hexagonal) Reprinted with permission from [24]. Copyright (2020) American Chemical Society. (InI) Reprinted with permission from [107]. Copyright (2018) American Chemical Society. ($BaZrS_3$) Reprinted with permission from [108], Copyright (2009) by the American Physical Society. ($LaYS_3$) Reprinted with permission from [23]. Copyright (2019) American Chemical Society. (α- and β-$BaZrS_3$) Reproduced from [109]. CC BY 4.0. (Tetragonal matlockite) Reprinted with permission from [24]. Copyright (2020) American Chemical Society. (Needel-like) Reprinted from [25], Copyright (2007), with permission from Elsevier.

et al claimed that the *p*-type character of Sn-based perovskites is related to the formation of Sn^{4+} centers, which could be suppressed by the introduction of a powerful reducing agent (e.g. H_3PO_2). Eventually, they showed that *n*-type polycrystalline $CsSnI_3$ and $MASnI_3$ could be obtained and also exhibit high electron mobilities of 2320 and 536 $cm^2\ V^{-1}\ s^{-1}$ (from Hall-effect measurement), respectively [110].

The carrier lifetime has been reported to be 59 ps and 6.6 ns in $FASnI_3$ thin films with 20 mol% SnF_2 additives and $CsSnI_3$ single crystals [117, 123], respectively. These relatively short carrier lifetimes compared to their Pb-based counterparts were mainly related to the electron recombination with large background hole densities (10^{14}–10^{19} cm^{-3}) [122, 228]. However, the incorporation of ethylenediammonium (en) or SnF_2 in some Sn-based perovskites has been found to reduce Sn vacancies and extend carrier lifetimes [111, 229]. For instance, $MASnI_3$ thin films with 20 mol% SnF_2 have shown a lifetime longer than 10 ns, which is almost 5–10 times of that of pristine $MASnI_3$ [111]. Moreover, the addiction of ZnI_2 could even improve the carrier lifetimes of $FAPb_{0.5}Sn_{0.5}I_3$ perovskites up to ~1 μs [230]. The presence of these sub-gap defects also results in the low PLQEs of Sn-based perovskites. As a result, the PLQEs of mixed Pb-Sn perovskites under solar illumination were typically less than 1% [231]. It is worth mentioning that

Table 2. Important properties of PIMs discussed in this review. RT = room temperature; m_e^*/m_h^* = the smallest effective electron/hole masses reported in the corresponding references; $\mu/\mu_e/\mu_h$ = the highest sum/electron/hole mobilities reported in the corresponding references; SC = single crystals; PC = polycrystalline ingots; TF = thin films; QD = quantum dots; NC = nanocrystals.

Material		Space group @ RT	m_e^*/m_h^* (m_0)	Band gaps (eV)	Mobility ($cm^2\ V^{-1}\ s^{-1}$)	Carrier lifetime (ns)	Highest PCE (%)	Reference
Sn-based perovskites	$MASnI_3$	Pm3m	0.1/0.11	1.23–1.4	$\mu_h \sim 322$ (PC) $\mu_e \sim 2320$ (PC)	10.2 (TF)	6.63	[110–116]
	$FASnI_3$	Amm2	0.02/0.05	1.35–1.45	$\mu_h = 67$ (TF) $\mu_e = 103$ (PC)	0.59 (TF)	12.4	[110, 115, 117–120]
	$CsSnI_3$	Pnma	0.041/ 0.069	1.3	$\mu_h = 585$ (SC) $\mu_e = 356$ (PC)	6.6 (SC)	3.56	[110, 121–125]
Ge-based perovskites	$MAGeI_3$	R3m	0.27/0.29	1.9–2	—	—	0.68	[126, 127]
	$CsGeI_3$	R3m	0.22/0.23	1.6	—	—	0.11	[127, 128]
	$FAGeI_3$	R3m	0.66/0.76	2.35	—	—	—	[127, 129]
Double perovskites	$Cs_2AgBiCl_6$	$Fm\bar{3}m$	0.53/0.15	2.5–2.77	—	—	—	[130–132]
	$Cs_2AgBiBr_6$	$Fm\bar{3}m$	0.37/0.14	1.95–2.5	$\mu \sim 1$ (TF) $\mu \sim 11.81$ (SC)	1400 (TF)	2.84	[130, 131, 133–137]
	Cs_2NaBiI_6	$Fm\bar{3}m$	0.28/0.58	1.66	—	—	0.42	[138, 139]
	$Cs_2AgInCl_6$	$Fm\bar{3}m$	0.29/0.28	3.3–3.53	—	—	—	[131, 140]
	$(MA)_2AgBiI_6$	$Fm\bar{3}m$	0.47/0.7	1.02–1.96	—	—	—	[131, 141]
	$(MA)_2AgBiBr_6$	R3m	0.15/0.24	1.25–2.02	—	—	—	[142, 143]
$A_3B_2X_9$ materials	$MA_3Bi_2I_9$	C 2/c	0.54/0.95	1.94–2.1	$\mu_h = 70$ (SC)	~40 000 (SC)	3.17	[144–149]
	$FA_3Bi_2I_9$	$P6_3mc$	—	1.85–1.94	$\mu = 0.224$ (TF)	—	—	[146, 150]
	$Cs_3Bi_2I_9$	C 2/c	1/1.1	1.9–2.2	$\mu_h = 1.7 \times 10^{-2}$ (SC-TF) $\mu_h = 4.4 \times 10^{-7}$ (PC-TF)	—	3.2	[144, 145, 149, 151–153]
	$(NH_4)_3Bi_2I_9$	P 2_1/n	—	2.04–2.05	$\mu = 213$ (SC)	~51 600 (SC)	—	[154, 155]
	$Cs_3Sb_2I_9$	$P6_3$/mmc (0D)	1.4/ 1.55 (0D)	2.3–2.5 (0D)	$\mu_h = 6.81$ (2D-TF)	54.29 (0D-TF)	1.49	[21, 156–158]
		$P\bar{3}m1$ (2D)	0.34/ 0.42 (2D)	2.02–2.05 (2D)	$\mu_h = 3.54$ (0D-TF)	6 (2D-TF)		
	$MA_3Sb_2I_9$	$P6_3$/mmc	—	1.92	$\mu_e \sim \mu_h = 16.68$ (SC)	271 (SC)	—	[159, 160]
	$Rb_3Sb_2I_9$	P 2_1/n	1.11/1.55	2–2.24	$\mu = 0.26$ (TF)	8.97 (TF)	1.37	[21, 161–165]
	$K_3Sb_2I_9$	$P\bar{3}m1$	3.15/1.83	2.03	—	29.98 (TF)	—	[21]
ABZ_2 materials	$NaBiS_2$	$Fm\bar{3}m$	0.36/0.25	1.2–1.45	—	—	0.07	[22, 166–168]
	$NaSbS_2$	C 2/c	0.34/0.35	1.5–1.8	$\mu_e = 14 - 22$ (TF)	—	3.18	[169–171]
	$AgBiS_2$	$Fm\bar{3}m$	0.35/0.722	1.15–2.7	$\mu_e = 0.07$ (NC) $\mu_h = 0.032$ (NC)	1670 (QD)	6.4	[172–177]
	$CuSbS_2$	Pnma	~0.3/0.3	1.4–1.9	$\mu_h = 64.6$ (TF)	0.7 (TF)	3.22	[178–183]
	$CuSbSe_2$	Pmna	0.71/0.9	1–1.2	$\mu_h = 20.17$ (TF)	0.19 (TF)	4.7	[184–190]

Table 2. (Continued.)

Material		Space group @ RT	m_e^*/m_h^* (m_0)	Band gaps (eV)	Mobility ($cm^2\ V^{-1}\ s^{-1}$)	Carrier lifetime (ns)	Highest PCE (%)	Reference
Binary halides	InI	Cmcm	0.215/0.118	2	—	6 (SC)	0.39	[18, 107, 191, 192]
	BiI_3	$R\bar{3}$	0.68/2.01	1.67–1.8	$\mu_e = 260$ (SC)	1.3–1.5 (SC)	1.21	[192–196]
	SbI_3	$R\bar{3}$	0.62/1.54	2.1	—	—	—	[192, 197, 198]
V–VI–VII materials	BiOI	P4/nmm	0.19/0.2	1.8–1.93	—	2.7 (SC)	1.8	[199–201]
	BiSI	Pnam	0.53/0.95	1.57	$\mu_e \sim 1$ (SC)	1.03 (TF)	1.32	[202–204]
	SbSI	(approx.) $P2_1P2_1P2_1$	0.65/0.34	1.8–2.72	—	—	3.62	[205–207]
Chalcogenide perovskites	$BaZrS_3$	Pnma	0.43/0.75	1.75–1.85	$\mu_e = 2.1 - 13.7$ (TF)	400 (TF)	—	[23, 208, 209]
	$SrZrS_3$	Pnma	3.11/0.64	1.52–1.53 (α-phase) 2.05–2.13 (β-phase)	—	—	—	[23, 209–211]
	$LaYS_3$	$P2_1/m$	0.49/0.67	2	$\mu \sim 0.009$ (TF)	~30 (TF)	—	[23, 209, 212]

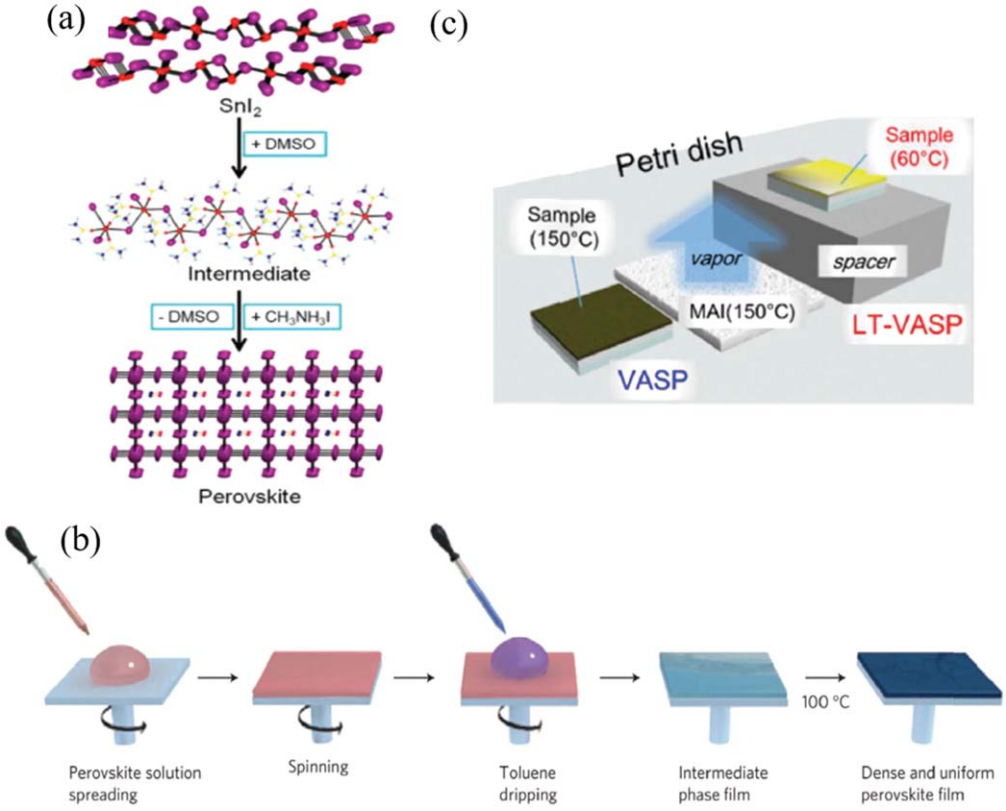

Figure 14. The scheme of (a) one-step solution method, (b) solvent engineering method, and (c) LT-VASP method. [19] John Wiley & Sons. © 2018 WILEY-VCH Verlag GmbH & Co. KGaA, Weinheim.

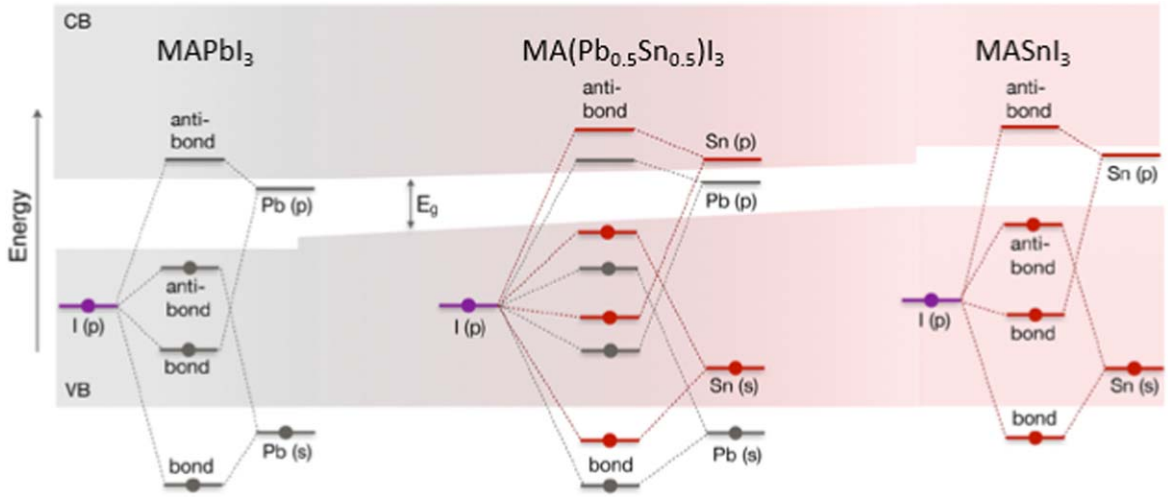

Figure 15. Schematic illustration of band gap bowing in $MA(Pb_{1-x}Sn_x)I_3$ using a molecular orbital diagram to approximate the band structure of the crystal. Reprinted with permission from [227]. Copyright (2018) American Chemical Society.

even with such short carrier lifetimes, Sn-based perovskites can still exhibit long diffusion length over 500 nm [111] mainly due to their high mobilities.

Poor stability is one of the main issues of Sn-based perovskites because Sn^{2+} is prone to oxidation into the more stable Sn^{4+} after exposure to ambient air [19]. A significant reduction in PL lifetime was observed in $FAPb_{0.5}Sn_{0.5}I_3$ films after one-minute of air exposure [230], indicating that Sn-based perovskites should be encapsulated immediately after fabrication in order to maintain their performance. In addition, thermogravimetric analysis (TGA) showed that $MASnI_3$ prepared in air would start to decompose at lower temperature (∼150 ℃) compared to that prepared in a sealed tube or solution (>300 ℃) [110], which is related to the presence of Sn^{4+} and liberation of volatile SnI_4. Nevertheless, both decomposition temperatures are significantly higher than the range of testing temperatures for solar cells (25 ℃ under standard conditions, or 85 ℃ for accelerated degradation

testing), indicating that $MASnI_3$ is sufficiently thermally stable for device applications. Further details on how the stability of Sn-based perovskites could be improved for applications in devices are discussed in section 4.2.

3.2. Ge-based perovskites

There have been few experimental reports of Ge-based perovskites focusing on $AGeX_3$ ($A = Cs^+$, MA^+, or FA^+), in which $X = I^-$ or a mixture of I^- and Br^-. The Ge-based perovskites discussed here exhibit trigonal structure (figure 13), where the distorted GeX_6 octahedra are arranged in a corner-sharing pattern with A cations align along the c-axis.

Solution-based methods are used to synthesize most Ge-based perovskites. For example, $MAGeI_{3-x}Br_x$ ($x = 0$–0.6) solution could be prepared by dissolving MAI, MABr, and GeI_2 in DMF [126]. On the other hand, various Ge-based perovskite precipitates can be obtained by adding different iodide salts (CsI, MAI, or FAI) into the solution containing HI, H_3PO_2 and GeO_2, where H_3PO_2 and GeO_2 acts as the reduction agent and Ge source, respectively [128, 232]. Ge-based perovskite precipitates can be dissolved into DMF to make solutions, and thin films can be fabricated via one-step methods [128] or by using solution engineering methods [126] to improve the film qualities. Unsatisfactory solubility of the precursors in polar solvents is a limiting factor of synthesizing Ge-based perovskites, which may lead to poorer film qualities [128].

$CsGeI_3$, $MAGeI_3$, and $FAGeI_3$ have direct band gaps varying from 1.6 to 2.35 eV with increasing A cation size [128]. These Ge-based perovskites also have strong absorption in the wavelength range between 400 and 600 nm, along with sharp edges. From thermogravimetric (TGA) measurements, Ge-based perovskites were found to exhibit high thermal stability since they tended to decompose at temperature >250 ℃ [128]. However, similar to Sn-based perovskites, Ge-based perovskites also face stability issues in air, which is attributed to the oxidation of Ge^{2+} to the more stable Ge^{4+}. The tendency of Ge^{2+} to oxidize is supported by x-ray photoemission spectroscopy (XPS) measurements, which show the presence of Ge^{4+} in the Ge 2*p* orbital scan [128]. Under ambient conditions, it was shown the absorption of $MAGeI_3$ thin films would drop by over 50% within one day. Kopacic *et al* showed that the addition of Br into $MAGeI_3$ can improve its ambient stability [126], though the films could only maintain one third of its initial absorption after one day.

3.3. Double perovskites

Although In, Sb and Bi are promising low-toxicity substitutes for Pb (see section 2), they tend to form a +3 oxidation state. Direct substitution of these metal cations into the B-site in perovskites would result in a non-perovskite crystal structure forming. This issue can be solved by using a double perovskite structure with the general formula: $A_2B'B''X_6$, where A and X are monovalent cations and halides, respectively. But two Pb^{2+} cations are replaced by a pair of monovalent B′ and trivalent B″ cations. This allows charge neutrality to be maintained in a perovskite crystal structure, which is then comprised of alternating $B'X_6^{5-}$ and $B''X_6^{3-}$ octahedra (figure 13). Examples of B′ cations that have been commonly used experimentally include Ag^+ and Na^+, which are paired with In^{3+}, Sb^{3+} or Bi^{3+} B″ cations. Although double perovskites have a 3D crystal structure, in some cases, the $[B'X_6]^{5-}$ octahedra do not contribute to the density of states at the band-edges and result in 0D electronic dimensionality [71], which may lead to large indirect band gaps and hinder carrier transport. Due to this reduced electronic dimensionality, effective masses for double perovskites usually display anisotropic behavior, though most calculated values are still small (between 0.1 and $0.5m_0$) [20].

Double perovskites can be synthesized through solution processing methods. For instance, polycrystalline Cs_2AgBiX_6 can be obtained by dissolving AgX, BiX_3, and CsX in hydrohalic acid HX/hypophosphorous acid mixed solvents [130]. Double perovskite thin films can then be fabricated via spin-coating or thermal evaporation of as-synthesized powders [233]. On the other hand, the synthesis of hybrid halide double perovskites is more difficult compared to that of inorganic double perovskites owing to the low decomposition and vaporization energies of the organic precursors. Therefore, most hybrid double perovskites were synthesized either by solid-state reaction or hydrothermal methods [141, 142], though these two synthesis routes can apply to other inorganic double perovskites as well [130, 138]. Apart from the bulk crystals, double perovskites can be also synthesized as nanocrystals through hot-injection methods. For example, $Cs_2AgBiBr_6$ nanocrystals would form when Cs-oleate is injected into the organic solvent (oleic acid or oleylamine) containing $BiBr_3$ and $AgNO_3$ at 200 ℃ [234]. The impurities can be reduced by introducing additives (e.g. HBr) as well as controlling the injection temperature. Particularly, Cs_2AgBiI_6 nanocrystals could be obtained via anion-exchange process by injecting TMSI to convert $Cs_2AgBiBr_6$ nanocrystals into the target material [235], even though Cs_2AgBiI_6 is expected to be thermodynamically unstable compared to $Cs_2AgBiBr_6$. Double perovskite solutions can be prepared by dissolving the synthesized products in solvents, such as dimethyl sulfoxide (DMSO), and films are fabricated by spin-coating these solutions following annealing processes. Annealing at high temperature or under low pressure [236] (low-pressure assisted annealing) can give crystalline films without phase impurities. Also, the utilization of antisolvents, such as IPA, during spin-coating has been shown to improve film quality and reduce the root-mean square roughness [131]. The main challenge for preparing double perovskite samples is the high temperature requirement involved in dissolving some insoluble precursors [237] (e.g. AgCl), solid-state reaction [238], or annealing process [239]. This challenge may limit the application of double perovskite devices on substrates intolerant to high temperature (e.g. ITO glass) or their compatibility with other materials.

Most double perovskites have low absorption coefficients (10^2–10^4 cm^{-1} in visible region [133]) at the band-edge due to an indirect band gap (e.g. $Cs_2AgBiBr_6$ or $MA_2AgBiBr_6$) or a parity forbidden band gap (e.g. $Cs_2AgInCl_6$ [240]), which

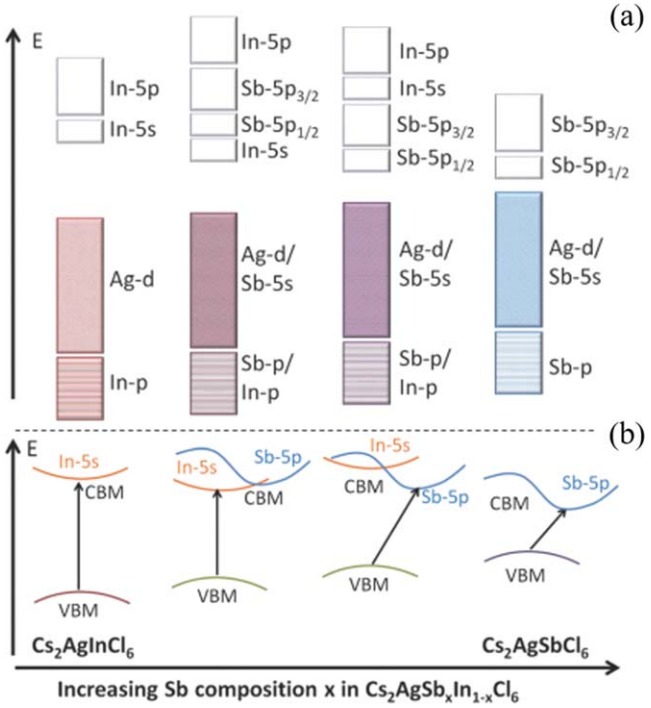

Figure 16. (a) Model band diagrams for $Cs_2AgSb_xIn_{1-x}Cl_6$ and (b) illustration of how the band gap changes due to the contributions from In 5*s* and Sb 5*p* orbitals in the conduction band. Reproduced from [241] with permission of The Royal Society of Chemistry.

limits their SLMEs. For example, $Cs_2AgBiBr_6$, which is the most common double perovskite explored experimentally, has an SLME of 7.9% [42]. Band gaps of double perovskites range from around 2 to 3.4 eV [235], which are too large for PV applications. Band gap engineering is therefore important. Doping or elemental substitution can tune the band gaps. Tran *et al* demonstrated that the band gaps of $Cs_2Ag(Sb_xIn_{1-x})Cl_6$ can decrease with increased Sb content and experience a transition from direct to indirect character [241], which stems from the dominant *p*-orbitals contributed by Sb^{3+} for the hybridization at band-edges, as illustrated in figure 16. In addition, Li, Kavanagh *et al* showed that band gap bowing occurs in $Cs_2Ag(Sb_xBi_{1-x})Br_6$ [75]. The alloy double perovskites exhibited a band gap value of 2.08 eV at $x = 0.9$, which is smaller than $Cs_2AgSbBr_6$ (2.18 eV) and $Cs_2AgBiBr_6$ (2.25 eV). The mechanism for band gap bowing is similar to that of $MA(Pb_{1-x}Sn_x)I_3$ (refer to section 3.1 and figure 15). That is, the lower band gap exhibited by the alloys of $Cs_2Ag(Sb_xBi_{1-x})Br_6$ is due to the energy mismatch between *s* and *p* orbitals from Bi and Sb cations, and their nonlinear mixing.

The investigations of lifetimes and carrier mobilities for double perovskites were mainly focused on $Cs_2AgBiBr_6$. Though trap densities on the order of 10^{16} cm^{-3} are present in $Cs_2AgBiBr_6$ bulk crystals [134], they can be reduced by thermal annealing in N_2 [135]. Annealed $Cs_2AgBiBr_6$ thin films have demonstrated long lifetimes of 1.4 μs [133], which is approaching that of multi-crystalline Si used in commercial solar cells [242]. However, the carrier transport of double perovskites is limited by larger effective masses than in lead-halide perovskites, as well as strong electron–phonon coupling (Refer to section 3.9). Consequently, $Cs_2AgBiBr_6$ single crystals were found to simply exhibit moderate mobilities of 11.81 cm^2 V^{-1} s^{-1} [135].

$Cs_2AgBiBr_6$ can maintain a stable phase in ambient air (with a relative humidity of ~60%) and in the dark for 3 months [135], though significant surface discoloration can be observed after 15 d of light exposure, which possibly stems from the photosensitivity of silver [243]. TGA results also showed that $Cs_2AgBiBr_6$ has higher thermal stability of up to 430 °C, while $(MA)_2AgBiBr_6$ would decompose at around 277 ℃ [142] due to its organic A-site cations. Particularly, double perovskites such as Cs_2InBiX_6, Cs_2CuInX_6 or Cs_2AgInX_6 that include Cu^+, or In^+ as B′-site cations have been confirmed theoretically to be relatively unstable owing to the small ionic radii, higher *d* orbital levels, and redox tendency of these B′ cations [244, 245].

3.4. Chalcogenide perovskites

Chalcogenide perovskites also have the ABX_3 chemical formula, but have the X-site anions replaced by S^{2-}. Owing to their stable crystal structure and smaller band gaps (1.5–2 eV), $BaZrS_3$, $SrZrS_3$, $LaYS_3$ are materials investigated most among chalcogenide perovskites. Due to the small electronegativity between B-site cations and sulfur, these materials tend to have strong covalent B–X bonding elements, which is beneficial to narrowed band gaps and carrier transport. The stronger Coulombic attraction between A^{2+} and $[BS_6]^{8-}$ can also enhance the ambient stability of chalcogenide perovskites. For example, it has also been shown that both $BaZrS_3$ and $SrZrS_3$ samples stored in air showed no significant degradation in structure and physical properties after one year. It is worth mentioning that the −2 charge of the X-site anion now allows B-site cations that are more stable in +4 oxidation state to be used (e.g. Sn^{4+} and Ge^{4+}). As shown in figure 13, $BaZrS_3$ exists in distorted perovskite phase with corner sharing BX_6 octahedra. $SrZrS_3$ may form similar distorted perovskite phase (β phase) or needle-like phase with edge-sharing BX_6 octahedra (α phase) at room temperature depending on the synthesis routes. The crystal structure of $LaYS_3$ is different from 3D perovskite since the oxidation states of A- and B-sites are both 3+. Therefore, $LaYS_3$ tend to form a 2D structure with $[Y_3S_9]^{9-}$ layers extended in the [bc] plane and separated by La^{3+} ions.

Phase pure $BaZrS_3$ can be obtained by sulfurization of $BaZrO_3$ with CS_2 at 1050 °C for 4 h [246]. Alternatively, heating the stochiometric mixtures of ground and cold-pressed BaS and ZrS_2 at 800 °C–1000 ℃ for 15 h under high vacuum can also make $BaZrS_3$ product, though further purification will be required [247]. Niu *et al* also made $BaZrS_3$ powders by heating BaS, Zr, and sulphur pieces with stochiometric quantities in a quartz tube at 600 ℃ for 60 h [210]. I_2 was introduced in this method to act as a catalyst to enhances the reactivity of transition metals. Experimentally, $BaZrS_3$ has direct band gaps of 1.75–1.85 eV [23, 247] with large absorption coefficients was on the order of 10^5 cm^{-1} from UV to visible range. Ti-alloying has been found to

effectively reduce the band gap of $BaZrS_3$ to 1.51 eV [248], resulting a theoretical conversion efficiency up to 32%. $BaZrS_3$ was found to exhibit n-type characteristic with high carrier density between 10^{19} and 10^{20} cm^{-3}, which may arise from excess electrons released when S vacancies form [208]. The Hall mobilities of $BaZrS_3$ thin films were reported to range from 2.1 to 13.7 cm^2 V^{-1} s^{-1} [208], which have been comparable to those of $MAPbI_3$ [249]. The higher mobilities also correspond to larger grain size and better crystallinity of $BaZrS_3$ thin films sulfurized at higher temperature. In addition, a PL at the wavelength accounting for the band gap and a lifetime of around 400 ns were observed in $BaZrS_3$ thin films [208, 210], indicating relatively lower defect density within this material.

$SrZrS_3$ can be synthesized via mixing SrS, Zr and sulfur at stoichiometric quantities along with iodine as catalyst in a quartz tube [210]. α-$SrZrS_3$ and β-$SrZrS_3$ would be obtained after heating the mixture at 850 ℃ and 1100 ℃ for 60 h, respectively. A similar synthesis process was conducted by heating Sr, Zr powders and sulfur at 850 ℃ and 1000 ℃ for 3 weeks to prepare α-$SrZrS_3$ and β-$SrZrS_3$, respectively [211]. α-$SrZrS_3$ and β-$SrZrS_3$ individually exhibits a direct band gap of around 1.53 and 2.05–2.13 eV, and both phases have large absorption coefficients on the order of 10^4–10^5 cm^{-1} in the UV to visible range [23, 210]. Especially, polycrystalline β-$SrZrS_3$ showed a high PL intensity comparable to that of single crystalline CdSe and InP and its highest EQE is even higher than that of CIGS solar cells [210]. A high V_{OC} was thus expected in $SrZrS_3$-based solar cells based on these features.

$LaYS_3$ thin films can be fabricated by the two-step process [23]. At the first step, La and Y atoms were deposited on a substrate via co-sputtering in order to form LaY films. The second step is to sulfurize the deposited LaY films at 950 ℃–1000 ℃ with a H_2S flow at atmospheric pressure. Crovetto *et al* showed that the introduction of O_2 at the first step could result in LaY films with improved morphology and fewer impurities. $LaYS_3$ thin films were found to display a band gap of 2 eV with absorption coefficients on the order of $10^4 - 10^5$ cm^{-1} in the UV to visible range [23]. $LaYS_3$ films also showed a PL intensity higher than that of high-efficiency CZTS thin films, implying their lower defect densities [23]. However, based on the time-resolved microwave conductivity (TRMC) measurement, $LaYS_3$ films demonstrated a low mobility of only 0.009 cm^2 V^{-1} s^{-1} (lower limit) and a relatively long carrier lifetime of 30 ns (upper limit) [212]. These results could be attributed to the presence of highly localized defect states, which has been observed in spatially resolved PL images [212]. Additionally, $LaYS_3$ was found to be an *n*-type material with a low doping density ($\sim 10^{14}$ cm^{-3}) and similar band position with $MAPbI_3$ [212].

Complicated processing and the high processing temperatures are two of the main challenges for synthesizing chalcogenide perovskites and integrating them with other transport layers, where contact materials may diffuse into active layers and form unwanted materials after heating [212]. Consequently, although many potential chalcogenide perovskites have been predicted theoretically, most of them are not yet realized experimentally.

3.5. $A_3B_2X_9$ materials

Owing to the low toxicity and the similar electron configuration with Pb^{2+}, Bi^{3+} and Sb^{3+} might serve as alternatives for the B-site cations in perovskites. To satisfy charge balance, however, an $A_3B_2X_9$ arrangement would be needed. These $A_3B_2X_9$ materials can be considered as defect-ordered perovskites, where only 2/3 of the B-site cations of the perovskites are occupied, thus forming an $A_3B_2\square X_9$ structure. These $A_3B_2X_9$ materials have been found to form two polymorphs. One is the 0D dimer-phase structure consisting of isolated bioctahedral clusters, while the other is 2D layered structure, which forms from general ABX_3 arrangement with the removal of every third B layer along the crystal axis (figure 13). While some materials have a fixed structure, other materials (e.g. $Cs_3Sb_2I_9$) have been found to capable of switching between 0D and 2D structures depending on the processing and composition [250, 251]. Several $A_3B_2X_9$ materials have been investigated as potential absorber layers in future PV devices. These include (i) 0D: $MA_3Bi_2X_9$ (X = Cl, Br, I), $FA_3Bi_2I_9$, $Cs_3Bi_2I_9$, (ii) 0D/2D: $Cs_3Sb_2I_9$, (iii) 2D: $MA_3Sb_2I_9$, $Rb_3Sb_2I_9$, and $K_3Sb_2I_9$, $_{K_3}Bi_2I_9$, $Rb_3Bi_2I_9$, and $(NH_4)_3Bi_2I_9$.

Most $A_3B_2I_9$ materials can be synthesized via solution processing methods, which resemble those used for preparing LHPs. For instance, $MA_3Bi_2I_9$ solutions can be prepared by mixing MAI and BiI_3 in DMF/DMSO mixed solvents [144, 154]. $A_3B_2X_9$ films can be fabricated through spin-coating followed by annealing or solvent engineering methods [21, 151] to promote film crystallization. Some modified methods can be applied to further improve film quality. For instance, the PL lifetime of $MA_3Bi_2I_9$ films can be extended by using vapor-assisted conversion, where high-quality $MA_3Bi_2I_9$ films would form by exposing BiI_3 films to MAI vapor [145]. Various $A_3B_2X_9$ powders can also be prepared by solid-state synthesis, where AX and BX_3 powders can react to form $A_3B_2X_9$ product under ball-milling [146]. To grow $A_3B_2X_9$ single crystals, the Bridgman method is a common synthesis route. In this method, precursors are sealed in an ampoule and placed into in a two-zone furnace, where raw materials would melt in the hot-zone and crystallize in the cold-zone [252]. Other than these general methods, some 0D phase materials can also be synthesized by different methods. $(NH_4)_3Bi_2I_9$ single crystals would precipitate when heating $(NH_4)I$ in a mix of BiI_3/HI for 3 h. Also, high-quality $Rb_3Bi_2I_9$ and $Cs_3Bi_2I_9$ powders could be obtained by solvothermal reactions [152]. Particularly, for materials that can transform between the 0D and 2D phase, 2D polymorphs are usually more desirable for optoelectronic applications since their stacked planes can exhibit higher mobilities. Therefore, although 0D $Cs_3Sb_2I_9$ can be easily synthesized by simple solution processing with antisolvent engineering, more researchers have worked on achieving 2D $Cs_3Sb_2I_9$ via various routes. Singh *et al* employed a vapor-assisted solution processing method to deposit 2D $Cs_3Sb_2I_9$ films [156], which were annealed inside an enclosed bottle filled with SbI_3 vapor to prevent the decomposition of material, as illustrated in figure 17. A similar synthesis was taken in 2D $Rb_3Sb_2I_9$ films [161] as well. Umar *et al* also found that HCl could be used as

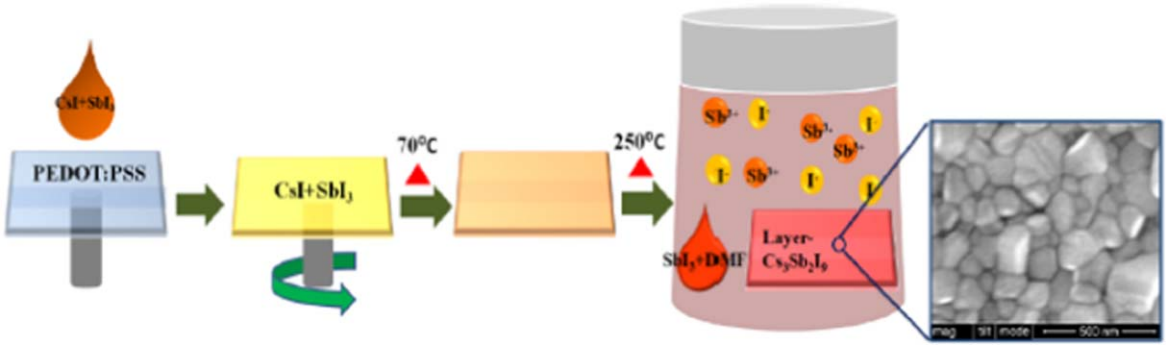

Figure 17. The scheme of vapor-assisted solution-processed method. Reproduced with permission from [156]. Copyright (2018) American Chemical Society.

a coordinated additive to promote the formation of 2D phase $Cs_3Sb_2I_9$ [157]. Recently, another approach found to favor the formation of the 2D phase of $Cs_3Sb_2I_9$ was to alloy with Cl [250]. In addition, by alloying with smaller halides, such as Cl or Br, 0D $Cs_3Bi_2I_9$ was found to be transformed into 2D polymorphs [253, 254], where a complete anion ordering has been shown in some work [253]. 2D $Cs_3Bi_2I_6Br_3$ has been prepared by heating the DMF/DMSO mixture solvent containing stoichiometric mixtures of CsI, BiI_3, and $BiBr_3$ [255]. On the other hand, 2D $Cs_3Bi_2I_6Cl_3$ ingots can be synthesized via a stoichiometric melt reaction of CsCl with BiI_3 at 750 ℃ [254].

Although $A_3B_2X_9$ materials generally have wide band gaps larger than 1.9 eV, large absorption coefficients of up to 10^5 cm^{-1} in the UV–visible region (wavelength <600 nm) have been presented in some of them (e.g. $Cs_3Sb_2I_9$ and $MA_3Bi_2I_9$ [144, 251]). In addition, materials in distinct phases can also demonstrate different band gap characteristic. For instance, it has been shown that 2D $Cs_3Sb_2I_9$ exhibits a direct band gap of 2.05 eV, while its 0D polymorph has an indirect band gap of 2.4 eV [251]. In addition, 2D $Cs_3Bi_2I_6Br_3$ also shows a reduced band gap of 2.03 eV compared with that of 0D $Cs_3Bi_2I_9$ (2.2 eV), which is related to a transition in crystal structures [255]. A gradual decrease in band gap from over 2.6 to 2.06 eV has been observed in 0D $Cs_3Bi_2Br_9$ when alloyed with iodide ($Cs_3Bi_2Br_{9-x}I_x$). This in turn transformed the 0D material into 2 D $Cs_3Bi_2Br_3I_6$ [253].

Apart from $MA_3Bi_2I_9$ and $(NH_4)_3Bi_2I_9$ single crystals, which have demonstrated a high mobility of 70 cm^2 V^{-1} s^{-1} (hole mobility based on the Hall-effect measurement) and 213 cm^2 V^{-1} s^{-1} (sum mobility based on the SCLC method), respectively [147, 155], most $A_3B_2X_9$ materials suffer from poor carrier transport due to the strong electron–phonon coupling (refer to section 3.9) and their low dimensional crystal structures, where carriers can be trapped within the isolated regions of materials. Not surprisingly, 0D $A_3B_2X_9$ materials usually have lower carrier mobilities than the 2D ones. For example, based on the space charge limited current (SCLC) method, 0D $Cs_3Bi_2I_9$ single crystals showed a hole mobility on the order of 10^{-2} cm^2 V^{-1} s^{-1} [153], while 2D $MA_3Sb_2I_9$ single crystals were found to have an electron and hole mobility over 10 cm^2 V^{-1} s^{-1} (or over 40 cm^2 V^{-1} s^{-1} with Sn doping) [159, 160]. Similar differences can be observed between 0D and 2D $Cs_3Sb_2I_9$. It has been verified by the SCLC method that 2D $Cs_3Sb_2I_9$ thin films have a hole mobility of 6.81 cm^2 V^{-1} s^{-1}, which is almost double that in 0D polymorphs [157]. In addition, carrier transport in low dimensional materials can experience significant anisotropy along different axes. For instance, estimated mobility-lifetime ($\mu\tau$) product could vary by over two times under the photoconductivity measurement along *b*- and *c*-axis of $MA_3Bi_2I_9$ single crystals [147]. Additionally, the low dimensionality also leads to large exciton binding energies since excitons could be trapped as well. The exciton binding energies in most $A_3B_2X_9$ materials have been estimated to vary from 70 to 270 meV [21, 144], which are significantly larger than those reported from Pb-based perovskites (25–50 meV) [256, 257] and could make carrier extraction from these materials relatively challenging.

Several $A_3B_2X_9$ materials have shown promising carrier lifetimes. Evaluating from its $\mu\tau$ product, single crystalline $MA_3Bi_2I_9$ and $(NH_4)_3Bi_2I_9$ may have carrier lifetimes up to 40 and >51.6 μs, respectively [147, 155]. Also, a PL lifetime of 271 ns was reported in $MA_3Sb_2I_9$ single crystals [159]. The different polymorphs of $Cs_3Sb_2I_9$ were also found to have different carrier lifetimes due to differences in their defect densities. Based on the SCLC model, 2D $Cs_3Sb_2I_9$ was found to have a trap density of 1.1×10^{15} cm^{-3}, which is almost five times smaller than that of 0D $Cs_3Sb_2I_9$ [157]. Furthermore, 2D $Cs_3Sb_2I_9$ also shows a lower Urbach energy (134 meV) in comparison with 0D $Cs_3Sb_2I_9$ (162 meV), which verifies its less structurally disordered feature [156] (although these values are still significantly higher than that of Pb-based perovskites (~15 meV [258])). However, only a PL lifetime of 6 ns has been reported in 2D $Cs_3Sb_2I_9$ single crystals [156], which is shorter than that of 0D $Cs_3Sb_2I_9$ thin films (54.29 ns) [21]. This result may be related to the presence of deep-level states in 2D $Cs_3Sb_2I_9$ [251].

$A_3B_2I_9$ materials are found to be stable in air. The absorption spectra of $Cs_3Bi_2I_9$ and $MA_3Bi_2I_9$ show negligible changes after one-month storage in dry air in the dark [144]. TGA measurements also shows that $MA_3Bi_2I_9$ and

$(NH_4)_3Bi_2I_9$ hardly decomposes until 250 ℃ and 240 ℃ [145, 154], respectively, indicating they are thermally stable as well. However, though the PXRD patterns for $Cs_3Bi_2I_9$ in ambient atmosphere could maintain unchanged for a few months, that of $K_3Bi_2I_9$ could not keep well after a few hours, which implies that the larger cation sizes may strengthen the stability of crystal structures [152].

3.6. ABZ_2 materials

ABZ_2 materials here refer to ternary chalcogenides, where A = Na, Ag, Cu and other cations with stable +1 charge states, and B-site cations and Z-site anions are generally Sb/Bi and S/Se. These materials are expected to be promising in PV application due to their usage of earth-abundant and non-toxic elements. In this section, we will mainly focus on the discussion of $NaBiS_2$, $NaSbS_2$, $AgBiS_2$, $CuSbS_2$, and $CuSbSe_2$, which have been experimentally investigated. Among these materials, $NaBiS_2$, $NaSbS_2$, and $AgBiS_2$ have a rock salt structure with mixed cations octahedrally coordinated by anions (figure 13). Interestingly, different cation ratios can lead to various superstructures known as 'coloring patterns', which can change their crystal structures and band gaps [22]. Instead of a rock salt structure, $CuSbS_2$ and $CuSbSe_2$ exhibits layered orthorhombic structure composed of SbZ_5 units (figure 13).

$NaBiS_2$ can be obtained by melt synthesis [259], in which powders of S, Bi, and Na_2S are mixed in a sealed tube, followed by a series of heating steps at high temperature for very long reaction time (~9 d). The hydrothermal method [260] can reduce the reaction time by heating $Bi(NO_3)_3 \cdot 5H_2O$, L-cysteine and NaOH in an autoclave at high temperature for around 3 d. Solution-based routes have also been used. For instance, Rosales *et al* used S, NaH, and triphenylbismuth as precursors, and $NaBiS_2$ nanocrystals (NCs) with different sizes can be synthesized with different solvents and reaction parameters [22]. Particularly, $NaBiS_2$ quantum dots (QDs) can be synthesized by the successive ion layer adsorption and reaction (SILAR) technique [166], where QD sizes can be controlled by different concentrations of the precursor solution. $NaBiS_2$ has been found to have an indirect band gap of about 1.2–1.45 eV, in agreement with computations [22]. Absorption measurements of $NaBiS_2$ QDs under different conditions showed that their band gaps increase with the decrease of QD sizes, implying the quantum confinement effect of this material [166], which occurs when QD sizes become comparable with the excitonic Bohr radius of the material. Also, large extinction coefficients over 10^4 cm^{-1} M^{-1} in visible region [22] shows the great potential of $NaBiS_2$ NCs on PV application. On the other hand, Zhong *et al* theoretically proved that $NaBiS_2$ is a ferroelectric material with a large polarization (~33 μC cm^{-2}) [261], which may improve the carrier separation by strong induced field.

$NaSbS_2$ thin films can be synthesized through spray pyrolysis [169], where the precursor solution (Na_2S and Sb_2S_3 in water) is sprayed onto a substrate heated at 230 ℃ to reacted into products. Also, $NaSbS_2$ QDs can be deposited on the mesoporous TiO_2 electrodes via Successive Ionic Layer Adsorption and Reaction (SILAR) followed by post-annealing procedure [262]. $NaSbS_2$ has an indirect band gap of around 1.5–1.8 eV along with large absorption coefficients of about 10^4–10^5 cm^{-1} in the visible range [169, 262]. Rahayu *et al* showed that the overall band gap of QDs-coated TiO_2 will decrease significantly with the increase of SILAR cycles, which is also a result of quantum confinement effect [170]. In addition, Xia *et al* used UPS and Hall effect measurements to demonstrate that $NaSbS_2$ is a weakly n-type material with an electron mobility between 14 and 22 cm^2 V^{-1} s^{-1} [169].

$AgBiS_2$ has been synthesized via several methods in the literature. Earlier reports were usually based on SILAR methods [172] and spray pyrolysis [263]. In addition, $AgBiS_2$ has been grown as nanocrystals (NCs) by hot injection method [264] involving the rapid injection of a sulfur source into the oleic acid solution containing bismuth and silver salts at high temperature. However, hot injection needs to be performed under vacuum, or within inert gas, which is inconvenient and costly. Some researchers thus worked on preparing $AgBiS_2$ NCs at room temperature and under ambient atmosphere. Pejova *et al* showed that $AgBiS_2$ NCs could be easily synthesized through dissolving $AgNO_3$, $Bi(NO_3)_3$, and $Na_2S_2O_3$ in nitric acid, and NC sizes could be reduced under high-intensity ultrasonic irradiation [265]. Recently, Akgul *et al* used air-stable precursors such as AgI and BiI_3 dissolved in amines, and $AgBiS_2$ NCs would form after quickly injecting another sulphur-amine solution [266]. $AgBiS_2$ has been found to have indirect band gaps of about 1.15–2.7 eV, and exhibits high absorption coefficients of around 10^4–10^5 cm^{-1} from visible to near-infrared range [264]. Similar to $NaBiS_2$, tunable band gaps have been observed in $AgBiS_2$ QDs with different sizes [172]. This tunability is also ascribed to the quantum confinement effect when QD sizes approached the excitonic Bohr radius of $AgBiS_2$ (4.6 nm [267]). $AgBiS_2$ also displays disperse band-edges and hence small effective carrier masses [267], which should favor carrier transport. However, only a small carrier mobility less than 0.1 cm^2 V^{-1} s^{-1} and a short diffusion length of 150 nm were reported for $AgBiS_2$ NC thin films by the TRMC method [173]. These poor performances may be resulted from the presence of deep-level defects, which has been predicted to arise from the minor off-stoichiometry of $AgBiS_2$ NCs [268]. Nevertheless, an extremely long carrier lifetime up to 1.67 ms was still seen in $AgBiS_2$ QD thin film based on photoconductivity measurement [174], implying that the defect physics of this material is not yet fully understood.

$CuSbS_2$ thin films can be fabricated by many techniques including thermal evaporation [269], sputtering [270], chemical bath deposition (CBD) [271], electrodeposition [272], ALD [273], solvothermal synthesis [274] and so on. On the other hand, solvothermal [275] and hot injection methods [276] can be also applied on the synthesis of $CuSbS_2$ nanoparticles. This material has been shown to have large absorption coefficients over 10^4 cm^{-1} in the visible region as well as direct band gaps ranging from around 1.4–1.9 eV, depending on various deposition processes [178–180]. DFT calculation also predicted that $CuSbS_2$ tends to exhibit *p*-type

characteristic owing to the presence of dominant Cu vacancies [277] acting as electron acceptors. It also exhibits small carrier effective masses of around 0.3 m_0 [277], leading to a high hole mobility of 64.6 $cm^2\ V^{-1}\ s^{-1}$ [181]. Yang *et al*'s work also demonstrated that $CuSbS_2$ may be defect tolerant owing to higher formation enthalpies for deep-level defects and the shallow transition level of Cu vacancies [277]. However, $CuSbS_2$ thin films were found to have a carrier lifetime of only 0.7 ns even after the improvement on film quality via thermal treatment [182, 278].

$CuSbSe_2$ thin films can be deposited through evaporation [279], co-sputtering of Cu_2Se and Sb_2Se_3 [184], sulfurization of Cu-Sb alloy [180], and electrodeposition [280]. Particularly, Yang *et al* also fabricated $CuSbSe_2$ by the hydrazine method, which involved the preparation of precursors such as Cu_2S, Sb_2Se_3 in hydrazine with specific stoichiometry [185]. In addition, it has been shown that $CuSbSe_2$ single crystals could also be synthesized by the hot-injection technique [281]. One main challenge within these methods is that several competitive phases may occur concomitantly, making pure phase $CuSbSe_2$ can be obtained only under strictly controlled environment [185, 186]. $CuSbSe_2$ has direct band gaps of 1–1.2 eV [185], which is close to the optimal band gap for single-junction solar cells. Moreover, Tiwari *et al* showed that $CuSbSe_2$ also exhibits large absorption coefficients up to $6.6 \times 10^6\ cm^{-1}$ in the visible region [282], indicating its potential as a solar absorber. Similar to $CuSbS_2$, a *p*-type characteristic caused by Cu vacancies is also observed in $CuSbSe_2$ with a high hole concentration over $10^{17}\ cm^{-3}$ being reported [184]. However, the larger effective hole mass ($0.9m_0$ [187]) of $CuSbSe_2$ may lead to a lower Hall mobility of 20.17 $cm^2\ V^{-1}\ s^{-1}$ [188] compared to $CuSbS_2$. Though Xue *et al* predicted that $CuSbSe_2$ would have benign defect properties [188], Welch *et al* indicated that Se vacancies could serve as deep-level defect states that may influence the carrier lifetime, which has been confirmed by a short carrier lifetime of 190 ps measured via transient THz spectroscopy technique [186].

In terms of stability, it has been claimed that $AgBiS_2$ and $NaBiS_2$ are stable in air for at least several weeks [22, 264]. No obvious degradation issues have been reported in the literature for other ABZ_2 materials, but Peccerillo *et al* believed that Cu-related instability resulted from ions migration under continuous DC operation may occur in Cu-based ABZ_2 materials [283].

3.7. Binary halides

Binary halides are compounds made from heavy metals and halides, which contain cations with valence s^2 electrons, making them promising for potentially exhibiting defect tolerance (refer to section 2). InI, BiI_3, and SbI_3 have been investigated most as PV materials among all binary halides, and we will focus our discussion on them. InI has an orthorhombic crystal structure with layers stacked along the *b*-axis [191] (figure 13), and every two atom sheets are staggered in this structure, making In atoms bonded more closely with adjacent In atoms. On the other hand, BiI_3 and SbI_3 exhibit layered structures [26, 193] with each layer composed of edge-sharing metal-halide octahedra bonded together by van der Waals interactions.

InI films can be deposited by thermal evaporation [107], or fabricated from the melt [18], where the In metal-I pellets mixture was placed into a quartz ampoule and heated at 400 °C for 12 h to ensure the complete reaction into InI. Alternatively, Shah *et al* used the Bridgman method to grow InI single crystals by placing purified InI into a vertical furnace kept at 450 ℃ but with a sharp temperature drop at the bottom, where melted InI can crystallize as molten InI moved down [284]. InI has a direct band gap of around 2 eV, which has been verified in calculation and experiment [107]. It has been reported that InI can exhibit reasonably long PL lifetime over 6 ns [18] and large mobility-lifetime products corresponding to a diffusion length of around 16 μm [107]. Defect calculations also suggest that the main vacancies and anti-site defects do not have transition levels resonant within the band gap, or have high formation energy transition levels that involve a large gradient change (which would have a low capture cross-section) [285]. However, In is not stable in the +1 oxidation state and tends to oxidize to the +3 oxidation state. InI films have been found to decompose under ambient conditions within 3 h [107].

BiI_3 thin films have been synthesized by physical vapor transport (PVT) [194], physical vapor deposition (PVD) [286], and solution processing [287]. On the other hand, BiI_3 single crystals can be obtained by the vertical Bridgman method [288] similar to that was described in InI section. It is worth noting that BiI_3 tends toward dissociation at 250 °C–300 ℃ [289, 290], which limits its synthesis to some extent. BiI_3 has indirect band gaps of around 1.7–1.8 eV with large absorption coefficients ($>10^5\ cm^{-1}$ above 2 eV) [194, 288]. BiI_3 single crystals have demonstrated the electron mobility as high as 260 $cm^2\ V^{-1}\ s^{-1}$ (or 1000 $cm^2\ V^{-1}\ s^{-1}$ with Sb doping) [195, 291], though the hole mobility was estimated to be much lower due to relatively large effective hole mass ($2.01m_0$). Furthermore, a long electron diffusion length of 4.9 μm estimated from the large $\mu\tau$ product as well as a PL lifetime of 1.3–1.5 ns was obtained from BiI_3 single crystals [194], indicating the potential of BiI_3 as a great PV material. BiI_3 films are also stable in air. For instance, Hamdeh *et al* have demonstrated that they could stand against oxidation for several months or withstand several hours of annealing without degradation [287]. In addition, Du *et al*'s work showed that the large Born effective charge of BiI_3 could result in its large dielectric constant of around 54 [292], which can Coulombically screen charged defects.

SbI_3 single crystalline plates could be grown from vapor phase [197] directly or by Bridgman method [293]. Particularly, SbI_3 microcrystals could be obtained by the incorporation with Y-zeolite faujasites via sublimation [293]. In addition, Mohan *et al* also fabricated SbI_3 films by iodizing evaporated Sb films [294]. Kepinska *et al* showed that SbI_3 has a temperature dependent indirect band gap [197], which is around 2.1 eV at room temperature. Virko *et al* proved that this band gap would be blue-shifted when the deposited SbI_3 clusters became smaller, which implies the quantum

confinement effect of this material [293]. BiI_3 also demonstrates rather large absorption coefficients in visible region on the order of 10^5–10^6 cm^{-1} [197]. However, SbI_3 single crystals were found to have an Urbach energy over 200 meV at room temperature [197], indicating that several defect states may exist within the band gap.

3.8. V–VI–VII materials

V–VI–VII materials are materials made from elements of V, VI, and VII group, which may be Bi/Sb, O/S/Se, and halides, respectively. Similar to binary halides, V–VI–VII materials also have antibonding orbital character at the band-edges along with strong SOC, which are therefore promising for potentially exhibiting defect tolerance. At present, BiOI, BiSI, and SbSI are the compounds studied the most. Both BiOI and BiSI have a layered structure (matlockite tetragonal system [199, 200]), where I–Bi–O/S–Bi–I layers are stacked along the c-axis and linked by weak van der Waals interactions (figure 13). On the other hand, SbSI has a needle-like crystal structure with long chains growing along the (001)-axis [295]. Strong anisotropy can be seen in V–VI–VII materials due to their low dimensionality and may be reflected in many features. For example, the effective hole mass can differ by over 3 times as along different axes of BiOI [200], which also leads to the anisotropy in its carrier transport.

BiOI polycrystalline thin films can be fabricated by chemical vapor deposition (CVD) [201, 296] or the SILAR technique [297]. Owing to the 2D structure, BiOI thin films exhibit a textured morphology. For example, CVD BiOI grown on solution-processed NiO_x have a {012} preferred orientation. It was recently shown that this could be controlled through the vaporization temperature of the BiI_3 precursor and the growth temperature, which influence whether growth is nucleation or kinetically-dominated [298]. The preferred orientation of BiOI films can then be changed from a/b-axis to c-axis, which results in a denser morphology.

BiOI has an indirect band gap of 1.8–1.9 eV with absorption coefficients larger than $10^4\,cm^{-1}$ from UV to visible range [201, 299]. Computed defect diagrams showed that the defects with the lowest formation energy have shallow transition levels [201], which was consistent with experiments. It has been showed that the electronic structure, PL intensity and charge-carrier lifetime are robust against percent-level defects [300]. Furthermore, a high dielectric constant of 45 was found through computations [201], and this can help to screen charged defects. The PL lifetime measured was 2.7 ns [201]. Although this is sufficient for further exploration in solar absorbers [18], it is shorter than the lifetime of lead-halide perovskites. Recently, photo-induced current transient spectroscopy measurements showed that BiOI films have deep traps located at 0.3 and 0.6 eV from the band-edge [300], but their origin have not yet been identified. BiOI has improved air stability over lead-halide perovskites, with no change in phase over the entire 197 d testing period [201].

BiSI polycrystalline thin films can be synthesized by various methods such as single-precursor solution processing [202], spray pyrolysis [301], asynchronous ultrasonic spray pyrolysis (APUSP) [302], hydrothermal [303] and solvothermal methods [304]. APUSP here used two ultrasonic humidifiers to deliver two nebulized solution onto a hot substrate subsequently to improve the film morphology. On the other hand, BiSI single crystals can be synthesized by a gel process [305] or the sublimation of BiSI polycrystals [203]. One key challenge of depositing BiSI films is the competition from other Bi–S–I phases [306], which is verified from the isothermal section of this ternary system. BiSI has a nearly direct band gap of around 1.6 eV with absorption coefficients of around 10^4 cm^{-1} in UV and visible range [301]. Though the effective electron mass is small for BiSI [202], Sasaki *et al* have shown that this material may exhibit an electron drift mobility of only 1 $cm^2\,V^{-1}\,s^{-1}$ along the c-axis [203]. Moreover, Hahn *et al* also estimated a mean hole diffusion length of only 5×10^{-6} cm [301], which arises from its larger hole effective mass ($0.95m_0$ [203]). In addition, a short PL lifetime of about 1.03 ns was also obtained from BiSI thin films [202], implying the presence of deep-level sulfur vacancies. BiSI is also a semiconductor exhibiting ferroelectricity, piezoelectricity and photoconductivity, and hence is an appealing material in various fields [307].

SbSI films can be prepared by hydrothermal methods [308] or simple solution processing methods [309]. In addition, SbSI single crystals can be synthesized via the vertical Bridgman technique [310] or CVT [311]. Due to the anisotropy of SbSI, it is still difficult to fabricate large-area and uniform single crystalline samples. SbSI has indirect band gaps of around 2 eV [309, 312], which may be blue-shifted when the temperature decreases [310]. The ferroelectricity of SbSI also leads to the large static dielectric constant of the order of 10^4 at 292 K [313], which is beneficial for screening charged defects. In addition to the ferroelectricity, SbSI also has high photoconductivity and piezoelectricity [314] and is as appealing as BiSI.

3.9. Strong electron–phonon interactions and self-trapped excitons

Although Sn-based perovskites have demonstrated high mobilities exceeding 500 $cm^2\,V^{-1}\,s^{-1}$ in single crystals [249], the mobilities of other PIMs are more modest. This is partly due to reduced band dispersion in many cases, particularly in compounds with layered, 1D or 0D structures. Another important factor, however, is electron–phonon coupling. Charge carriers can couple with phonons (quanta of lattice vibrations) via polarization of the lattice ions, inducing a localized structural distortion. Meanwhile, the movement of charge carriers can be constrained by these distortions, and the term 'polaron' is used to describe the charge carrier coupled to the crystal vibrations. It has been verified that strong electron–phonon coupling occurs in $A_3B_2X_9$ materials [252], double perovskites [124, 315], and binary halides [316]. Owing to the polar nature of these materials, Fröhlich interactions are expected, in which charge-carriers couple to longitudinal optical (LO) phonons [317]. Optical phonons involve out-of-phase lattice movements, resulting in electric

fields which interact with the charge-carrier via polarization effects [318]. The strength of this electron–phonon coupling is described by a dimensionless coupling constant, α, which is given by equation (5) [319]:

$$\alpha = \frac{q^2}{\hbar c}\sqrt{\frac{m_b c^2}{2\hbar\omega_{LO}}}\left(\frac{1}{\varepsilon_\infty} - \frac{1}{\varepsilon_0}\right). \quad (5)$$

In equation (5), q is the charge of an electron, $\hbar$ the reduced Planck constant, c the speed of light, m_b the effective mass of the charge-carrier in the absence of lattice interactions, ω_{LO} the rotational frequency of the longitudinal optical phonon mode, and ε_∞ and ε_0 the optical and static dielectric constants, respectively [319]. A coupling constant larger than 2 is considered to be strong, with larger coupling constants yielding increased polaron (carrier) effective masses, thereby significantly limiting the mobilities. In $Cs_2AgBiBr_6$ for example, the Fröhlich coupling constant has been calculated to be 2.54 for electrons and 2 for holes [315], showing the presence of strong electron–phonon coupling in this double perovskite material. This electron-lattice interaction can also be quantified through the Huang–Rhys factor, S, which indicates the average number of vibrations emitted after an optical transition between excited and ground states [315]. The Huang–Rhys factor for $Cs_2AgBiBr_6$ has been measured to be high, at 11.7–15.4 [315, 320]. As a result, the mobilities of $Cs_2AgBiBr_6$ single crystals have been measured to only reach 11.81 $cm^2\ V^{-1}\ s^{-1}$, well below lead- and tin-based perovskites [133, 249]. Beyond reducing the mobility, Fröhlich interactions also result in a temperature-dependent widening in the photoluminescence peak [317].

Similar to polarons, excitons are also quasiparticles that can arise in semiconductor crystals, and which can have significant effects on optoelectronic behavior [321, 322]. Excitons are Coulombically-bound electron–hole pairs which are produced by band-edge excitations. The attraction of the oppositely-charged electron and hole results in a stabilization of the excitonic state relative to that of free charge carriers, termed the exciton binding energy (E_b).

The exciton binding energy (E_b) and diffusion length (L_D) are two closely-related parameters which are often used to characterize excitonic behavior in materials [321–324]. Excitons with low E_b (on the order of kT) are termed Wannier–Mott (or free) excitons and are relatively mobile in the crystal, thus exhibiting large exciton diffusion lengths. On the other hand, Frenkel excitons are those which exhibit high E_b (approx. 100–1000 meV), extremely short diffusion lengths and are typically confined to a single unit cell, drastically inhibiting charge transport.

For photocurrent applications (such as PV, photodetectors and photocatalysts) [325], excitons must first be dissociated into 'free' charge carriers to allow charge extraction and current generation to occur [323, 326]. In contrast, for photoluminescence applications (i.e. LEDs), excitons can benefit device performance by facilitating efficient radiative recombination [321]. Therefore, low binding-energy, Wannier–Mott-type excitons are desirable in PV devices (being readily dissociated into free carriers by thermal energy), and these have been observed as the dominant excitonic species in 3D lead-halide perovskites and silicon, and co-exist with free carriers [326–328].

For PV materials with large E_b, such as organic semiconductors and low-dimensional perovskites, strategies to overcome poor charge separation and transport must be employed in order to maintain device performance [322, 323, 329]. Often, the introduction of heterojunctions, to facilitate exciton dissociation, and use of extremely thin devices, to counteract the extremely-short L_D, are necessary. Beyond these effects, excitons can also affect absorption properties, with high E_b materials exhibiting an excitonic peak in the optical absorption spectrum below the band gap of the material.

While excitonic behavior has been well-studied in the lead-halide perovskites, with low binding energies of a few meV at room temperature observed, initial investigations of excitons in PIMs have indicated larger binding energies in these systems, primarily due to reductions in carrier effective mass, structural dimensionality and/or dielectric screening. For instance, investigations of $A_3B_2X_9$ compounds with 0D crystal structures have reported E_b values in the range of 170–370 meV, attributed to carrier localization within the isolated $[B_2X_9]^{3-}$ bi-octahedra [21, 254, 330, 331]. Lower binding energies of approx. 100–120 meV are witnessed for $A_3B_2X_9$ materials exhibiting two-dimensional crystal structures, e.g. $K_3Sb_2I_9$ and $Rb_3Sb_2I_9$ [21]. Wannier–Mott binding energies on the order of 100 meV have also been calculated for vacancy-ordered double perovskites (A_2BX_6 materials)—specifically K_2SnI_6 in this case, which have strong band dispersion despite being crystallographically zero-dimensional, due to close-packing of the lattice [332, 333].

As with polarons, excitons may also interact with phonons. This coupling is similar to electron–phonon coupling discussed earlier in this subsection. Such interactions can result in the exciton localizing in the lattice in the absence of defects due to distortions in the lattice [334] (e.g. Jahn–Teller distortions [124]). This is referred to as intrinsic self-trapping (figure 18(a)). These self-trapped excitons (STEs) can be considered to be defect states, but unlike lattice defects, STEs are only created after excitation. Moreover, if the exciton occurs in the vicinity of a permanent defect, it will form an extrinsic STE that is trapped at different energies compared to those of intrinsic STEs. Schematic images of three trapping conditions are displayed in figure 18(a). As discussed above, this behavior limits mobilities and acts as a loss channel for photogenerated carriers. Multiple excited states relative to the ground state will be also generated as coupling occurs, as illustrated in figure 18(b). These excited states will exhibit a large equilibrium position offset relative to the free exciton (FC) state, and this offset is proportional to the Huang–Rhys parameter. As a result, a broadband white light emission with large Stokes shift is usually observed in the materials [124, 335].

Beyond $Cs_2AgBiBr_6$, strong coupling has also been identified in $A_3B_2X_9$ materials. For example, $Cs_3Sb_2I_9$ was found to have a Huang–Rhys factor as high as 42.7. It is proposed that this strong electron–phonon coupling resulted in the formation of STEs and in turn gave the broad PL peaks

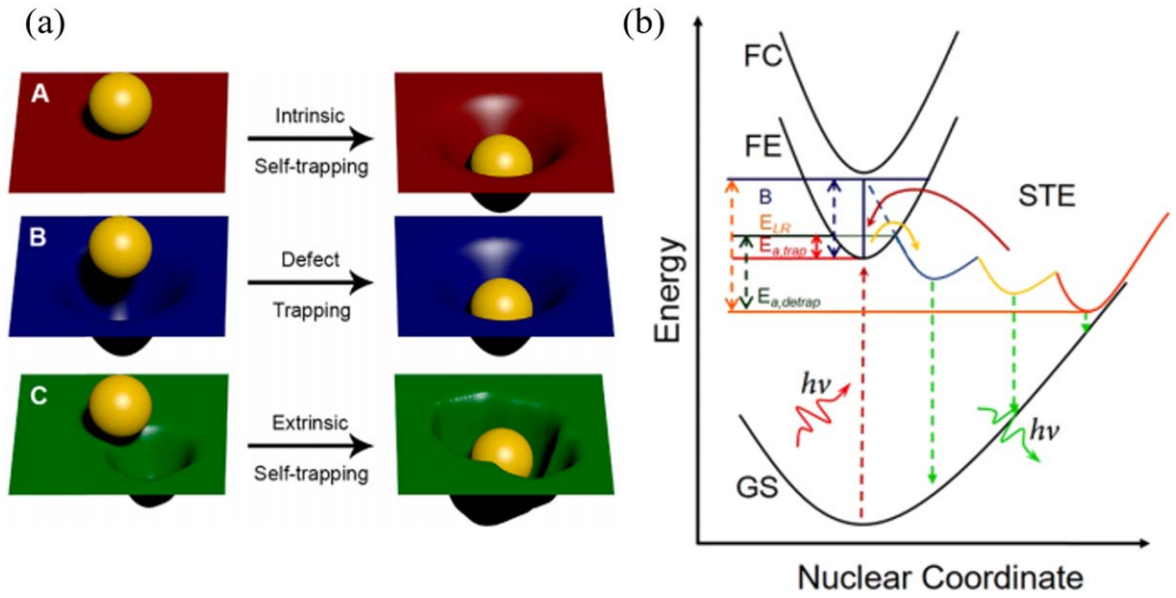

Figure 18. (a) Schematic illustrations of (A) intrinsic self-trapping, which is created as an exciton induces a lattice distortion, (B) defect trapping, which is created as an exciton is trapped within a permanent defect and (C) extrinsic self-trapping, which is created as an exciton induces a lattice distortion near the edge of a permanent defect. Reprinted with permission from [334]. Copyright (2018) American Chemical Society. (b) Band diagrams for STE states, where FC, FE, and GS refers to the state of free carrier, free exciton, and ground state, respectively. Reprinted with permission from [335]. Copyright (2019) American Chemical Society.

observed [252]. Luo *et al* fabricated an alloyed $Cs_2(Ag_{0.6}Na_{0.4})InCl_6$ double perovskite [124] and observed that its PL showed a linear dependence on the excitation power with the PLQEs almost unchanged. This result verified the existence of STEs since permanent defects will encounter the saturation effect, where none of carrier transitions occurs after all defect states are filled at high power excitations. They also demonstrated that though Na ions could break the inversion symmetry of $Cs_2AgInCl_6$ and improve the PLQE to some extent, too many Na ions might force the excited states to cross ground state, leading to non-radiative recombination through phonon emission. Other important features regarding white light emission have been investigated in low-dimensional perovskites. For instance, Cortecchia *et al* indicated that the white light emission intensity will increase at lower temperature due to the thermal energy is not comparable to the de-trapping energy ($E_{a,detrap}$ in figure 18(b)), but it will decrease when the temperature is down to below ~80 K since the thermal energy is even less than self-trapping energy ($E_{a,trap}$ in figure 18(b)). These materials featuring white light emission with large Stokes shift will not suffer PL self-absorption and thermal quenching, which are suitable for the white light LED applications.

4. Engineering of photovoltaic devices—strategies and challenges

Two common device structures are used: n-i-p and p-i-n. In the n-i-p structure, the active layer is grown over an electron transport layer (ETL) covering the transparent conducting oxide. A hole transport layer (HTL) and a high-work function top electrode is deposited over the active layer (vice versa for p-i-n). These device structures can be divided into planar and mesoporous structures. The planar structure only needs a compact ETL, but the mesoporous structure uses a mesoporous scaffold (typically comprised of TiO_2 nanoparticles) deposited on a thin compact ETL (TiO_2 thin film). The active layer will then incorporate into the mesoporous scaffold, which improves carrier transfer. These device structures are illustrated in figure 19.

The stability of PV devices is a critical consideration for commercial applications. However, publications usually lack consistency in terms of testing procedures and parameters reported. To resolve this issue, protocols have been developed for stability testing. For commercial silicon solar cells, the protocol IEC (International Electrochemical Commission) 61215-1-3:2016 is commonly used (refer to the Introduction) [336]. At the lab level, protocols developed by the International Summit on Organic Photovoltaic Stability (ISOS) are commonly used [337]. These were initially developed for organic solar cells, but were more recently adopted for perovskite solar cells as well. The ISOS protocols are categorized into 5 stress conditions (dark storage testing, outdoor testing, light soaking testing, thermal cycling testing, light-humidity-thermal cycling testing). Additional testing procedures specific to perovskite solar cells (PSCs), such as light-dark cycling and testing under continuous bias in the dark, have been added to these protocols. It is suggested that the stability of PIM-based solar cells can be evaluated according to similar protocols as well to resolve the large discrepancies in testing procedures that are present in the literature.

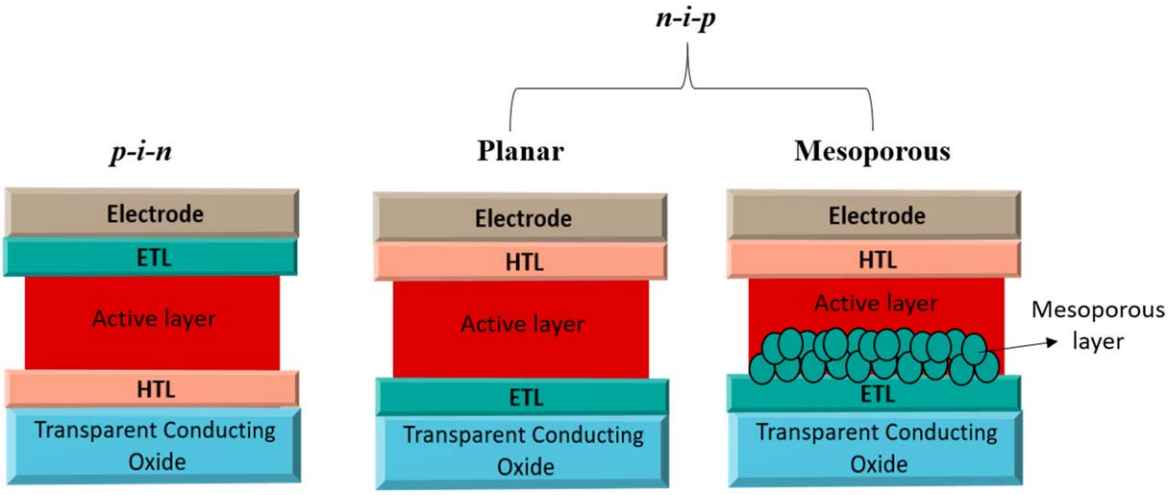

Figure 19. Illustration of the most common device structures used for perovskite-inspired materials.

In this section, we will first briefly review the progress of lead-halide PSCs before focusing the discussion on PIM-based photovoltaics. We discuss the architectures used in PV devices of each class of PIMs, and the device performance and stability achieved. Finally, an overview of the current challenges and limiting factors will be presented.

4.1. Lead-halide perovskites

As mentioned in section 1, lead-halide PSCs have made enormous progress, demonstrating rapid increases in PCE after only a decade of research [6]. One of the factors driving the rapid learning rate demonstrated in perovskite PVs is the rapid evolution in device architecture.

In 2009, $MAPbI_3$ and $MAPbBr_3$ were used in a dye-sensitized solar cell configuration, with the halide perovskite thought of as a replacement for the dye. These devices used a liquid electrolyte solution (LiBr and Br_2 dissolved in acetonitrile) [6]. However, this configuration was hardly used later due to the poor stability of lead-halide perovskites in contact with the liquid electrolyte. Kim *et al* proposed a mesoporous $MAPbI_3$ PSC with a solid 2,2′,7,7′-tetrakis(*N*,*N*-di-*p*-methoxyphenyl-amine)9,9′-spirobifluorene (spiro-OMeTAD) HTL [338]. This device not only showed an enhanced PCE of 9.7%, with an open-circuit voltage (V_{OC}) of 0.88 V and short-circuit current density (J_{SC}) of 17 mA cm^{-2}, but also improved stability, with minimal change in the PCE after 500 h illumination under 1-sun in air. In the same year (2012), Lee *et al* surprisingly found that a hybrid $MAPbI_xCl_{3-x}$ PSC with PCE over 10% can be achieved when replacing the mesoporous TiO_2 with an insulating mesoporous Al_2O_3 scaffold [339]. Their work indicated that electrons diffuse faster in $MAPbI_xCl_{3-x}$than in TiO_2 and fewer sub-gap defect states exist in Al_2O_3, which enables improvements in the J_{SC} and V_{OC} of the device. Later, due to the discovery of fast carrier transport and long diffusion lengths within lead-halide perovskites [340], PSCs fabricated in either a p-i-n or n-i-p structure with thicker (∼500 nm) perovskite layers were intensively investigated. In 2013, Liu *et al* used dual-source evaporation to fabricate a planar $MAPbI_xCl_{3-x}$ PSC that demonstrated a PCE of 15.4%, a V_{OC} of 1.07 V, and a J_{SC} of 21.5 mA cm^{-2} , indicating that the mesoporous scaffold is not completely necessary for efficient PV devices [341]. More recently, in 2019, Yoo *et al* reported a solution-processed $(FAPbI_3)_{0.92}(MAPbBr_3)_{0.08}$ PSC with a mesoporous scaffold, and with the surface of the 3D perovskite passivated with a layered perovskite, which resulted in PCEs of 23.4% along with a record low V_{OC} loss of only ∼0.34 V [342]. On the other hand, Tang *et al* adopted [6,6]-phenyl-C61-butyric acid methyl ester (PCBM)/C_{60} and 2,9-dimethyl-4,7-diphenyl-1,10-phenanthroline (BCP) as the ETL and NiO nanocrystals as the HTL to reduce the scattering loss in p-i-n $MAPbI_3$ PSCs, which led to a PCE of 15.47%, a V_{OC} of 1.06 V, and J_{SC} of 19.41 mA cm^{-2} [343]. It is worth mentioning that although the lead-halide PSCs have shown comparable PCEs to that of silicon solar cells, there is still significance space for further improvements in PCE.

To further increase the PCEs and overcome the SQ limit for single-junction PSCs, perovskite-based tandem photovoltaics have gained attention. A perovskite tandem combines one PSC as the top cell with another device as the bottom cell. The bottom cell absorber needs to have a lower band gap E_g than the perovskite used in the top cell (E_g of 1.55–1.8 eV usually), and examples include crystalline Si (E_g of 1.1 eV) [13, 344], copper indium gallium selenide (CIGS) (E_g of 1.2 eV) [345, 346], PbS colloidal quantum dots (E_g ∼ 0.5–1.3 eV) [347, 348] or another lower-bandgap PSC (E_g ∼ 1.25 eV) [349, 350]. These devices allow higher PCEs compared to single PSCs since the bottom cells can absorb the photons with lower energy in the solar spectrum that cannot be absorbed by lead-halide perovskites. The two sub-cells can either have the top-cell mechanically stacked over the bottom-cell (four-terminal tandem) or integrated together into one device (two-terminal tandem). Since their first report in 2014 [351], perovskite-based tandems have made rapid progress in terms of efficiencies. Chen *et al* reported four-terminal $Cs_{0.05}FA_{0.81}MA_{0.14}PbI_{2.55}Br_{0.45}$/Si tandems with

improved surface morphology on the perovskite layer, and achieved a PCE of 28.2% [347]. A PCE of up to 29.15% was also reported in a two-terminal perovskite/Si tandem in 2020 [7].

Although perovskite tandems have presented great potential in terms of PCEs, the multiple layers incorporated in these cells also lead to severe optical losses, such as due to unwanted reflection between layers with large differences in refractive index [352]. Therefore, light management techniques, which are well-established in the modern semiconductor industry, have been applied to perovskite/Si tandems. A micron-scale pyramidal structure can be formed on the surfaces of the silicon bottom cells via chemical etching in order to reduce reflection losses. This texturing can be adopted in a two-terminal tandem by growing the perovskite top-cell conformally over the textured silicon bottom cell, such as through thermal evaporation [344]. Tandems textured on one side or on both sides have been adopted and demonstrated significant improvement in efficiencies over planar tandems [13, 344, 353]. Optical losses in tandems can also be achieved through the use of light management foils (e.g. viscous lacquer fabricated by UV nanoimprinting lithography) or by depositing anti-reflection coatings (e.g. LiF or MgF_2) on the front side of the top cell with optimal thickness. The application of light management foils or antireflection coatings on planar tandems has led to improvements in the PCE by 1.1% and photocurrents by over 10% [354, 355].

It should be noted that the PCE of perovskite solar cells has been shown to be dependent on the test method used (e.g. scan direction and speed in the measurement of an *I–V* curve) [356, 357]. One of the main causes of these deviations is the facile ion conductivity of lead-halide perovskites, which strongly contributes to hysteresis in *I–V* curve measurements. Some of the factors influencing the degree of hysteresis include the device architecture, thickness of TiO_2, and scan rate [356]. The origin of hysteresis of PSCs is still under debate, but it has been shown that a bad solar cell can be 'made to look good' simply through improper testing methods (e.g. by taking fast reverse scans) [356, 358]. There has therefore been significant effort to identify how to reliably measure the correct efficiency of a PSC, and to standardize measurement and reporting protocols. For instance,

1. The stabilized power output should be recorded by tracking the maximum power point of the device over several minutes of continuous illumination.
2. The J_{SC} calculated by integrating the incident photon to current efficiency (IPCE) spectrum should not deviate from the measured J_{SC} by more than 20%.
3. Biasing a PSC at a voltage higher than V_{OC} before a *J–V* scan could lead to large measurement errors and should be avoided.

It is worth mentioning that PV devices based on PIMs may face similar issues as PSCs, and many researchers have adopted the best practices developed for lead-halide perovskite PSCs.

The toxicity of lead in lead-halide perovskites remains as a potential issue for commercialization. We note that although photovoltaics are exempt from the Restriction of Hazardous Substances directive, the lead in perovskites is present in a soluble form that may be easily accessible. To reduce the lead leakage when modules are damaged or penetrated by water, encapsulation may be the most widely employed approach. It has been shown that perovskite modules encapsulated by epoxy resin can effectively reduce the lead leakage rate down to 0.08 mg h^{-1} m^{-2} under simulated sunny weather conditions [359]. Alternatively, coating lead-adsorbing materials, such as films of *P*,*P*′-di(2-ethylhexyl)methanediphosphonic acid (DMDP) on each side of PSCs, can also sequestrate more than 96% of leaked lead [360]. In addition, recycling lead-containing liquid solvent generated during PSC fabrication has been shown to be a viable strategy. For instance, iron-incorporated hydroxyapatite exhibits a strongly charged surface that can effectively absorb lead ions in solvent, and the magnetism introduced by iron enables the easy collection of lead-absorbed products [361]. As a result, 99.7% of leaked lead can be recycled.

4.2. Sn-based perovskites

PV devices with Sn-based perovskites have been fabricated in the n-i-p (planar and mesoporous) and p-i-n structures. For the planar structure, although the diffusion length of Sn-based perovskites can be very long, it is still challenging to make devices based on this structure owing to the requirement of high film quality (compact film morphology and low pinhole density). Trimethylamine (TMA) was found to be an additive that can improve the film quality of $FASnI_3$, and a PCE of 4.34% with a V_{OC} of 0.31 V, and a J_{SC} of 21.65 mA cm^{-2} in planar $FASnI_3$ solar cells was achieved [362].

On the other hand, the most common architectures used in Sn-based perovskite PV devices is the mesoporous structure. The so-called hollow solar cells based on mesoporous structure were found to demonstrate improved performance over planar devices [113, 363]. In these devices, ethylenediammonium (en) was incorporated to replace parts of A-site cations in Sn-based perovskites, which would create several SnI_2 vacancies and change the electronic structures of perovskites. As a result, hollow solar cells could demonstrate better film morphology and lower defect densities (estimated from the trap-filled limited voltage from SCLC measurement) compared to neat solar cells, leading to an improved PCE and V_{OC}. Consequently, hollow {en}$FASnI_3$, {en}$MASnI_3$, and {en}$CsSnI_3$ solar cells have shown the highest PCE of 7.23%, 6.63%, and 3.79%, respectively among mesoporous PV devices [113, 363].

Several p-i-n Sn-based perovskite solar cells have demonstrated high PCEs. Shao *et al* fabricated p-i-n $FASnI_3$ solar cells with poly(3,4-ethylenedioxythiophene):polystyrene sulfonate (PEDOT:PSS) as the HTL and BCP as the ETL, achieving a PCE of 9% with a V_{OC} of 0.53 V, and a J_{SC} of 24.1 mA cm^{-2} [364]. Jiang *et al* also proposed p-i-n mixed 2D/3D $PEA_xFA_{1-x}SnI_{3-x}$ ($PEA = C_6H_5CH_2CH_2NH_3^+$) solar cells with indene-C_{60} bisadduct (ICBA) and PEDOT:PSS as the ETL and HTL, respectively [119]. They showed that the use of ICBA, which exhibits a lowest unoccupied molecular orbital (LUMO) closer to the vacuum level compared to

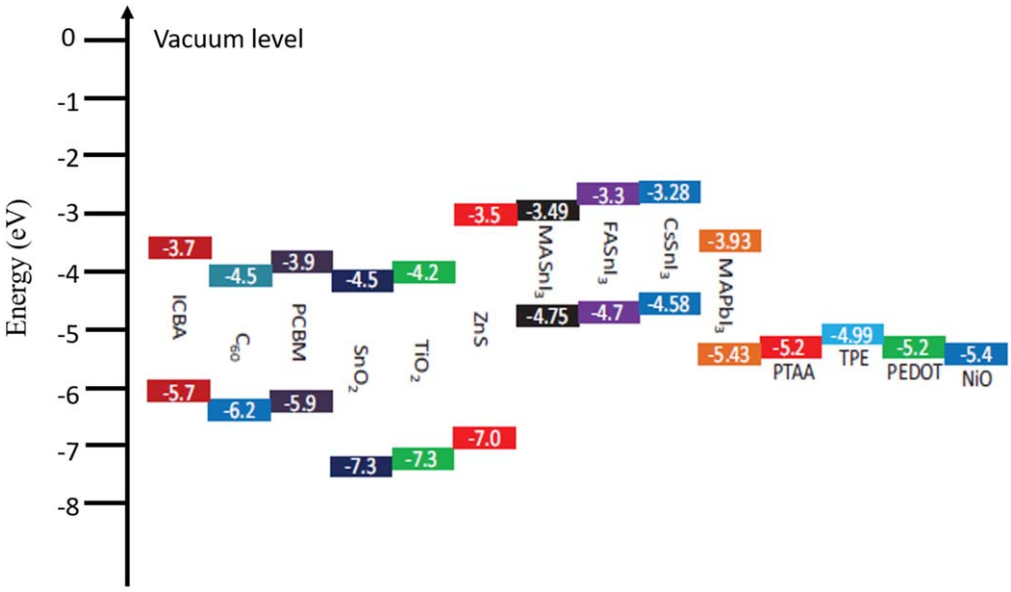

Figure 20. Energy diagram of Sn- and Pb-based perovskites along with some common ETLs and HTLs. Unit is in eV. The energy levels are estimated from Tauc plots and photoemission spectroscopy in air. [19] John Wiley & Sons. © 2018 WILEY-VCH Verlag GmbH & Co. KGaA, Weinheim.

PCBM, could effectively increase the V_{OC}. Introducing NH_4SCN as an additive to the perovskite can help to reduce defect densities as well. As a result, their champion device showed a record PCE of 12.4% and V_{OC} of 0.94 V along with a J_{SC} of 17.4 mA cm^{-2}. It should be noted that simpler devices without hole transport layers have also been reported. For instance, HTL-free p-i-n $CsSnI_3$ solar cells (with $SnCl_2$ added to the perovskite to improve film quality) demonstrated a PCE of 3.56%, along with a high fill factor of ~70% [121].

The efficiency for Sn-based perovskite solar cells is limited by nonradiative recombination (with carrier lifetimes <1 ns for most thin film samples) and unmatched band alignment with common transport layers [19]. Other than poor film morphology during processing, the high recombination rate of Sn-based perovskites is mainly due to the creation of Sn vacancies from self-doping (refer to section 3.1). Recently, it has been shown that the incorporation of additives such as enI_2 and PEAI [229, 364] or using high-impurity precursors might help to decrease the density of these background recombination centers. On the other hand, Sn-based perovskites have larger band mismatch to common ETLs and HTLs compared to $MAPbI_3$, as shown in figure 20. This mismatch may impede the carrier extraction and cause the recombination loss at the interface of the transport layers and the perovskite layer, which will reduce V_{OC} significantly. Searching for transport layers with suitable band-edges is therefore important as fabricating Sn-based perovskite solar cells.

Sn-based perovskite solar cells are unstable in air owing to the oxidation of Sn^{2+}, as discussed in section 3.1. Typically, neat Sn-based perovskite solar cells may completely lose their initial PCEs in air within a few hours [229, 365, 366]. In addition to processing under an oxygen-free or hydrazine-based atmosphere, many works have been attempted a wide range of strategies to improve the stability of Sn-based perovskites. For instance, the hollow structures incorporated with en [229] or using TMA as additives have been shown to enhance the air stability of $FASnI_3$ [362]. Incorporation of the nonpolar guanidinium cations (GA^+) with 1% ethylenediammonium diiodide ($EDAI_2$) as an additive can also enhance the moisture tolerance of $FASnI_3$ [367]. Devices based on this hybrid Sn-based perovskite showed almost no decrease in PCE after storage without encapsulation in air with 20% relative humidity for 170 h. Furthermore, an improvement in PCE was achieved when stored in a N_2-filled glovebox for 2000 h. Recently, solar cells composed of 2D Sn-based perovskites were found to exhibit improved ambient stability than their 3D counterparts. For example, it has been shown that the PCE of 2D layered $(BA)_2(MA)_3Sn_4I_{13}$ (BA: butylammonium) solar cells demonstrated less degradation than 3D $MASnI_3$ in air [366]. However, the PCEs for most Sn-based perovskite solar cells decrease significantly after a few days in air unless proper encapsulation is employed. By encapsulating devices with glass and epoxy or glue under inner gas atmosphere, the encapsulated cells could extend their device lifetimes up to a few months [368].

4.3. Ge-based perovskite

Ge-based perovskite PV devices have been fabricated in the mesoporous and p-i-n structures. Krishnamoorphy *et al* fabricated various mesoporous Ge-based perovskite solar cells by using spiro-OMeTAD as the HTL [128]. However, the PCEs of mesoporous $CsGeI_3$ and $MAGeI_3$ solar cells are limited by their low V_{OC} in the mV range, which is far below the band gaps.

Champion Ge-based perovskite solar cells were based on the p-i-n structure with PEDOT:PSS as HTL and $PC_{70}BM$ as ETL. Kopacic *et al* showed that the efficiency and stability of

p-i-n structured $MAGeI_3$ solar cells could be improved with the substitution of a few percent of bromine [126]. Consequently, the optimal device with $MAGeI_{2.7}Br_{0.3}$ demonstrated a record PCE of 0.68% along with an improved V_{OC} of 460 mV.

There are currently few reports of Ge-based perovskite PV devices mainly due to their limited stability, as discussed in section 3.2. Even $MAGeI_{2.7}Br_{0.3}$ solar cells with improved stability still lose two-thirds of their initial performance in air within a few hours after preparation [126]. It has also been claimed that the formation of 2D perovskites with the addition of bulky cations such as PEA^+ [365] could be a promising solution to address this issue.

Ge-based perovskite PV devices also suffer from low V_{OC}s, which limits PCEs, and which are arise in part due to the high density of defect states during the oxidation of Ge^{2+}. Improved synthesis methods would be needed to address this issue, but the poor solubility of some precursors in most polar organic solvents is also a challenge that needs to be overcome. Krishnamoorthy *et al* proposed that preparation methods without the addition of hypophosphorous acid as well as the strict control of synthesis environment and precursors may help improve the quality of fabricated Ge-based perovskite films [128].

4.4. Double perovskite

Most double perovskite solar cells investigated have used $Cs_2AgBiBr_6$, while most groups reported only ~1% PCE in PV devices based on this material. However, the first report of this material in photovoltaics by Greul *et al* led to higher PCEs of 2.43% and external quantum efficiencies (EQEs) reaching 60% [239]. This was achieved through careful optimization of the film quality. Recently, Yang *et al* introduced an N179 dye (di-tetrabutylammonium cis-bis(isothiocyanato) bis(2,2′-bipyridyl-4,4′ dicarboxylato) ruthenium (II)) interlayer between the active layer and spiro-OMeTAD HTL, which could improve hole transfer and enhance light absorption. As a result, the optimized mesoporous $Cs_2AgBiBr_6$ solar cell exhibited a record PCE of 2.84% with a V_{OC} of 1.06 V and a J_{SC} of 5.13 mA cm^{-2} [136]. On the other hand, Gao *et al* showed that p-i-n $Cs_2AgBiBr_6$ solar cells could also deliver a PCE of 2.23% with a V_{OC} of 1.01 V and a J_{SC} of 3.19 mA cm^{-2} after using IPA as the anti-solvent during film synthesis [131], which resulted in smooth and uniform films with micron-sized grains. In addition, $Cs_2AgBiBr_6$ solar cells have demonstrated improved stability in ambient air over Sn-, Ge- and Pb-based perovskites. The stability of $Cs_2AgBiBr_6$ solar cells have been tested by storing cells in the dark under ambient condition (temperature: 20 °C–30 °C, relative humidity: 40%–60% [236]), which is actually consistent with the dark storage study in ISOS protocols (ISOS-D-1). Eventually, the optimal $Cs_2AgBiBr_6$ solar cells showed no PCE degradation for at least 30 d.

As mentioned in section 3.3, the performance of double perovskite devices is still significantly limited by their intrinsic optoelectronic properties (large band gaps and poor carrier mobilities) and synthesis challenges (low solubility precursors).

4.5. $A_3B_2X_9$ materials

$MA_3Bi_2I_9$ and $Cs_3Bi_2I_9$ are the two $A_3B_2X_9$ materials that are most commonly investigated in reports of defect-ordered perovskite PVs. $MA_3Bi_2I_9$ devices are generally based on the mesoporous structures with spiro-OMeTAD as the HTL. Most PV devices, however, have demonstrated very low PCEs, which are believed to be related to the poor film morphology of $MA_3Bi_2I_9$, in addition to the high exciton binding energy and large effective masses. Many investigators have worked on improving the film morphology. Zhang *et al* fabricated $MA_3Bi_2I_9$ films via a two-step approach with the BiI_3 films evaporated under high vacuum and transformed into $MA_3Bi_2I_9$ films under a low vacuum MAI atmosphere [369]. Their $MA_3Bi_2I_9$ solar cells consist of the compact, pinhole-free, and large-grained films, demonstrating a PCE of 1.64% with a V_{oc} of 0.81 V and a J_{SC} of 2.95 mA cm^{-2}. Jain *et al* further optimized the $MA_3Bi_2I_9$ film quality via the vapor assisted solution process by exposing solution-processed BiI_3 films to MAI vapors, and replaced spiro-OMeTAD with poly(3-hexylthiophene-2,5-diyl) (P3HT) as the HTL [148]. A PCE of 3.17% with a V_{OC} of 1.01 V and a J_{SC} of 4.02 mA cm^{-2} was achieved in their champion solar cells.

Similarly, most $Cs_3Bi_2I_9$ PV devices were fabricated based on the mesoporous structure as well. The PCEs of these devices were also low due to their relatively low photocurrents. Ghosh *et al* showed that the photocurrents of $Cs_3Bi_2I_9$ solar cells could be enhanced when the precursor solution was prepared with excess BiI_3, which may passivate the deep-level defects of $Cs_3Bi_2I_9$ [370]. They investigated the influence of different structures (planar and p-i-n), along with the mesoporous solar cells with different HTLs, while none of the PCEs of these devices exceeded 1%. A PCE of 0.21% with a V_{OC} of 0.49 V and a J_{SC} of 0.67 mA cm^{-2} was achieved in their best device. A breakthrough was made by Bai *et al* [151]. They reported a dissolution-recrystallization method to fabricate high-quality $Cs_3Bi_2I_9$ films. In this method, the mixed DMF/CH_3OH solvent, which can thoroughly dissolve $Cs_3Bi_2I_9$ and evaporate, will be dropped onto the annealed as-deposited $Cs_3Bi_2I_9$ films, and the ultrathin $Cs_3Bi_2I_9$ nanoplates will recrystallize after the second annealing. Eventually, the devices with CuI as the HTL achieved a record PCE of 3.2% with a significantly improved J_{SC} of 5.78 mA cm^{-2}, which is ascribed to the smaller grains and voids within fabricated films.

Sb-based $A_3B_2X_9$ material solar cells also drew the attention of many researchers due to their higher dimensionality (2D) compared to Bi-based counterparts (0D), which could lead to improved mobilities. In particular, $Cs_3Sb_2I_9$ can be 0D or 2D depending on the synthesis method (refer to section 3.5). $Cs_3Sb_2I_9$ solar cells have been fabricated based on n-i-p or p-i-n structures. Umar *et al* deposited high-quality 2D $Cs_3Sb_2I_9$ films by using IPA as an antisolvent and introducing HCl additive into the precursor solutions, which can decrease the reaction time and suppress the formation of Sb–I–Sb clusters [157]. HTL-free planar $Cs_3Sb_2I_9$ solar cells with only TiO_2 as the ETL were realized with a PCE of 1.21%, V_{OC} of 0.61 V and a J_{SC} of 3.55 mA cm^{-2}. By contrast, 0D

$Cs_3Sb_2I_9$ devices with a similar structure only obtained a PCE of 0.43%. Sign *et al* fabricated *p-i-n* 2D $Cs_3Sb_2I_9$ solar cells with PEDOT:PSS as the HTL and [6,6]-Phenyl-C71-butyric acid methyl ester ($PC_{70}BM$) as the ETL [156], achieving a PCE of 1.49% with a V_{OC} of 0.72 V and a J_{SC} of 5.31 mA cm^{-2}. On the other hand, p-i-n 0D $Cs_3Sb_2I_9$ solar cells exhibited a larger V_{OC} (0.77 V) while much smaller J_{SC} (2.96 mA cm^{-2}) and PCE (0.89%), which is mainly ascribed to the larger band gaps of 0D $Cs_3Sb_2I_9$. Alternatively, Peng *et al* demonstrated mesoporous 0D $Cs_3Sb_2I_9$ solar cells with poly(N,N′-bis-4-butylphenyl-N,N′-isphenyl) benzidine (poly-TPD) as the HTL [250] could only achieve a low PCE of 0.24%. However, the incorporation of Cl was found to convert 0D $Cs_3Sb_2I_9$ into 2D $Cs_3Sb_2Cl_xI_{9-x}$, and mesoporous 2D $Cs_3Sb_2Cl_xI_{9-x}$ solar cells (with LZ-HTL-1-1 as the HTL) showed a significantly improved PCE of 2.15% with a V_{OC} of 0.6 V and a J_{SC} of 6.46 mA cm^{-2}. Additionally, some promising results have been obtained with $Rb_3Sb_2I_9$ solar cells. Weber *et al* deposited single crystallite $Rb_3Sb_2I_9$ thin films by using the antisolvent vapor diffusion crystallization method [165], where single crystals could grow as the antisolvent was evaporated and condensed onto the coated precursor solutions. A PCE of 1.37% and peak EQE of 26% was achieved in their champion mesoporous $Rb_3Sb_2I_9$ with spiro-OMeTAD as the HTL. They also found that the incorporation of Br led to a preferred orientation of $Rb_3Sb_2Br_{9-x}I_x$films parallel to the substrate, which would impede carrier transport. Recently, Li *et al* employed high temperature annealing under SbI_3 atmosphere to improve the morphology of $Rb_3Sb_2I_9$ films and increase the grain size [161]. Based on the planar structure with poly(N,N′-bis-4-butylphenyl-N,N′-bisphenyl)benzidine (poly-TPD) as the HTL, optimized $Rb_3Sb_2I_9$ solar cells from Li *et al*'s study demonstrated a comparable PCE (1.35%) but a much higher peak EQE (65.4%), which was attributed to the improved mobilities and reduced defects in the devices.

As discussed in section 3.5, most PV devices based on $A_3B_2X_9$ materials are stable in air. For instance, the stability of $Rb_3Sb_2I_9$ solar cells have been tested by storing cells in the dark under inert gas atmosphere, which is consistent with the suggested protocol ISOS-D-1I for PSCs [337]. As a result, the PCE of $Rb_3Sb_2I_9$ solar cells could retain 84% of their initial values after 150 d [165]. However, planar $Cs_3Bi_2I_9$ solar cells with CuI and spiro-OMeTAD as the HTL were found to maintain only 57% and 28% of their initial PCEs, respectively after storing in a constant temperature-humid chamber (temperature: 25 °C, relative humidity: 45%) for 38 d [151], which implies that the device stability may be influenced by the interactions between transport layers and active layers.

The factors limiting the performance of $A_3B_2X_9$ material-based devices are the wide band gaps, high exciton binding energies, poor film morphology, and the presence of deep defects. As discussed in section 3.5, wide band gaps and high exciton binding energies can lead to weak absorption and poor carrier extraction, respectively. Though some works have attempted to tune the band gaps by mixing different halides with $A_3B_2X_9$ materials at different proportions [144], there are not yet sufficiently promising results reported. In addition, high exciton binding energies are partly due to the lower dimensionality of $A_3B_2X_9$ materials, and synthesis routes which can convert 0D structure into 2D counterpart for some materials (e.g. $Cs_3Sb_2I_9$) may help to address this issue. Finally, many researchers have managed to resolve the latter two issues via various processing techniques. Shin *et al* also proposed a general method to fabricate compact thin films of most Bi-based $A_3B_2X_9$ precursors [371], which involves the use of solvent complexes to increase the solubility of Bi-based precursors and a subsequently rapid nucleation process via an antisolvent dripping. It should be noted that film orientation should be taken into account as well when developing synthesis routes since strong anisotropy can be seen in $A_3B_2X_9$ materials.

4.6. ABZ_2 materials

ABZ_2-based PV devices can be fabricated as n-i-p or p-i-n structures. Nanocrystals of ABZ_2 could also be mounted onto a mesoporous scaffold, giving a sensitized structure. At present, devices based on $CuSbS_2$, $CuSbSe_2$, and $AgBiS_2$ are investigated most. Although some early progress has been made in $NaBiS_2$ and $NaSbS_2$ quantum dot sensitized solar cells [166, 168, 170], investigations into both materials are still rare.

$CuSbS_2$ PV devices were largely fabricated based on the p-i-n and mesoporous structures. p-i-n $CuSbS_2$ solar cells typically used Mo as the HTL and ZnO as the ETL with a CdS buffer layer between $CuSbS_2$ and ZnO to form a type-II staggered heterojunction and promote carrier separation [277]. Septina *et al* prepared purified $CuSbS_2$ films with the precursors preheated before sulfurization, fabricating p-i-n $CuSbS_2$ solar cells achieving a PEC of 3.1% with a V_{OC} of 0.49 V and a J_{SC} of 14.73 mA cm^{-2} [178]. Banu *et al* demonstrated p-i-n $CuSbS_2$ solar cells prepared from hybrid inks [179]. The cells they made showed a record PCE of 3.22% with a V_{OC} of 0.47 V and a J_{SC} of 15.64 mA cm^{-2}. Mesoporous $CuSbS_2$ solar cells were found to exhibit comparable PV performance compared to that of p-i-n solar cells. Chio *et al* fabricated mesoporous $CuSbS_2$ solar cells with poly(2,6-(4,4-bis-(2-ethylhexyl)-4H-cyclopenta[2,1-b;3,4-b′] dithiophene)-alt-4,7(2,1,3-benzothiadiazole)) (PCPDTBT) as the HTL, achieving a PCE of 3.1% with a V_{OC} of 0.34 V and a J_{SC} of 21.5 mA cm^{-2} [372].

On the other hand, almost all the $CuSbSe_2$ solar cells were built in the p-i-n structure by using Mo or Mo/MoO_x and ZnO (with CdS buffer layers) as the HTL and ETL, respectively. Although there are fewer reports of $CuSbSe_2$ PV devices than $CuSbS_2$ devices, $CuSbSe_2$ PV devices have achieved higher performance. Yang *et al* optimized the morphology and crystalline orientation of hydrazine solution processed $CuSbSe_2$ film by tuning the annealing temperature [185]. However, $CuSb(Se,S)_2$ usually occur due to the reaction with competitive phases. As a result, the optimal $CuSb(Se_{0.96}S_{0.04})_2$ solar cells only showed a PCE of 2.7%. Welch *et al* controlled the evaporation flux ratio of Sb_2Se_3 and Cu_2Se to form pure phase $CuSbSe_2$ films, but found a trade-off between J_{SC} and V_{OC} exists in $CuSbSe_2$ solar cells [186]. It has been shown that as the Sb_2Se_3/Cu_2Se ratio

increased, the J_{SC} would be enhanced due to the extended depletion width, while the V_{OC} would be suppressed owing to the reduced hole concentration (and hence the reduced quasi Fermi level splitting). Consequently, the highest PCE of 4.7% along with a V_{OC} of 0.336 V and a J_{SC} of 26 mA cm^{-2} were achieved in their devices.

In addition to competitive impurity phases and the J_{SC}-V_{OC} trade-off for $CuSbSe_2$ solar cells, lower J_{SC} arising is a common challenge for $CuSbS_2$ and $CuSbSe_2$ solar cells. This could be attributed to the strong absorption losses of CdS buffer layer [283], which leads to a significant drop in the short wavelength range below 520 nm. Moreover, CdS layers are known to have some detrimental effects, such the introduction of deep hole defects [373]. Nevertheless, none of PV devices with CdS being replaced by other materials have shown promising performance to date.

Most $AgBiS_2$ solar cells were fabricated as the planar structure with ZnO as the ETL and P3HT or poly[[4,8-bis[(2-ethylhexyl)oxy]benzo[1,2-b:4,5-b′]dithiophene-2,6-diyl][3-fluoro-2-[(2-ethylhexyl)carbonyl]thieno[3,4-b]thiophenediyl]] (PTB7) as the HTL. Bernechea *et al* displayed $AgBiS_2$ nanocrystal solar cells achieving a PCE of 6.3% with a V_{OC} of 0.45 V and a J_{SC} of 22 mA cm^{-2} [264]. The cells in this work also demonstrated high stability in air with the PCE almost unchanged under ambient condition for up to four months. Recently, Burgues-Ceballos *et al* have shown that the $AgBiS_2$ nanocrystal sizes can be enlarged by using the double-step hot-injection technique [177], making thin films with higher carrier mobilities and lower defect densities. As a result, their champion $AgBiS_2$ nanocrystal solar cell exhibited a PCE of 6.4%, a V_{OC} of 0.46 V along with an improved J_{SC} of 22.68 mA cm^{-2}, which can be ascribed to better carrier extraction in this device.

Incomplete current collection is one of the main challenges for $AgBiS_2$ solar cells, which could be confirmed by the nonlinear dependence of J_{SC} of on light intensity [264]. Improvements in the ligands used or the surface passivation of the nanocrystals would be needed to suppress the trap recombination during carrier transport.

4.7. Binary halides

Apart from BiI_3, binary halides have not yet been investigated much into PV devices. Most BiI_3-based PV devices were fabricated based on the planar structure. Hamdeh *et al* used TiO_2 and V_2O_5 as the ETL and HTL [287], respectively, and found that the devices processed in air showed better performance than those in a glovebox, which is attributed to the facilitated hole transport due to the formation of BiOI layers. Moreover, solvent vapor annealing could also improve film quality and boost the PCE of PV devices. A PCE of 1.02% with a V_{OC} of 364 mV and a J_{SC} of 7 mA cm^{-2} were displayed in their work. Tiwari *et al* showed that using HTLs with higher ionization potential such as poly(9,9-di-noctyl-fluorenyl-2,7-diyl) (F8) can exhibit better match to the VBM of BiI_3, raising the V_{OC} of PV devices [196]. As a result, their champion planar BiI_3 solar cell demonstrated a slightly improved PCE of 1.21% along with a record V_{OC} of 0.607 V. Additionally, hole extraction also plays an important role in determining PCEs of BiI_3-based PV devices, which could be seen from the substantial influence of the HTL on device performance. Searching for HTLs with matched energy levels is thus crucial for BiI_3-based PV devices. Furthermore, the softness of the material makes it challenging to handle without scratching the film and causing pinholes to occur [374]. Finally, BiI_3 devices have exhibited improved stability over Sn-, Ge- and Pb-based perovskites. It has been verified that mesoporous BiI_3 solar cells stored in ambient air with a relative humidity of 50%, which is also consistent with the test requirement of the protocol ISOS-D-1, can retain above 90% of their initial PCEs for over 30 d [375]. In addition, these cells could also maintain ~70% of their initial PCEs and showed mineral change in their *J*–*V* curves after the heat stress (temperature: 100 ℃ in ambient air, similar to the environment requirement of the protocol ISOS-D-2 with a higher temperature) for 2 h and light-soaking test (by a solar simulator, consistent with the environment requirement of the protocol ISOS-L-1) for 20 min, respectively [375].

Recently, planar InI solar cells with CdS and P3HT as the ETL and HTL, respectively, were reported by Mitzi's group [107]. SnI_2 was used as an interface modification layer between the CdS and InI layer to control the preferred orientation of InI films. Eventually, a PCE of 0.39% with a V_{OC} of 450 mV and a J_{SC} of 2.14 mA cm^{-2} were demonstrated in the champion cell. Although Brandt *et al* have showed that InI predominantly forms shallow defects [18], Dunlap-Stohl *et al* indicated that the weak PL emission from InI-based PV devices suggests the presence of non-radiative recombination centers [107]. In addition, significant hysteresis was also observed in InI-based PV devices [107]. Improvements in the performance of InI devices will require further understanding of the composition and role of defects in this material, as well as control over the oxidation of In^+ to In^{3+}.

4.8. V–VI–VII materials

V–VI–VII materials have been applied as photocatalysts (refer to section 5.2), but have gained increasing attention for solar absorber applications more recently. Owing to their original application in photocatalysts, early BiOI solar cells were fabricated as liquid-state sensitized architectures with iodide redox couple as electrolytes. However, most devices showed very low efficiencies. Zhang *et al* deposited BiOI flakes onto mesoporous TiO_2 as the working electrodes, but their devices only reached 0.38% efficiently [376]. Sfaelou *et al* replaced mesoporous TiO_2 with a compact layer of TiO_2 and fabricated BiOI solar cells with a PCE over 1% and a V_{OC} of 0.61 V [297]. Recently, Hoye *et al* demonstrated solid-state BiOI solar cells with a p-i-n structured comprising of NiO_x and ZnO as the HTL and ETL, respectively [201]. A record PCE of 1.8% with a V_{OC} of 0.75 V and a J_{SC} of 7 mA cm^{-2} was achieved in the champion device. They showed that the band bending caused by the energy level mismatch (figure 21) between BiOI and the HTL could introduce unwanted energy barriers to hole collection. From this, they claimed that future

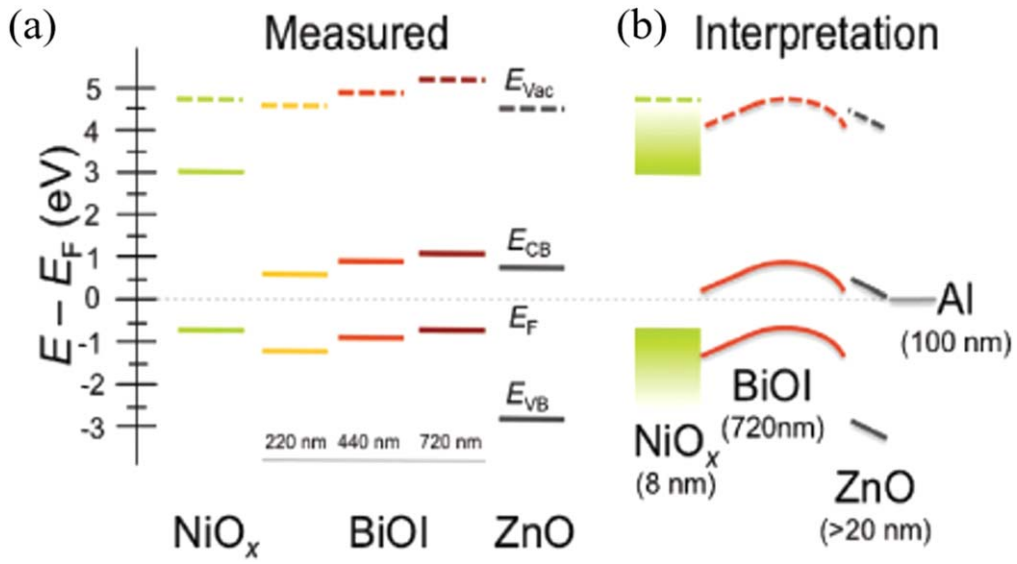

Figure 21. (a) The measured energy alignment of device stack and (b) schematic energy band diagrams for inverted BiOI solar cells. Reproduced from [201]. CC BY 4.0.

progress on performance could be made by finding HTLs with deeper work functions [201]. Furthermore, BiOI has a layered structure with anisotropic carrier transport. The CVD BiOI grown on solution-processed NiO_x by Hoye *et al* had an {012} preferred orientation, which allowed the top and bottom electrodes to be connected by the high-mobility planes. This enabled effective charge extraction, with a peak EQE up to 80% at 450 nm wavelength [201]. At the same time, the films had an open structure, which limited the shunt resistance. It was later shown the preferred orientation of the BiOI platelets grown by CVD could be controlled through the temperature of the BiI_3 precursor and the temperature of the substrate [298], as discussed in section 3.8. Growing *c*-axis oriented BiOI platelets resulted in compact film morphology, which improved the V_{OC} from 0.7 V (*a*/*b*-axis oriented) to 0.9 V (*c*-axis oriented).

Owing to the *n*-type characteristic of BiSI, Hahn *et al* combined BiSI films with *p*-type CuSCN to make single junction solar cells [377]. They tested the PV performance of BiSI/CuSCN solar cells immersed in the electrolyte containing iodide compounds and achieved a 0.25% PCE. However, the poor charge separation and transport within BiSI films led to an abnormal *I*–*V* curve in their devices, where dark currents increased slowly under reverse bias. In addition, solid-state BiSI/CuSCN solar cells were also fabricated, but a small PCE of only 0.012% was reached, which was mainly ascribed to scattering losses from CuSCN layer as well as non-radiative recombination within the BiSI layer. It is worth mentioning that though they attempted to introduce Se-dope BiSI films to reduce the band gaps, this resulted in a reduction in the performance, possibly due to increased defect densities. Recently, Tiwari *et al* fabricated planar BiSI solar cells with SnO_2 and F8 serving as the ETL and HTL, respectively [202]. A PCE of 1.32% with a V_{OC} of 0.445 V and a J_{SC} of 8.44 mA cm^{-2} was obtained from their optimized device. It was claimed that one key challenge is the presence of other Bi–S–I phases in the films [306]. Moreover, BiSI devices also suffer from short carrier lifetime due to the presence of deep defects [378] and poor carrier transport, which arises from the strong anisotropy of BiSI films [202].

Nie *et al* used CBD to fabricate mesoporous SbSI solar cells which demonstrated a PCE up to 3.05% along with a V_{OC} of 0.58 V and a J_{SC} of 9.11 mA cm^{-2} [309]. Their great success was attributed to the use of poly[2,6-(4,4-bis-(2-ethylhexyl)-4H-cyclopenta[2,1-b;3,4-b′]dithiophene)-alt-4,7 (2,1,3-benzothiadiazole)] (PCPBTBT) as the HTL, which can not only transport holes effectively but also harvest light not absorbed by SbSI. Mesoporous SbSI solar cells in this work retained over 93% of their initial PCEs after 15 d of storage under ambient condition in the dark. Similar stability could be maintained even under highly humid condition (humidity: 60%). Choi *et al* demonstrated planar SbSI solar cells fabricated by a simple solution processing method [206], which may help resolve the issues of CBD-synthesized SbSI films such as the formation of impurity phases and an uncontrollable Sb/S ratio. However, the best planar SbSI solar cell only showed a PCE of 0.93% with a V_{OC} of 0.548 V and a J_{SC} of 5.45 mA cm^{-2}. Recently, Nie *et al* proposed a vapor processing method, where more uniform SbSI films could form when CBD-processed Sb_2S_3 were annealed under vaporized SbI_3 atmosphere [205]. As a result, a record PCE of 3.62% along with a V_{OC} of 0.6 V and a J_{SC} of 9.62 mA cm^{-2} was achieved in their mesoporous SbSI solar cells (with PCPDTBT as the HTL). Compared to the CBD-processed solar cells, the vapor processed solar cells exhibited better crystallinity (stronger XRD peaks), lower series resistance, and better stability (vapor-processed cells could maintain 91% of their initial PCEs while CBS-processed cells would lose over 70% of theirs after 3 h under illumination) which is due to the compactness of the fabricated films. In this study, they

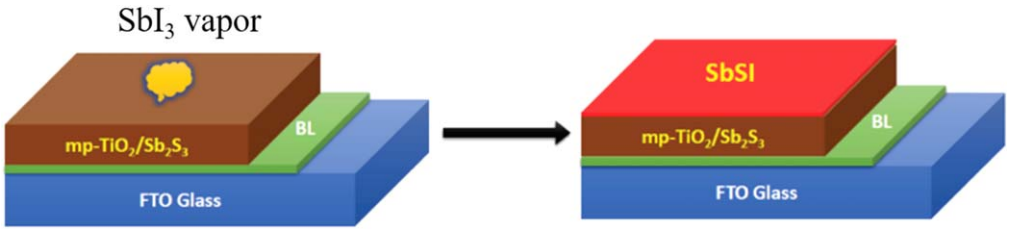

Figure 22. Configuration of SbSI-interlayered Sb_2S_3 solar cell (the HTL is not shown). [205] John Wiley & Sons. © 2018 WILEY-VCH Verlag GmbH & Co. KGaA, Weinheim.

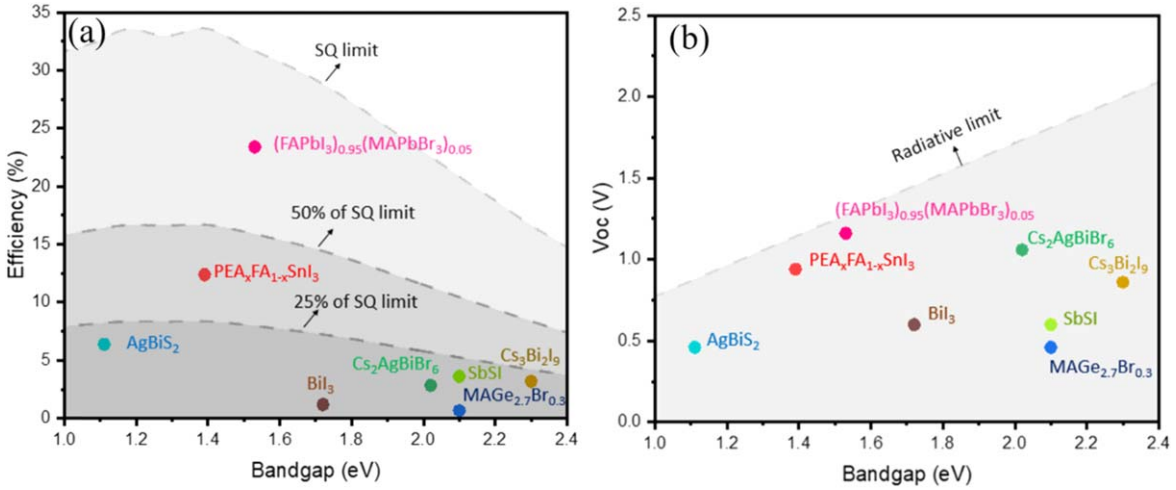

Figure 23. (a) The highest efficiencies and (b) the corresponding V_{OC} from various PIM-based PV devices reported in the literature to date. The highest values reported in Pb-based perovskite ($(FAPbI_3)_{0.95}$ $(MAPbBr_3)_{0.05}$) counterpart are also depicted.

also used halide treatment on Sb_2S_3 films to passivate surface defects and form thin SbSI layers above (figure 22). It has been claimed that these SbSI thin films can exert an external driving force to promote the carrier transport. The optimized mesoporous SbSI-interlayered Sb_2S_3 solar cell demonstrated a high PCE of 6.08% with a V_{OC} of 0.62 V and a J_{SC} of 14.92 mA cm^{-2}.

4.9. Overview of perovskite-inspired materials in photovoltaics

Figure 23 illustrates the highest PCEs and corresponding V_{OC} reported in various PIM-based PV devices discussed in this Review. For comparison, the highest values for Pb-based PSC ($(FAPbI_3)_{0.95}(MAPbBr_3)_{0.05}$) reported in literature (not the record value) is also plotted [342]. These are compared to the SQ limit for different band gaps, along with the radiative limit in the V_{OC}. It can be seen from figure 23(a) that except for Sn-based perovskites, all the other PIMs exhibited efficiencies below 25% of SQ limit. Furthermore, the V_{OC} of the PIM devices are well below their radiative limits (figure 23(b)). This is due to a combination of non-radiative recombination (due to traps or possibly self-trapped excitons in some cases), high Urbach energies, or shunting due to a sub-optimal morphology. There is therefore great room for improvements in PIM-based PV devices through the identification of new classes of materials that could tolerate defects and engineering the quality of the thin films grown.

Stability is always an important consideration for PV devices, and several devices based on PIMs such as double perovskites and V–VI–VII materials have shown improved stability over Pb-based perovskites. Aside from the intrinsic stability of PIMs, it has been shown that the adoption of transport layers in these devices can significantly influence the stability of the device itself. Therefore, many researches are now aiming to improve PIM device stability by introducing specific additives or through careful choice of the transport layers. We are thus looking forward to seeing more investigations on the PIM device stability by following specific protocols soon.

5. Broader applications of perovskite-inspired materials

There is a strong overlap between the required properties of solar absorbers with the ideal properties of materials in wide range of other types of electronics. For example, strong absorption of visible light, long transport lengths and low dark currents are also needed in radiation detectors, photocatalysts and memristors. This section explores the opportunities in applying lead-free PIMs beyond PVs and the new insights into the materials that could be gained in doing so.

5.1. Light-emitting applications

Luminescence is one of the critical properties that influences the performance of materials in photovoltaics through the open-circuit voltage [49]. It follows that efficient photovoltaics with a direct allowed band gap are promising candidates for light-emission applications. This has been particularly well demonstrated in III–V materials [379], and more recently with lead-halide perovskites [380, 381]. There are two common applications of emitters: (1) phosphors, in which the active layer is optically excited and spontaneously emits; and (2) light-emitting diodes (LEDs), in which electrons and holes are injected into the active layer, where they radiatively recombine to give electroluminescence (EL). For both applications, one of the most important properties of the emitter is the photoluminescence quantum efficiency (PLQE), which quantifies the percentage of recombination events that are radiative (refer to [381] for more details of the other properties influencing the efficiency of LEDs). LHPs have now achieved PLQEs approaching 100% across a variety of emission wavelengths [382–384]. Green-, red- and near-infrared-emitting perovskite LEDs have now also achieved external quantum efficiencies (EQEs) >20% [380, 384, 385]. Critically, pure-halide perovskites have demonstrated low Urbach energies <30 meV, and the FWHM of the PL and EL peaks are <30 nm [49, 386]. This is narrower than achievable in typical organic and inorganic emitters, and the high color saturation, coupled with the ability to tune the emission over the entire color gamut, makes both perovskite phosphors and LEDs highly suited for ultra-high definition displays [387, 388]. But there is a strong motivation to find lead-free alternatives for display and lighting applications, owing to regulations limiting the lead content in electrical products (e.g. to a maximum of 0.1 wt% by the European Restriction of Hazardous Substances Directive [389]).

Lead-free perovskite-inspired materials, however, have not been close in matching the performance and color-purity of LHPs [381, 390–393]. One of the main reasons is the low PLQEs of most lead-free materials, many of which have indirect band gaps (refer to section 3). But an important exception to the low luminescence in perovskite-inspired materials are $A_3B_2X_9$ nanocrystals. These include $Cs_3Sb_2Br_9$ nanocrystals (46%–51.2% PLQE at 410 nm wavelength [394, 395]) and $Cs_3Bi_2Br_9$ nanocrystals (19.4% PLQE at 410 nm wavelength [396]). The latter has been used as blue-phosphors, optically-excited with a UV-emitting GaN LED. These phosphors were combined with a broad-emitting $Y_3Al_5O_2$ (YAG) phosphor to achieve white-light emission, with Commission Internationale de l'éclairage (CIE) coordinates of (0.29, 0.30) (close to the (0.33, 0.33) coordinates for pure white) and a cool color temperature of 8477 K [396]. An important advantage of $Cs_3Bi_2Br_9$ is that it forms a passivating shell of BiOBr, which improves its stability against moisture and acid. As a result, $Cs_3Bi_2Br_9$ nanocrystals could be mixed with tetraethyl orthosilicate and react with HBr and water to form a nanocrystal-silica composite. This composite encapsulated the nanocrystals, resulting in improved stability under UV lighting (retaining 72% of the PL after 16 continuous UV illumination), and under heat stress (retaining 75% of the PL after 16 h continuous heating at 60 °C [396]). Similar results were achieved with the vacancy-ordered perovskite Cs_2SnCl_6. This perovskite is advantageous over regular tin-based perovskites because the tin cation is already in the more stable +4 oxidation state. By doping with bismuth, a PLQE of 78.9% could be achieved, with a blue emission wavelength of 455 nm. Cs_2SnCl_6:Bi was combined with yellow phosphors ($Ba_2Sr_2SiO_4$:Eu^{2+} and $GaAlSiN_3$:Eu^{2+}) and excited with a UV GaN LED, giving white emission with CIE coordinates of (0.36, 0.37) and a color temperature of 4486 K [397].

Lead-free double perovskites have also been demonstrated as white-light-emitting phosphors. The materials investigated have been $Cs_2A(I)B(III)Cl_6$, in which A(I) is Ag^+ or Na^+ (or a mixture of both), and A(III) is In^{3+} or Bi^{3+} or a mixture of both. White-light emission from these materials stems from broad luminescence below the optical band gap. $Cs_2AgBiCl_6$ has a wide indirect band gap [130], whereas $Cs_2NaInCl_6$ has a direct, parity-forbidden band gap [240], across which absorption is forbidden but PL could still occur. Alloying In into $Cs_2AgBiCl_6$ resulted in a broad orange luminescence peak below the optical band gap of $Cs_2AgBiCl_6$ appearing. This was attributed to the formation of a lower parity-forbidden band gap after alloying with In, from which luminescence occurred with a PLQE up to 36.6% with 90% In addition [398]. Sub-band gap emission in $Cs_2NaInCl_6$ was attributed to self-trapped excitons. Undoped $Cs_2NaInCl_6$ has no luminescence, which was believed to be due to the self-trapped excitons being dark. Alloying with Ag^+ improved the PLQE to 31.1% [399]. Alloying $Cs_2(Ag_{0.6}Na_{0.4})InCl_6$ with 0.04% Bi further increased the PLQE to 86 ± 5%, with broad emission centered at 570 nm wavelength [124]. On the other hand, $Cs_2NaInCl_6$ alloyed with Bi^{3+} remained dark, with only blue PL due to free excitons. But broad yellow emission was achieved through alloying with Mn^{2+}, with a PLQE of 44.6% being achieved, and this was attributed to the dark self-trapped exciton transferred to an excited state of Mn^{2+} [400]. $Cs_2(Ag_{0.6}Na_{0.4})InCl_6$:$Bi^{3+}$ was used as white-light phosphors, owing to its high white-light PLQE. With excitation from a GaN LED, emission with CIE coordinates of (0.396, 0.448) was achieved with a color temperature of 4054 K. Critically, the double perovskite was air stable, and even more so when encapsulated with silica. As a result, the emission was stable after 1000 h of illumination in air [124].

Currently, there is only a handful of reports of EL from PIMs, and most are on Sn-based perovskites. Lai *et al* reported near-infrared LEDs from $MASnI_3$, which emitted at 945 nm wavelength, but with EQEs only reaching 0.72% [401]. An important limitation was the low PLQE of 5.3% [401]. Rand *et al* subsequently improved the EQE to 5.0% (at 917 nm EL wavelength) by alloying Pb with Sn and introducing a long-chain organoammonium iodide ligand to the precursor solution. The inclusion of the ligand resulted in smaller grains with passivated surfaces [402]. Ruddlesden–Popper tin-based perovskites have also been investigated, but an early investigation into 2D phenethylammonium tin iodide resulted in inefficient red-emitting devices (0.15 cd m^{-2}

luminance and 0.03 cd A^{-1} current efficiency [403]). Subsequently, Rogach *et al* investigated tin-based Ruddlesden–Popper perovskites with bromide as the halide, and oleylammonium as the A-site cation. They were able to directly inject into the self-trapped exciton, resulting in broad orange sub-band gap EL (centered at 620 nm), with 0.1% EQE and 350 cd m^{-2} luminance [404]. Notably, a PLQE of 88% was achieved in colloidal suspensions, and 68% in thin films [404]. Beyond these tin-based perovskites, there has recently been a demonstration of Sb-based LEDs. Shan *et al* achieved violet EL from $Cs_3Sb_2Br_9$ (408 nm wavelength) with an EQE of 0.2%. The PLQE of the $Cs_3Sb_2Br_9$ quantum dots was 51.2%, and the quantum dots were stable against heat, UV illumination and moisture. In particular, the LEDs retained 90% of their initial EL intensity after 6 h of operation at 7 V ($\sim$70 mA cm^{-2} current density [394]). This is more stable than their Sn- and Pb-based perovskite counterparts. But the FWHMs of all tin- and antimony-based emitters discussed here are significantly wider than their lead-based counterparts, typically 50–100 nm [394, 401–403]. This makes them less competitive for display applications, compared to quantum dot, organic and inorganic LEDs already commercially available [387].

5.2. Photocatalysis

Leaves absorb sunlight to convert CO_2 and water to sugar and oxygen through photosynthesis. Similarly, semiconductors can absorb sunlight to enable the production of fuels, precursors for value-added products, or the degradation of organic contaminants through photocatalysis [405, 406]. The production of H_2 from water was first achieved by Fujishima *et al* in 1969, in which TiO_2 was used to absorb UV light. Holes generated in TiO_2 oxidized water to O_2 gas, while the electrodes transferred to the Pt counter electrode reduced H^+ to H_2 [407, 408]. This spurred several decades of research into semiconductor-based photocatalysis, and was motivated both by the promise of the clean solar-to-chemical energy conversion, as well as the limitations of TiO_2 in only being able to absorb a small part of the solar spectrum due to its wide band gap [405, 406, 409]. The materials and devices structures for photocatalysis, as well as the operating principles, are reviewed in [405, 406, 409, 410]. The requirements for the semiconductor are: (1) good light absorption, (2) high chemical stability in the presence of the electrolyte, (3) suitable band-edge positions for enabling the redox reactions required, (4) efficient charge transport, and (5) to be low-cost. Requirements 1, 4 and 5 overlap with the requirements for photovoltaic materials. Lead-halide perovskites have therefore been considered for photocatalysis, owing to their high absorption coefficients, strong overlap in their absorption with the solar spectrum, and long diffusion lengths, coupled with the ability to achieve high-quality films when processed at low temperature. But lead-halide perovskites are limited by their low chemical stability [406]. This necessitates tailoring of the solution to minimize degradation to the perovskite (e.g. using a saturated halo acid solution for water splitting), or encapsulating the perovskite to isolate them from the polar solvent [406, 411–414]. But ensuring the long-term stability of the photocathode or photoanode, as well as avoiding potential lead contamination of the solution motivate the investigation of lead-free and more stable alternatives.

In photocatalytic applications, the wider band gap of most perovskite-inspired materials is advantageous. Murphy *et al* found that the optimal band gap for solar-driven water splitting is 2.03 eV, which would enable a theoretical maximum solar-to-hydrogen conversion efficiency of 16.8% [415]. This is because the quasi-Fermi levels of the semiconductor determine the oxidation/reduction potential of the photoelectrochemical cell. Therefore, in the case of water splitting, the band gap needs to at least be equal to the difference in redox potentials for H^+/H_2 (hydrogen reduction) and O_2/H_2O (water oxidation). This has a value of 1.23 eV, but the semiconductor band gap needs to be larger in order to account for thermodynamic losses (0.3–0.4 eV) and overpotentials for fast reactions (0.4–0.6 eV). A band gap of $>$1.9 eV therefore should be used [409], indicating that many of the double perovskites, $A_3B_2X_9$ compounds and V–VI–VII compounds are suitable, particularly given their improved environmental stability compared to lead-halide perovskites (refer to section 3). The electronic band positions of these perovskite-inspired materials compared to the redox potentials for water splitting, as well as for CO_2 reduction [406] are shown in figure 24. It is noted that the redox potentials and band positions are given on a relative hydrogen electrode (RHE) scale. H^+/H_2 under standard conditions is typically taken as a reference point (standard hydrogen electrode), which occurs at pH 0 and has a value of 4.44 ± 0.02 eV relative to vacuum level according to IUPAC [409]. But according to the Nernst equation, the redox potential for H^+/H_2, as well as O_2/H_2O, CO_2/CO and CO_2/CH_4 all vary with -0.059 pH [V] [406]. The potential across the Helmholtz double layer on the semiconductor surface also changes with -0.059 pH [V]. The RHE scale is therefore used, in which all potentials are given relative to H^+/H_2 at a given pH [409].

Many recent works on lead-free perovskite-inspired materials for photocatalytic applications have focused on double perovskites, vacancy-ordered perovskites and $A_3B_2X_9$ materials. These materials have been demonstrated to be more phase-stable than methylammonium lead iodide in ambient air [145, 234, 237, 420]. Groups have also demonstrated $Cs_2AgBiBr_6$ to remain the same phase after illumination with 70 mW cm^{-2} white light for 500 h [234], while $Rb_3Bi_2I_9$, $Cs_3Bi_2I_9$ and $(CH_3NH_3)_3Bi_2I_9$ was found to maintain the same phase after 12 h of illumination with a UV lamp (80.4 μW cm^{-2} [416]). Despite these promising stability results, efforts have focused on the application of these perovskite-inspired materials as photocatalysts under benign environments (e.g. halo acid solutions or gaseous precursors), rather than in photoelectrolytic devices in more aggressive aqueous environments. Nevertheless, these works have found the photocatalysts to be stable under operation. Many works have focused on CO_2 reduction to form CO or CH_4 (or a mixture of both), and most materials have suitable electron affinities to induce the reduction of CO_2 (figure 24). Zhou

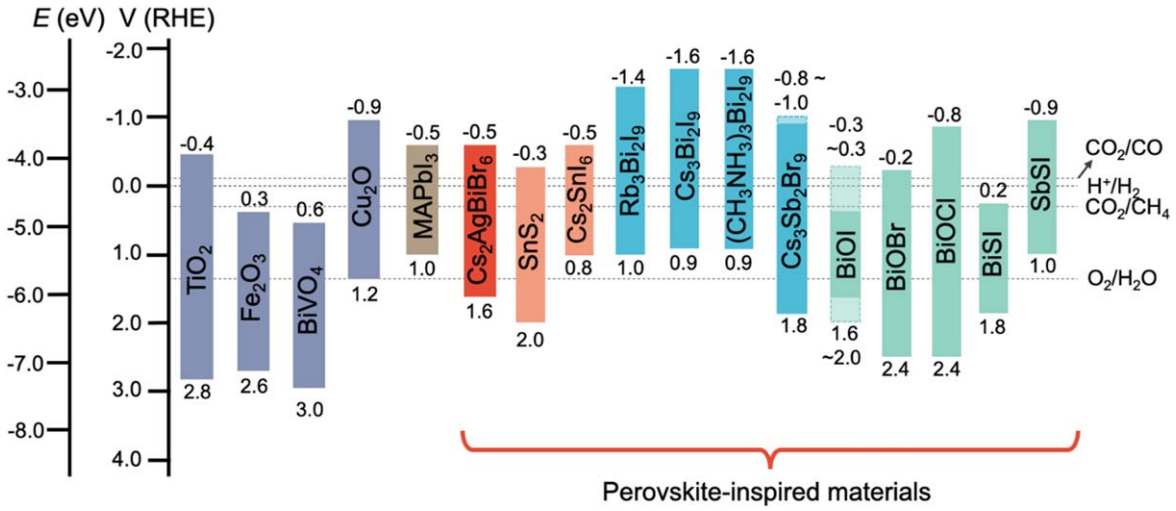

Figure 24. Band-edge positions of perovskite-inspired materials, which are compared to methylammonium lead iodide ($MAPbI_3$) and traditional photocatalytic materials. The band positions are shown on a relative hydrogen electrode (RHE) potential scale (energy scale shown as a comparison). The RHE redox potentials of common half-reactions are given [406, 409]. The band positions are obtained from [133, 201, 237, 296, 394, 406, 409, 416–420].

et al synthesized $Cs_2AgBiBr_6$ double perovskite nanocrystals through hot-injection [234]. However, the yield of CO and CH_4 were 5.5 μmol g^{-1} and 0.65 μmol g^{-1} respectively. This was improved by washing the nanocrystals in ethanol to remove the oleic acid and oleylamine ligands prior to the application of the nanocrystals as photocatalysts, which resulted in the yields improving to 14.1 μmol g^{-1} and 9.6 μmol g^{-1} for CO and CH_4 respectively. However, the external quantum efficiency was only 0.028% at 398 nm wavelength. Nevertheless, the washed double perovskite nanocrystals were found to not change in phase or surface composition or agglomerate after 6 h operation, implying that the nanocrystals were stable in the ethyl acetate solution the CO_2 was dissolved in [234]. Wang *et al* obtained comparable product yields using SnS_2 nanosheets decorated with Cs_2SnI_6. This was achieved by reacting the SnS_2 nanosheets with CsI dissolved in ethanol. The improvement in photocatalytic activity by forming Cs_2SnI_6 was attributed to the smaller band gap of the vacancy-ordered perovskite (1.3 eV [420]), which led to an increased population of photogenerated carriers [418]. Higher product yields were obtained by Bhosale *et al* using $A_3B_2I_9$ photocatalysts, especially $Cs_3Bi_2I_9$, which was found to have high photocatalytic activity and gave yields of 78 μmol g^{-1} and 15 μmol g^{-1} for CO and CH_4 respectively after 10 h [416]. The $Cs_3Bi_2I_9$ was synthesized as nanocrystals with oleic acid and oleylamine ligands and dispersed in trichloromethane after purification. The trichloromethane had a mixture of CO_2 gas and H_2O vapor introduced to it, and the nanocrystals were illuminated with a UV lamp [416]. Yet higher product yield was achieved using $Cs_3Sb_2Br_9$ nanocrystals, which reached 516 [417] μmol g^{-1} for CO after 5 h, with illumination under 1 sun radiation. By contrast, $CsPbBr_3$ nanocrystals produced only 53.8 μmol g^{-1} CO after 5 h under the same conditions. The $Cs_3Sb_2Br_9$ nanocrystals were synthesized by hot-injection, and were exposed to CO_2 gas dissolved in octadecene. The same nanocrystals were used three times, and it was found that with each subsequent usage, there was a decrease in the product yield. But after the third usage, the yield was approximately 30% of that of the first usage. Despite this reduction in activity, the yield remained higher than the yield of fresh $CsPbBr_3$ nanocrystals [417].

$Cs_2AgBiBr_6$ and $(CH_3NH_3)_3Bi_2I_9$ have also been investigated for the photocatalytic reduction of H^+ to H_2 [421, 422]. H_2 is an important clean fuel that combusts to only produce H_2O, is used for hydrogen fuel cells, and is a convenient option for storing excess solar energy to compensate for the intermittent nature of terrestrial solar radiation [405, 423]. Wang *et al* synthesized $Cs_2AgBiBr_6$ powder, and a mixture of HBr and H_3PO_2 was used as the H^+ source. The $Cs_2AgBiBr_6$ photocatalyst was illuminated with white light (300 W), and H_2 was generated with a rate of 0.6 μmol g^{-1} h^{-1}, averaged over 10 h. The photocatalytic activity was improved by 80 times to 48.9 μmol g^{-1} h^{-1} by adding reduced graphene oxide (rGO) to the double perovskite. Moreover, it was found that the photocatalytic activity of the composite remained stable after 12 cycles (120 h total). It is believed that the improved catalytic activity was due to (1) photogenerated electrons from the double perovskite being injected to the rGO, which contains active sites for H^+ reduction, and (2) a reduction in the recombination rate because of the separation of the photogenerated electrons and holes at the perovskite/rGO junction [421]. A higher H_2 production rate of 169.2 μmol g^{-1} h^{-1} was reported by Guo *et al* who used $(CH_3NH_3)_3Bi_2I_9$ powder coated with Pt. The electrolyte was HI solution, and it was found that $(CH_3NH_3)_3Bi_2I_9$ remained phase-stable in this solution. While the energy of the photogenerated holes was insufficient to oxidize water, they were believed to oxidize I^- to I_3^-. H_3PO_2 was added to the solution to reduce I_3^- to prevent I_3^- from accumulating and blocking light absorption in the $(CH_3NH_3)_3Bi_2I_9$/Pt photocatalyst. The stability was tested through 7 repeat cycles (each 10 h long), with only a

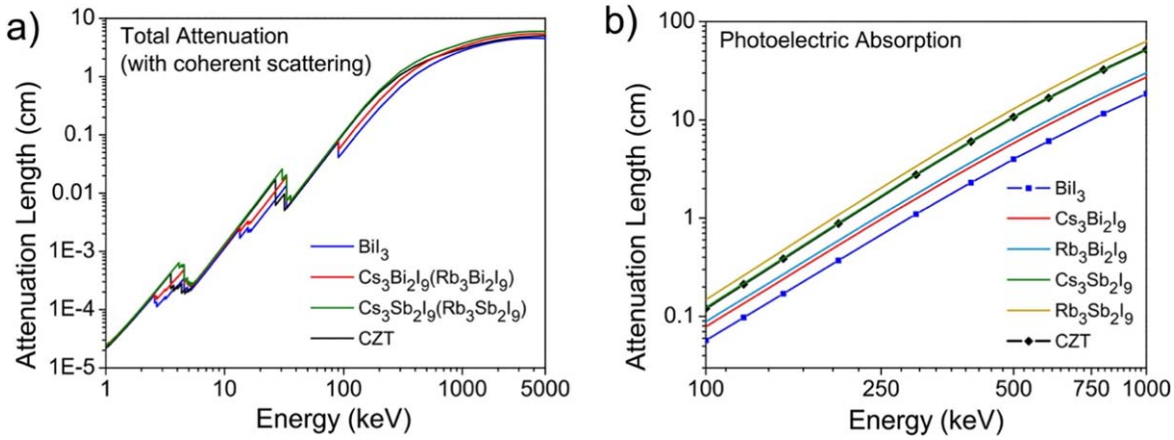

Figure 25. Attenuation length of perovskite-inspired materials compared to $Cd_xZn_{1-x}Te$ (CZT) under (a) total attenuation and (b) photoelectric absorption. Reprinted with permission from [429]. Copyright (2018) American Chemical Society.

small decrease in the catalytic activity [422]. Finally, $Cs_2AgBiBr_6$ powders have also been used as a photocatalyst for the degradation of ionic dyes in ethanol solution by forming oxygen radicals from O_2. The catalytic activity was again enhanced by coating with Pt. The double perovskite/Pt composites were observed to maintain their photocatalytic activity and phase after five cycles, which each had a duration of 1 h [424].

V–VI–VII materials have been investigated as both photocatalysts and photoelectrodes before the work on lead-halide perovskite photocatalysts began. These V–VI–VII materials are appealing due to their strong absorption of visible light. Two examples are BiOI and BiSI, which have band gaps of 1.6–1.9 eV [201, 425] (figure 25), and have been investigated as photocatalysts for degrading organic contaminants in water, such as methyl orange and crystal violet [425, 426]. BiOI itself has been found to have low photocatalytic activity due to its short charge-carrier lifetimes [426]. The photocatalytic activity has been improved through heterostructures, such as $BiOI/MoS_2$, $BiOI/WO_3$, BiOI/AgI, BiOI/Ag, BiOI/Ag/AgI, $BiOI/Bi_2WO_6$, $BiOI/Ag_3PO_4$, $BiOI/Bi_2MoO_6$, $BiOI/ZnSn(OH)_6$, BiOI/BiOBr [426]. Similarly, the photocatalytic activity of BiSI was improved by forming a composite with MoS_2 [425]. MoS_2 forms a type II heterojunction with both BiOI and BiSI, and this is thought to improve the separation of photogenerated electrons and holes, which can then take part in the photodegradation of the organic contaminants [426]. High photocatalytic activity was achieved from SbSI without needing to form a heterostructure. Tamilselvan *et al* demonstrated that micron-sized urchin-shaped SbSI degraded 97% of methyl orange [427], which is comparable to $BiOI/MoS_2$ nanocomposites and higher than BiOI alone [426]. Investigations found that SbSI induced the degradation of methyl orange by forming oxygen radicals through the oxidation of singlet oxygen with photogenerated holes [427]. Wang *et al* achieved a slightly higher degradation rate of methyl orange in aqueous solution (99% within 1 min when illuminated with a 300 W xenon lamp) through the use of SbSI nanocrystals at room temperature or at 65 °C [428]. However, they attributed the degradation of methyl orange to the formation of singlet oxygen rather than oxygen radicals [428]. For all materials ($BiOI/MoS_2$, $BiSI/MoS_2$, SbSI), it was found that the photocatalysts maintained their activity after several cycles [426].

Defects in bismuth oxyhalides have been found to enhance photocatalytic activity. For example, it was found that oxygen vacancies in BiOBr and BiOCl led to an increase in the product yield for the reduction of CO_2 to CO or CH_4 [430, 431]. It is believed that these oxygen vacancies act as sites for CO_2 adsorption, where they are activated to radical ions that can be reduced with photogenerated electrons. It is also proposed that the oxygen vacancies can trap electrons to prolong their separation from photogenerated holes [430]. These oxygen vacancies were induced in BiOBr by modifying the solvothermal synthesis, in which ethylene glycol was used as the solvent instead of water (which gave stoichiometric BiOBr [430]). For BiOCl, Zhang *et al* induced oxygen vacancies by illuminating for 5 h with a Xe lamp. But despite the improvements in photocatalytic activity, the product yield of CH_4 in BiOBr and BiOCl remained lower than $Cs_3Bi_2I_9$ [416, 430, 431]. Nevertheless, the materials were found to maintain their activity after several cycles, and, in the case of BiOCl, it was found that the oxygen vacancies could be regenerated through illumination [430, 431].

Bismuth oxyhalides have also been investigated in photoelectrochemical cells. BiOI was used in photoelectrochemical cells with an I_3^-/I^- redox couple (0.53 V reduction potential relative to the standard hydrogen electrode) in an acetonitrile-based solution. Platelets of BiOI were grown by successive ionic layer adsorption and reaction (SILAR) and spray pyrolysis [297, 432]. Such cells can be used as photovoltaic devices, but the performance was low, with PCEs of 1% or below, and EQEs reaching only 60% [297, 432]. Possibly a limiting factor was a non-compact structure of the BiOI platelets, or a non-optimal arrangement. Subsequent work on growing BiOI by chemical vapor deposition resulted in more compact films, with PCEs reaching 1.8% and EQEs reaching 80% (refer to section 4.7) [201]. Beyond photovoltaics, bismuth oxyhalides could be used for photo-assisted water conversion. Bhachu *et al* synthesized thin films of BiOI, BiOBr

Table 3. Materials properties of direct x-ray detectors and their performance.

Material	Z_{avg}	$\mu\tau$ (cm^2 V^{-1})	Resistivity (Ω cm)	Sensitivity (μC Gy_{air}^{-1} cm^{-2})	Lowest detectable dose rate (μGy_{air} s^{-1})	References
Si	14	>1	10^4	8	<8300	[441–444]
a-Se	34	10^{-7}		20	5.5	[445, 446]
$Cd_xZn_{1-x}Te$	48.2–49.1	0.01	10^{10}	318	50	[447]
$MAPbBr_3$[a]	45.1	0.012	$\sim10^7$	2.1×10^4	0.039	[448]
BiI_3	60.5	10^{-5}	10^9–10^{11}	10^4	—	[449, 450]
$Cs_2AgBiBr_6$	53.1	6.3×10^{-3}	10^9–10^{11}	105	0.0597	[135]
$MA_3Bi_2I_9$	—	$\sim10^{-3}$	10^{10}–10^{11}	1.1×10^4	0.0006	[147]
$(NH_4)_3Bi_2I_9$	—	1.1×10^{-2}	10^6–10^8	0.8×10^4	0.210	[155]

[a] MA is $CH_3NH_3^+$.

and BiOCl by aerosol-assisted chemical vapor deposition (AA-CVD) and performed photoelectrochemical testing in a 0.5 mol l^{-1} Na_2SO_4 electrolyte (pH of 6.5), with a Pt counter electrode and Ag/AgCl reference electrode [296], and with 1 sun illumination. BiOI was found to not give any photocurrent at 0 V(RHE), suggesting that it would not reduce H^+. However, the photocurrent was ~0.1 mA cm^{-2} at 1.23 V(RHE), suggesting that the BiOI photoelectrochemical cells could oxidize water. BiOBr was also found to be capable of oxidizing water, with a photocurrent of ~0.3 mA cm^{-2} at 1.23 V(RHE). BiOCl showed very little photocatalytic activity. But all three materials were found to be unstable in the electrolyte. For example, the photocurrent from BiOBr at 1 V versus Ag/AgCl (1.6 V(RHE)) was found to decrease by 23% after 1 h, whereas BiOI at the same potential decreased after only 100 s [296]. Moreover, the photocurrents were significantly lower than those achieved with Cu_2O, which has a similar band gap. But recent Cu_2O photoelectrodes have used a heterojunction structure, as a well as a surface catalyst to improve the photocatalytic activity [423]. Similar strategies could be investigated for V–VI–VII materials.

5.3. Radiation detection

The detection of ionizing radiation (particularly x-rays and γ-rays) is important for a wide range of applications, including security screening, medical diagnostics and the characterization of materials [147, 433–435]. Furthermore, it is important to be able to detect and quantify heavy charged particles, such as α-particles, which are by-products from nuclear reactions [436]. The key properties of radiation detector materials are that they need to have a large: (1) average atomic number (Z_{avg}), (2) product of mobility and charge-carrier lifetime ($\mu\tau$), and (3) resistivity (>10^9 Ω cm [433, 434, 437]). A high atomic number is needed because the attenuation coefficient (α) of high energy photons is proportional to Z^4/E^3, where E is the photon energy [135, 291, 438]. A large $\mu\tau$ product is needed for the efficient extraction of charge-carriers because the thickness required to completely absorb radiation is often at the millimeter scale or larger [438]. The dependence of the photocurrent (I) from a radiation detector to the $\mu\tau$ product is given by the Hecht equation [434]:

$$I = \frac{I_0 \mu\tau V}{L^2} \frac{1 - e^{-L^2/\mu\tau V}}{1 + \frac{L}{V}\frac{s}{\mu}}. \quad (6)$$

In equation (6), I_0 is the saturated photocurrent, V the applied bias, L the thickness of the radiation detector, and s the surface recombination velocity. Typically $\mu\tau > 10^{-4}$–10^{-3} cm^2 V^{-1} is needed [439]. If the $\mu\tau$ product is low, a large applied field is needed to extract the carriers, but this can increase the dark current, which reduces the signal-to-noise ratio. A high resistivity is also needed to maintain a low dark current to achieve a high signal-to-noise ratio (which gives high image contrast), as well as the ability to detect lower doses of radiation (i.e. reduced lowest detectable dose rate). This is especially important for medical diagnostic applications and security screening, in which a lower dose of harmful radiation can be used, reducing the risk of causing cancer in the human subject. The lowest detectable dose rate required for medical applications is 50 mGy_{air} s^{-1} [435], but there is motivation to be able to detect lower doses down to 0.1 nGy_{air} s^{-1}, which is the background radiation levels in the US [135], and also because using lower doses improves the spatial resolution of the detector [135]. Note that the unit Gy (gray) represents the energy of ionizing radiation absorbed by a particular mass (1 Gy = 1 J kg^{-1}). The dark current can be reduced by increasing the band gap, and at room temperature, the band gap should be between 1.4 and 2.5 eV [429, 435, 437]. The upper limit to the band gap is so that the electron–hole ionization energy is small [437]. Another important parameter in radiation detectors is the sensitivity (S), which is defined as $S = (I_{ON} - I_{OFF})/(\text{dose rate}$ [155]). The sensitivity would therefore depend on Z, $\mu\tau$ product, as well as the dark current. The spatial resolution, response speed (which determines the duration of exposure to harmful radiation that is needed), energy resolution, linear dynamic range, uniformity and stability of the detectors are also important parameters [135, 434].

Often the materials used for radiation detectors are single crystals. This is because the penetration depth of radiation (from soft x-rays to hard γ-rays) are on the millimeter to centimeter scale. It is also because single crystals tend to have a lower defect density and larger $\mu\tau$ products than thin films. A common radiation detector is silicon. But silicon has a low

Z value and low band gap. Thus, despite its high $\mu\tau$ product, it has low stopping power, low resistivity, low sensitivity and a high lowest detectable dose rate (table 3). Silicon therefore tends to only be used for soft x-ray ($E < 10$ keV) detection and in portable detectors (e.g. for EDX or XRF [434]). Amorphous selenium (a-Se) has a higher Z value and therefore stronger stopping power for radiation. a-Se is the most common solid-state material for the direct detection of x-rays, but has a low $\mu\tau$ product. High applied biases are therefore needed, which leads to low sensitivities (table 3 [434]). Other alternatives contain toxic elements ($Cd_xZn_{1-x}Te$ and HgI_2 [434]), or require liquid nitrogen cooling (such as high purity Ge [429], which has a small band gap of 0.66 eV and needs cooling to reduce the dark current [434]). Beyond direct-conversion materials, radiation detection can also occur by the use of scintillators to absorb and down-convert the radiation to lower-energy photons that can be detected using standard silicon-based photodiodes [438]. But common scintillators are alkali halides doped with toxic Tl [434, 438], and have given lower resolution for imaging and lower linearity in their response to the radiation dose [429] than direct detectors. Recently, lead-halide perovskites have gained attention for radiation detectors, owing to their composition of high atomic number elements, the high $\mu\tau$ products achievable, their widely tunable band gaps, and their facile processability from solution [433, 435, 436, 438]. As a result, perovskite X-ray detectors can operate at room temperature with improved performance (in terms of sensitivity and lowest detectable dose rate) over a-Se and $Cd_xZn_{1-x}Te$ have been demonstrated (table 3). Furthermore, lead-halide perovskites have demonstrated promising radiation hardness to protons and γ-rays [434]. Lead-halide perovskites, with high PLQEs to visible light excitation, have also demonstrated reasonable x-ray excited luminescence yields at room temperature, making them suitable for consideration as scintillators [440]. The price of each perovskite single crystal is estimated to be US$0.5–1.0 cm^{-3} based on the price of the precursors [433]. By contrast $Cd_xZn_{1-x}Te$ single crystals cost $3000 cm^{-3}, in part due to the low demand for these materials for radiation detectors [434]. Despite these advantages, lead-halide perovskites have limited stability in air [145], and can degrade under continuous irradiation with high flux-density x-rays in air [17] for extended periods of time. In addition, the lead content of perovskite single crystals significantly exceeds the limited imposed by regulations on hazardous elements [135]. Ion migration in lead-halide perovskites could also result in drift in the dark current, which could increase the lowest detectable dose rate [147]. It is therefore important to consider perovskite-inspired materials for radiation detection.

Perovskite-inspired materials have many desirable properties for radiation detectors: the band gaps of most materials are within the ideal 1.4–2.5 eV range, and they are comprised of high atomic number elements (e.g. Bi and I). In particular, many of these materials are stable in air, have low toxicity and can be processed as single crystals using facile fabrication methods. Prior to the work on lead-halide perovskites, BiI_3 had already been investigated for radiation detectors [449–452]. BiI_3 has a band gap of 1.67 ± 0.09 eV [288], and can be grown as single crystals by the vertical Bridgman method and physical vapor transport [291, 450] (refer to section 3.7 for details). Owing to the high Z_{avg} of 60.5 and density (5.78 g cm^{-3}), the mass absorption coefficient is large (6.746 cm^2 g^{-1} at 60 keV). In addition, BiI_3 has a low ionization energy (5.8 eV) that is comparable to $Cd_xZn_{1-x}Te$ (5 eV) and lower than a-Se (45 eV). BiI_3 can therefore easily convert absorbed x-rays into charges through the photoelectric effect [450]. For device characterization, BiI_3 is used in a photoconductor structure owing to its high resistivity (10^9–10^{11} Ω cm), in which its dark current is several orders of magnitude smaller than its photocurrent. That is, BiI_3 has two ohmic contacts, usually Au or Pd [449, 450]. These can be applied on the front and back surface of the single crystal (planar) or both on the front surface (coplanar). Sun *et al* found that the planar structure resulted in 1.8-2.5 times higher sensitivities of ∼1.3 × 10^4 $\mu C\ Gy_{air}^{-1}\ cm^{-2}$, which are comparable to $MAPbBr_3$ and larger than $Cd_xZn_{1-x}Te$ or a-Se [450] (table 3). This was attributed to a more uniform electric field in the planar configuration [450]. Dmitriev *et al* used the planar configuration to measure an electron mobility-lifetime product of 10^{-5} $cm^2\ V^{-1}$ [449] through photoconductivity measurements.

By contrast, $Cs_2AgBiBr_6$, $MA_3Bi_2I_9$ and $(NH_4)_3Bi_2I_9$ single crystals are grown from solution [135, 147, 155]. Au electrodes were used for $Cs_2AgBiBr_6$ and $MA_3Bi_2I_9$ radiation detectors [135, 147], whereas Ag was painted the $(NH_4)_3Bi_2I_9$ single crystal [155]. The ionization energies for these materials are low: 5.61 eV for $Cs_2AgBiBr_6$ [135] and 5.47 eV for $(NH_4)_3Bi_2I_9$ [155]. As-grown $Cs_2AgBiBr_6$ was reported to have a trap density of 4.54 × 10^9 cm^{-3} and mobility of 3.17 cm^2 V^{-1} s^{-1}, as determined from space-charge limited current measurements. By post-annealing the single crystals at 100 °C for 2 h in N_2, the trap density was reduced to 1.74 × 10^9 cm^{-3}, whereas the mobility increased to 11.81 cm^2 V^{-1} s^{-1}. This resulted in the $\mu\tau$ product increasing from 3.75 × 10^{-3} to 6.3 × 10^{-3} $cm^2\ V^{-1}$, which is larger than a-Se and BiI_3 (table 3). The surface recombination velocity was reduced by washing the single crystals in isopropanol to remove surface defect states, resulting in the resistivity increasing to 10^{11} Ω cm. Despite these promising properties, and despite $Cs_2AgBiBr_6$ having a higher Z_{avg} than $MAPbBr_3$, the sensitivity achieved was only 8 $\mu C\ Gy_{air}^{-1}\ cm^{-2}$, which increased to 105 $\mu C\ Gy_{air}^{-1}\ cm^{-2}$ after applying an electric field of 25 V mm^{-1}. However, the larger resistivity led to a low dark current (∼0.15 nA cm^{-2} at 5 V) and therefore a small lowest detectable dose rate of 0.0597 $\mu C\ Gy_{air}\ s^{-1}$ [135]. A smaller lowest detectable dose rate and significantly larger sensitivity were achieved with $MA_3Bi_2I_9$ single crystals, which have a 0 D crystal structure (table 3 [147]). This may be due to the wide band gap and high resistivity (10^{11} Ω cm in the out-of-plane direction) resulting in a low dark current of only 0.98 nA cm^{-2} at 120 V bias [147]. Notably the activation energy barrier for ion migration was found to be 0.31–0.46 eV [147], comparable

Table 4. Properties of direct γ-ray and α-particle detectors.

Material	Z_{avg}	$\mu\tau$ ($cm^2\ V^{-1}$)[a]	Resistivity (Ω cm)	Energy resolution (%)	References
Gamma ray detector					
HPGe	32	>1	10^2–10^3	0.2	[456, 457]
$Cd_xZn_{1-x}Te$	48.2–49.1	0.004–0.01	10^{10}	0.5	[458, 459]
$CsPbBr_3$	65.9	1.34×10^{-3}	10^{11}	3.8–3.9	[455]
$Sb:BiI_3$	60.5	10^{-4}	10^8–10^{10}	2.2	[439]
Alpha particle detector					
$Cd_xZn_{1-x}Te$	48.2–49.1	10^{-3}–10^{-2}	10^{10}	~1%	[456, 460, 461]
$CsPbBr_3$	65.9	9.5×10^{-4}	10^9	15%	[436]
BiI_3	60.5	—	10^{10}	40.2%	[439, 451, 452]
$Sb:BiI_3$	60.5	—	10^9	33%–66%	[291]
$Cs_3Bi_2I_9$	57.7	5.4×10^{-5}	9.4×10^{12}	—	[429]
$Cs_3Sb_2I_9$	53.1	1.1×10^{-5}	5.2×10^{11}	—	[429]
$Rb_3Bi_2I_9$	53.9	1.7×10^{-6}	3.2×10^{11}	—	[429]
$Rb_3Sb_2I_9$	49.3	4.5×10^{-6}	8.5×10^{10}	—	[429]

[a] The highest $\mu\tau$ product is shown for anisotropic materials.

to $Cs_2AgBiBr_6$ (0.35 eV) and larger than $MAPbBr_3$ (0.19 eV [155]). A higher activation energy barrier was found for $(NH_4)_3Bi_2I_9$. $(NH_4)_3Bi_2I_9$ is a layered material, and the activation energy barrier was found to be higher in the [001] direction (i.e. between planes; 0.91 eV see 0.72 eV along the [99] direction [155]). Owing to the layered structure, $(NH_4)_3Bi_2I_9$ exhibited anisotropic transport properties, in which higher $\mu\tau$ products and sensitivities were obtained in the [99] direction (1.1×10^{-2} $cm^2\ V^{-1}$; 0.8×10^4 $\mu C\ Gy_{air}^{-1}\ cm^{-2}$) than the [001] direction (4.0×10^{-3} $cm^2\ V^{-1}$; 803 $\mu C\ Gy_{air}^{-1}\ cm^{-2}$). However, the signal to noise ratio in the [001] direction was found to be larger, leading to a smaller lowest detectable dose rate of 0.055 $\mu Gy_{air}\ s^{-1}$ (see 0.210 $\mu Gy_{air}\ s^{-1}$ in the [99] direction), which was attributed to reduced ion migration [155]. All three materials were found to be stable in ambient air and withstand temperatures >200 °C [135, 147, 155].

Beyond the direct conversion of x-rays to electrical energy, perovskites have also been investigated as scintillators. A recent work found $CsPbBr_3$ nanocrystals to demonstrate significantly higher sensitivity than $Bi_4Ge_3O_{12}$ (one of the standard scintillator materials), and have a sensitivity to x-rays on the same order of magnitude as CsI:Tl [453]. Recently, $(C_8H_{17}NH_3)_2SnBr_4$ was demonstrated as a lead-free perovskite scintillator. These had a PLQE of 98%. It was suggested that the mechanism for x-ray induced emission (radioluminescence) was photoelectric ionization, followed by relaxation to the band-edge to form excitons that recombine radiatively. The radioluminescence spectrum was found to be almost the same as the PL spectrum. The emission peak was centered at 596 nm, which is detectable by standard CCDs. The tin-based perovskite was made into a composite with PMMA. The radioluminescence was found to be linear with the x-ray dose down to 104 $\mu Gy\ s^{-1}$, which is a sufficiently low dose to be safely used in x-ray imaging. The spatial resolution achieved with the perovskite scintillator/CCD system was 200 μm, which was lower than reported for lead-based perovskite systems. The tin-based perovskite/PMMA composite also demonstrated no decrease in radioluminescence intensity after cycled x-ray exposure over 800 s [454].

In γ-ray detection, the energy resolution of the detector is an important parameter. This is because the detector needs to accurately identify the characteristic spectrum of specific radionucleotides. Although high energy resolution can be achieved with high purity Ge and $Cd_xZn_{1-x}Te$ (table 4), these materials are limited by their need to operate at cryogenic temperatures or high cost, respectively, as discussed above. Recently, He *et al* achieved high sensitivity γ-ray detectors using $CsPbBr_3$ single crystals, which demonstrated an energy resolution of 3.8%–3.9% (FWHM relative to the energy of the peak) for the γ-ray peak [455]. In perovskite-inspired materials, there has been extensive work on BiI_3 for γ-ray detection. The total attenuation length for photoelectric absorption (the main process by which γ-rays are converted to electron–hole pairs) in BiI_3 is smaller than $Cd_xZn_{1-x}Te$ (figure 25(b)) due to the higher Z_{avg} for BiI_3 [429] (table 4). But despite the high Z_{avg} and reasonable $\mu\tau$ products demonstrated in x-ray detectors, BiI_3 capable of detecting moderate energy γ-rays (>100 keV) have only been recently demonstrated. The limited performance has been attributed to the formation of voids and defects in BiI_3 during growth by the vertical Bridgeman method [439]. The density of iodine vacancies was found to be reduced through Sb doping, which led to improved resistivities (from 1.45×10^8 Ω cm for BiI_3 to 2.63×10^9 Ω cm for $Sb:BiI_3$) and a four-order-of-magnitude reduction in the leakage current in BiI_3 single crystals [291]. The higher-quality $Sb:BiI_3$ crystals demonstrated an energy resolution of 2.2% for ^{137}Cs (662 keV) radiation [439], substantially lower than reported for $CsPbBr_3$ [455].

Beyond x-rays and γ-rays, the detection of α-particles is important because these are the byproducts of nuclear reactions and nuclear decays [436]. $\mu\tau$ particles are also used in

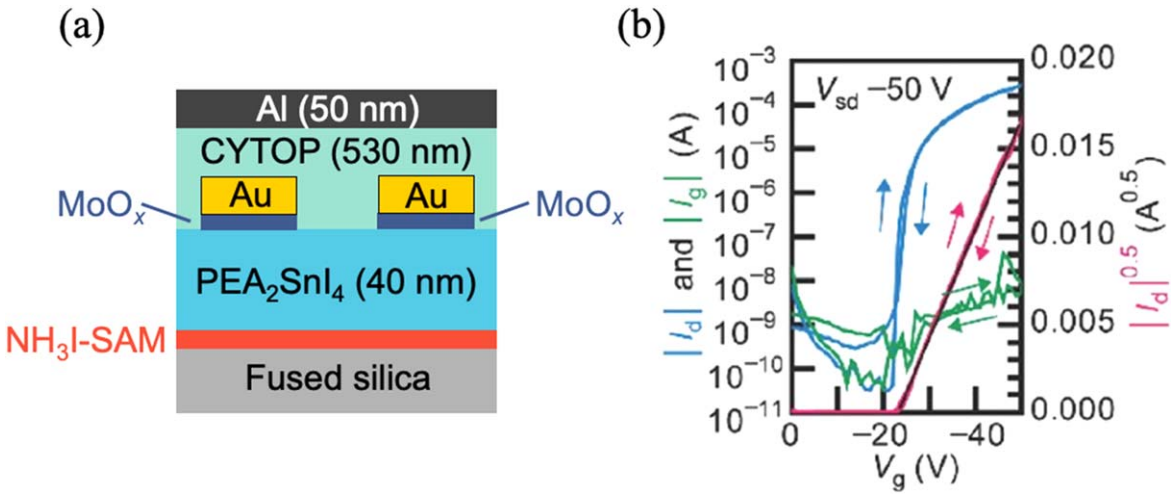

Figure 26. $(PEA)_2SnI_4$ perovskite TFTs: (a) device structure and (b) transfer curves. [465] John Wiley & Sons. © 2016 WILEY-VCH Verlag GmbH & Co. KGaA, Weinheim.

the measurement of composition, such as in Rutherford backscattering spectrometry. The energy resolution of the α-particle detector is therefore an important factor. In testing α-particle detectors, 5.5 MeV α-particles from an ^{241}Am source are commonly used [291, 429, 436, 452, 461]. Current work on perovskite and perovskite-inspired materials for α-particle detectors have not demonstrated energy resolutions or $\mu\tau$ products matching industry-standard $Cd_xZn_{1-x}Te$ (table 4). In fact, the defect perovskites ($A_3B_2I_9$ materials) are not able to resolve the α-particle peak, and have low $\mu\tau$ products. This was attributed to the low mobilities, which limit the charge collection efficiency [429]. By contrast, Sb:BiI_3 single crystals were found to have electron mobilities of 1000 ± 200 cm^2 V^{-1} s^{-1}, which are similar to the mobilities of $Cd_xZn_{1-x}Te$ [291]. Sb:BiI_3 demonstrated an energy resolution of 66% to α-particles, which improved to 33% after applying an electric field of 532 V cm^{-1} for 8 h, and the improvement in resolution was attributed to reduced leakage currents [291]. $CsPbBr_3$ single crystals were also found to be capable of resolving the α-particle peak, demonstrating an energy resolution of 15%. An important factor was the high mobilities of 63 cm^2 V^{-1} s^{-1} for electrons and 49 cm^2 V^{-1} s^{-1} for holes, leading to reasonable $\mu\tau$ products reaching up to 10^{-3} cm^2 V^{-1} [436]. Future efforts to improve the performance of defect perovskites for α-particle detection should focus on improving the mobility [429]. While the mobilities could be limited due to strong-electron phonon coupling, defect perovskite x-ray detectors have achieved $\mu\tau$ products reaching 10^{-2} cm^2 V^{-1} s^{-1} (table 3), and improved performance may be expected from these materials for α-particle detection.

5.3.1. Electronic devices. Two critical electronic devices are thin film transistors (TFTs) and memristors. The operating principles of these devices can be found in review articles, such as [28, 438]. TFTs are ubiquitously used in electronic circuits, in which they are used as switches, for amplification, as well as for the fabrication of logic devices (particularly the Complementary Metal Oxide Semiconductor or CMOS). Memristors are actively explored for next-generation terabyte-scale non-volatile memory storage that can be operated with low power. Historically, the materials considered for these applications have been silicon or oxides [28, 438]. But more recently, lead-halide perovskites have been actively explored for these applications with promising results [28, 438]. As with all other electronic applications, it will be important to reduce the lead content used in these devices, as well as improve the stability under operation.

In TFTs, tin-based perovskites have been widely explored as a lead-free alternative. In fact, the first organic-inorganic perovskite TFT was a 2D tin-based perovskite ($(C_6H_5C_2H_4NH_3)_2SnI_4$ or $(PEA)_2SnI_4$), reported by Mitzi *et al* well before lead-halide perovskites were actively considered for photovoltaics. This TFT demonstrated *p*-channel character with a field-effect mobility of 0.6 cm^2 V^{-1} s^{-1} [462]. Significantly higher electron mobilities have recently been reported in lead-based perovskites, with field-effect mobilities exceeding 10 cm^2 V^{-1} s^{-1} demonstrated at room temperature [463], which is comparable to the electron field-effect mobility of strontium titanate perovskites [28]. We note that an electron mobility of 396 cm^2 V^{-1} s^{-1} has been reported from $MAPbI_3$ TFTs at room temperature [464], but there is uncertainty on whether this was overestimated. Recently, tin-based perovskite TFTs have been demonstrated with hole field-effect mobilities exceeding those of lead-based perovskites [463]. This was achieved by Matshushima *et al* using the same material previously reported by Mitzi *et al* Critical improvements were: (1) the passivation of the surface of PEA_2SnI_4 with self-assembled monolayers of NH_3I-SAM, and (2) the development of the top-gate, top-source/drain device structure (figure 26(a)) to ensure both surfaces are passivated. These led to minimal hysteresis in the transfer curves (figure 26(b)), with the hole field-effect mobilities reaching 15 cm^2 V^{-1} s^{-1} [465] and on/off ratios reaching 10^6. *p*-type TFTs are especially important because CMOS requires both *n*- and *p*-type TFTs, and fewer options for high-performing *p*-type TFTs are currently

available. The hole mobility of $MASnI_3$ single crystals has been found to be at least an order of magnitude larger than the field-effect mobilities achieved thus far (refer to section 3), and it is expected that the in-plane mobility of 2D $(PEA)_2SnI_4$ is comparably high [465]. Thus, future improvements in the hole field-effect mobility could be expected. However, $(PEA)_2SnI_4$ has low stability, and TFTs have been found to degrade quickly, even when they are in high vacuum or inside a glovebox [466]. Improved stability was achieved by replacing PEA with the π-conjugated oligothiphene ligand 4 Tm (4 Tm = 2-(3‴,4′-dimethyl-[2,2′:5′,2″:5″,2‴-quaterthiophen]-5-yl)ethan-1-ammonium). $(4\,Tm)_2SnI_4$ perovskite TFTs were found to retain their performance after storage in air for a month. TFTs were made using a bottom gate, top-source/drain structure, which gave a hole field-effect mobility of 2.32 $cm^2\ V^{-1}\ s^{-1}$ and an on/off ratio of 10^5–10^6. While the field-effect mobility is lower than that reported by Matshushima *et al* a different structure was used; $(PEA)_2SnI_4$ TFTs made in the same structure as the $(4Tm)_2SnI_4$ TFTs had a field-effect mobility of 0.15 $cm^2\ V^{-1}\ s^{-1}$, with an on/off ratio of 10^4–10^5 [466].

Memristors are devices with variable resistance states, which depend on the applied voltage and current history [467]. Such devices were first proposed as a fourth fundamental circuit element in 1971 (along with resistors, inductors and capacitors) [468], and realized in 2008 [469]. These variable resistance states can be used for high-density memory storage, logical computations, as well as for neuromorphic computing [467]. Such devices switch between resistance states through the application of an electric field. As such, memristors have low power consumption and retain their resistance states after the electric field has been removed, which contrasts to common commercial non-volatile memory (e.g. NAND flash [470]). The key requirements for memristors are (1) rapid switching between the high and low resistance states, (2) low operating voltage (for set/reset and read), (3) large ratio in resistance of the on and off states (on/off ratio), (4) large endurance (number of switching cycles in which the resistance states are maintained), and (5) long retention time [438] of the resistance states after power has been removed. Thin film memristors are typically comprised of an insulator sandwiched between two degenerate contacts (e.g. metal–insulator–metal structure). Wide band gap oxides are commonly used for the insulator layer, such as TaO_x, HfO_2 and $SrRuO_3$, which have achieved on/off ratios ranging from 10 to 10^3, endurances ranging from 10^3–10^{10} cycles, and retention times between 10^4 s and 10 y [438]. Lead-halide perovskites ($MAPbI_3$, $CsPbBr_3$ and 2D perovskites, among others) have recently been demonstrated to exhibit resistive switching, with high on/off ratios reaching 10^7 and rapid switching between resistance states (640 μs) but lower endurances of up to 3000 cycles. Retention times up to 10^5 s have been measured, but the set/reset voltages are lower than their oxide counterparts (which commonly have set/reset voltages with absolute values exceeding 1 V) [438]. But as with many other optoelectronic device applications, the need eliminate toxic lead from memristors has motivated the exploration of perovskite-inspired materials for resistive switching [467, 470–472].

The wide band gaps of many perovskite-inspired materials leads to a low dark resistance, which is advantageous for achieving a high resistance in the off state. The ability to process these materials using low temperature, facile methods is also advantageous and makes the materials compatible with flexible substrates [470]. At the same time, these materials have low formation energies for vacancies (especially halides), which can act as conductive filaments in resistive switching [471]. This ionic vacancy conduction mechanism (known as valence change memory) has been identified in $MASnBr_3$, $CsSnI_3$ and $Cs_3Sb_2Br_9$ memristors [467, 470, 471] using inert Au electrodes. For $MASnBr_3$ and $Cs_3Sb_2Br_9$, the conducting filaments are attributed to bromide vacancies [467, 471]. When a bias exceeding the set voltage is applied, Br^- accumulate at the anode, while bromide vacancies form and accumulate at the cathode [467, 471]. The Br^- may be oxidized to Br atoms that are stored in the inert electrode [467]. The bromide vacancies have a low activation energy barrier to migration (0.22–0.57 eV), and these vacancies can form a conductive channel bridging the two electrodes, resulting in the memristor switching from the high to low resistance state. Composition and Raman measurements have shown that the segregation of Br occurs. Applying a negative reset voltage causes the Br atoms to diffuse away from the electrode they were stored at and recombine with the halide vacancies, causing the conductive filaments to rupture and the memristor return to the high resistance state [467, 471]. The conductive filaments for $CsSnI_3$ has been attributed to tin vacancies, which form and are removed in a similar manner to bromide vacancies [470]. Valence change memory has also been suggested as the mechanism for resistive switching in BiOI memristors, which are believed to form conductive filaments through oxygen vacancies [473].

An alternative to valence change memory for the formation of conductive filaments is through electrochemical metallization (ECM), in which a reactive metal anode (often Ag) is oxidized when an electric field is applied. The metal cations are the conductive filament and migrate through the solid film electrolyte to the cathode, where they are reduced and electrocrystallize to form the metal again. To reset the device from the low to high resistance state, a negative bias is applied, which results in the dissolution of the conducting filaments through Joule-heating assisted dissolution [470]. This ECM mechanism was found to occur in $CsSnI_3$ and $Cs_3Cu_2I_5$ memristors with Ag top electrodes. In both devices, a layer of polymethyl methacrylate (PMMA) was spin coated over the perovskite-inspired materials to improve its stability in ambient air, as well as preventing the reaction between Ag and the iodide-based thin film, which is important for improving the endurance of the devices [470, 472]. The PMMA layer did not act as a barrier to silver dissolution and migration, allowing resistive switching to occur. Han *et al* compared $CsSnI_3$ memristors using Ag versus Au electrodes to compare the ECM and VCM mechanisms. They found the memristors operating based on ECM to give improved on/off ratios (>1000) and low set/reset voltages of 0.13 and −0.08

Table 5. State-of-the-art performance of perovskite-inspired materials in the applications covered in section 5.

Application	Active material	Performance properties	Performance values	References
Phosphor for white-light LEDs	$Cs_2(Ag_{0.6}Na_{0.4})InCl_6$with 0.04% Bi^{3+}	PLQE	86 ± 5%	[124]
		CIE coordinates	(0.396, 0.448)	
		Color temperature	4054	
LED	FPMAI-$MAPb_{0.6}Sn_{0.4}I_3$	PLQE	—	[402]
		EQE	5.0	
		EL wavelength	917	
		EL FWHM	80 nm	
Photocatalysis	$Cs_3Sb_2Br_9$ nanocrystals	Precursor	CO_2 (g)	[417]
		Light source	1 sun AM 1.5G	
		Product	CO	
		Yield	516 μmol g^{-1} (5 h)	
X-ray detector	$MA_3Bi_2I_9$ single crystals	$\mu\tau$	$\sim10^{-3}$ cm^2 V^{-1}	[147]
		Sensitivity	1.1×10^4	
		Lowest detectable dose rate	0.0006	
Gamma-ray detector	Sb:BiI_3 single crystals	$\mu\tau$	10^{-4}	[439]
		Energy resolution	2.2% (662 keV)	
α-particle detector	Sb:BiI_3 single crystals	Energy resolution	33%–66% (5.5 MeV)	[291]
Thin film transistor	$(C_6H_5C_2H_4NH_3)_2SnI_4$ thin films	Hole mobility	12 ± 1 (max. 15) cm^2 V^{-1} s^{-1}	[465]
		Threshold voltage	−22 ± 2 V	
		I_{ON}/I_{OFF}	$(1.9 \pm 2.1) \times 10^6$	
Memristor	$CsSnI_3$ (orthorhombic phase; Ag top electrode)	SET voltage	0.13 V	[470]
		RESET voltage	−0.08 V	
		On/off ratio	$>10^3$	
		Endurance	>600 cycles	
		Retention time	$>7 \times 10^3$ s	

V (with an electroforming voltage of 0.36 V), whereas VCM memristors gave improved retention (10^4 s [470]).

To summarize the devices discussed in section 5, a comparison of the state-of-the-art performance of perovskite-inspired materials across all applications is given in table 5.

6. Conclusions and outlook

Lead-halide perovskites have developed at an unprecedented rate in photovoltaics due to an ideal set of optoelectronic properties. Among these properties is its tolerance to point defects, which allows perovskite devices to achieve high efficiencies despite being processed at low temperature using simple fabrication methods that give rise to high densities of point defects. This contrasts to traditional semiconductors, such as silicon and III–V compounds, and has spurred efforts to identify 'perovskite-inspired materials' that could replicate the exceptional optoelectronic properties of LHPs, but which are free from the toxicity burden of lead and which are also more thermally and environmentally stable. The effort to develop PIMs is a multi-disciplinary challenge involving theorists, experimentalists and device engineers.

For theorists, the primary challenges have been: (1) unveiling the origins of the tolerance of LHPs to point defects, and (2) developing improved approaches to design PIMs [474]. As discussed in section 2.2, defect tolerance is a phenomenon that rarely originates from any single material property. Indeed, there are several factors which can contribute to the defect tolerance of a material, each with different levels of efficacy and rarity. To achieve the remarkable defect tolerance of LHPs, successful PIMs will likely be required to replicate the wealth of 'defect-tolerant' material properties exhibited by LHPs (atypical band structure, strong dielectric screening, anharmonic carrier capture etc). Through deeper understanding of defect-tolerant properties and their interrelationships, as well as extending the materials discovery abstraction pyramid (figure 2) to the explicit treatment of crystal defects, the accuracy of predictions for next-generation, high-performance PIMs will be improved immensely.

For materials design, recent years have witnessed an explosion in the popularity of data mining (materials informatics) and ML procedures, which promise to revolutionize the materials discovery process [30, 37, 474]. An inspiring, prototypical example is the use of text mining and natural language processing to extract previously-hidden insights from the vast dataset of materials science literature. In 2019, Ceder *et al* exemplified this concept by retrieving nearly 20 000 'codified synthesis recipes' from over 50 000 paragraphs in the recent solid-state literature [475]. In addition to pure data mining, the integration of

physics-based ML models into the high-throughput screening process could significantly augment the power and efficiency of materials discovery. For instance, by implementing accurate ML models of material stability and chemical descriptors as a pre-screening step, before the application of expensive electronic structure theory (i.e. DFT), the computational load could be considerably reduced, thereby accelerating the process and affording the use of expanded input compositional space [474]. Moreover, ML techniques may be leveraged to uncover subtle chemical trends in successful candidate materials (e.g. defect-tolerant material properties), which may not be initially apparent to the 'human eye' [37]. Indeed, the ability to physically interpret trained ML models and distinguish causation from correlation is an ongoing area of research [476].

For materials scientists, chemists, physicists and engineers, one of the main challenges has been to develop suitable fabrication methods for each class of materials. A wide range of methods have been investigated, from solution processing to chemical and physical vapor deposition (which can be used at scale), through to 'hybrid' methods that combine both solution- and vapor-based processing. A series of dedicated efforts has led to pinhole-free thin films being achieved across a wide range of materials, with methods to control the grain size and preferred orientation demonstrated, which all have led to improvements in the performance of the materials in devices. Furthermore, it has been widely shown across many families of PIMs that the materials are more stable thermally and in air compared to LHPs (e.g. $Cs_2AgBiBr_6$ and BiOI). There are a handful of exceptions, namely tin- and germanium-based perovskites, as well as InI (owing to In being unstable in the +1 oxidation state). But the incorporation of additives and developing 2D structures have been utilized to enhance their ambient stability. Critically, defect tolerance has been demonstrated computationally across several materials, such as BiOI, $CuSbS_2$ and $CuSbSe_2$.

One of the challenges across many PIMs is their wide band gaps, which are not suitable for single-junction photovoltaic devices. Although these materials may be used as top-cells in tandems, recent work has shown these materials to also hold significant promise in applications beyond PV. For example, in light-emission applications, photocatalysis and radiation detectors, wide band gaps of 2 eV or larger are advantageous, which compounded with the stability of these materials, makes them of practical interest for these applications. For example, inorganic double perovskites have been demonstrated as efficient, stable white-light emitters, which will be important for solid-state lighting. Many PIMs have suitable band positions to reduce H^+ or CO_2, and $Cs_3Sb_2Br_9$ nanocrystals were demonstrated to more efficiently reduce CO_2 than $CsPbBr_3$. In radiation detectors, the wide band gap of PIMs results in low dark current, which is important for them to achieve a high signal-to-noise ratio, with a low lowest detectable dose rate, down to 0.6 $nGy_{air}\ s^{-1}$ in $MA_3Bi_2I_9$. This is smaller than the lowest dose detectable by $MAPbBr_3$ as well as standard x-ray detectors, such as a-Se and CZT, and will allow lower and safer doses of x-rays to be used in security equipment or in medical screening. Furthermore, the composition of PIMs of high atomic number elements allows these materials to have high stopping power for radiation, which in turn results in sensitivities to X-rays being comparable to $MAPbBr_3$ and orders of magnitude larger than conventional Si, a-Se and CZT materials. The high resistivities of PIMs owing to their wide band gap is also advantageous for achieving a high resistance 'off' state in memristors, and on/off ratios comparable to or larger than conventional oxide-based materials have been reported. The exploration of PIMs in these electronic applications is still in the nascent stages, but there are already very promising signs of the potential of these low-toxicity materials to give stable, efficient performance.

However, an important challenge faced by the field is the limited mobility of some PIMs. Many PIMs either have a 0D crystal structure (e.g. $Cs_3Bi_2I_9$), or a 0D electronic structure (e.g. $Cs_2AgBiBr_6$), which limits mobilities and drift/diffusion lengths. Furthermore, these lower-dimensional materials have higher exciton binding energies, as well as soft lattices and strong electron–phonon coupling. These factors further restrict mobilities due to the formation of excitons (which need to be split to free carriers), as well as polarons or self-trapped excitons. This limits the current densities and efficiencies in PVs, as well as the $\mu\tau$ product of PIM single crystals, which are lower than in standard radiation detector materials. The main exception to the low mobilities in PIMs are tin-based perovskites, which have disperse bands. Indeed, this has resulted in these materials achieving field-effect mobilities comparable to LHPs in *p*-type TFTs.

Many PIMs also have crystal structures based on low dimensional networks (e.g. 1D and 2D connectivity), which leads to certain crystallographic orientations having higher mobility. This anisotropy in carrier transport necessitates careful control over the preferred orientation of the materials in thin films, such that: (1) the high mobility directions connect both electrodes in devices, while (2) also maintaining a compact morphology that does not lead to shunting. For example, BiOI has a layered structure, and a {012} preferred orientation is desirable to connect the top and bottom electrodes in vertically-structured PV devices. But this open structure leads to low shunt resistances, which limits open-circuit voltages. New device structures or strategies that allow high mobility and high shunt resistance to be simultaneously achieved are needed.

Beyond these materials and fabrication challenges, further efforts are needed to identify the cause of defect tolerance. While some ns^2 compounds have been found to be defect tolerant, others have been found to have deep traps, e.g. BiI_3 and SbI_3. A deeper understanding of defect tolerance will be necessary to develop increasingly refined, accurate, and comprehensive design principles, and thus more efficient, targeted screening procedures. On the computational front, recent advances in theory and technology have enabled both the qualitative and quantitative descriptions of bulk and defect-related material properties from *ab-initio* modelling. Overcoming the challenges associated with complex defect calculations (section 2.3.5) will facilitate accurate prediction and validation of promising candidate materials, alongside enhanced understanding of experimental results and defect behavior.

Ultimately, for future research efforts in materials discovery to be successful, consensus and consistency with selection metrics will be immensely beneficial, allowing greater transferability and comparability between studies. For

similar reasons, alongside the reduction of duplicate work, the facilitation of sharing both data and methodologies should be vehemently encouraged. Frameworks which automate this process (e.g. AiiDA [98] for materials modelling), maintaining data provenance and reproducibility, will be especially advantageous in this regard. This effort should not be limited to only computational data, but also experimental data (e.g. optical and transport measurements) and synthesis details. This will help to refine computational models, as well as providing 'training' datasets for more general ML models. Overall, the future of PIMs research will require an interlinked, synergistic approach between theory and experiment in order to identify further promising materials.

Acknowledgments

Yi-Teng Huang acknowledges funding from Ministry of Education from Taiwan Government as well as Downing College Cambridge. Seán R Kavanagh acknowledges funding from the EPSRC Centre for Doctoral Training in Advanced Characterisation of Materials (CDT-ACM)(EP/S023259/1), as well as the use of VESTA [477] (for crystal structure visualization) and Freepik.com (for vector image templates) in the preparation of figure 2. David O Scanlon acknowledges support from the European Research Council, ERC (Grant 758345). Aron Walsh acknowledges supportfor this work by a National Research Foundation of Korea (NRF) grant funded by the Korean government (MSIT) (No. 2018R1C1B6008728). Robert L Z Hoye acknowledges support from the Royal Academy of Engineering under the Research Fellowships scheme (No. RF\201718/1701), Downing College Cambridge via the Kim and Juliana Silverman Research Fellowship, and the Isaac Newton Trust (Minute 19.07(d)).

ORCID iDs

Yi-Teng Huang https://orcid.org/0000-0002-4576-2338
Seán R Kavanagh https://orcid.org/0000-0003-4577-9647
David O Scanlon https://orcid.org/0000-0001-9174-8601
Aron Walsh https://orcid.org/0000-0001-5460-7033
Robert L Z Hoye https://orcid.org/0000-0002-7675-0065

References

[1] Haegel N M *et al* 2019 Terawatt-scale photovoltaics: transform global energy *Science* **364** 836–8
[2] Hermann W A 2006 Quantifying global exergy resources *Energy* **31** 1685–702
[3] Kurtz S R *et al* 2020 Revisiting the terawatt challenge *MRS Bull.* **45** 159–64
[4] Needleman D B *et al* 2016 Economically sustainable scaling of photovoltaics to meet climate targets *Energy Environ. Sci.* **9** 2122–9
[5] Polman A, Knight M, Garnett E C, Ehrler B and Sinke W C 2016 Photovoltaic materials: present efficiencies and future challenges *Science* **352** 6283
[6] Kojima A *et al* 2009 Organometal halide perovskites as visible-light sensitizers for photovoltaic cells *J. Am. Chem. Soc.* **131** 6050–1
[7] National Renewable Energy Laboratory 2020 *Best Research-Cell Efficiency Chart.* (https://doi.org/https://www.nrel.gov/pv/cell-efficiency.html)
[8] Mailoa J P *et al* 2015 A 2-terminal perovskite/silicon multijunction solar cell enabled by a silicon tunnel junction *Appl. Phys. Lett.* **106** 121105
[9] Bailie C D *et al* 2015 Semi-transparent perovskite solar cells for tandems with silicon and CIGS *Energy Environ. Sci.* **8** 956–63
[10] Li Z *et al* 2018 Cost analysis of perovskite tandem photovoltaics *Joule* **2** 1559–72
[11] Dagar J, Castro-Hermosa S, Lucarelli G, Cacialli F and Brown T M 2018 Highly efficient perovskite solar cells for light harvesting under indoor illumination via solution processed SnO_2/MgO composite electron transport layers *Nano Energy* **49** 290–9
[12] Babayigit A, Ethirajan A, Muller M and Conings B 2016 Toxicity of organometal halide perovskite solar cells *Nat. Mater.* **15** 247–51
[13] Bush K A *et al* 2017 23.6%-efficient monolithic perovskite/silicon tandem solar cells with improved stability *Nat. Energy* **2** 17009
[14] Walsh A and Stranks S D 2018 Taking control of ion transport in halide perovskite solar cells *ACS Energy Lett.* **3** 1983–90
[15] Ganose A M, Savory C N and Scanlon D O 2017 Beyond methylammonium lead iodide: prospects for the emergent field of ns^2 containing solar absorbers *Chem. Commun.* **53** 20–44
[16] Lee L C, Huq T N, Macmanus-Driscoll J L and Hoye R L Z Z 2018 Research update: bismuth-based perovskite-inspired photovoltaic materials *APL Mater.* **6** 084502
[17] Hoye R L Z *et al* 2017 Perovskite-inspired photovoltaic materials: toward best practices in materials characterization and calculations *Chem. Mater.* **29** 1964–88
[18] Brandt R E *et al* 2017 Searching for 'defect-Tolerant' photovoltaic materials: combined theoretical and experimental screening *Chem. Mater.* **29** 4667–74
[19] Ke W, Stoumpos C C and Kanatzidis M G 2019 'Unleaded' perovskites: status quo and future prospects of tin-based perovskite solar cells *Adv. Mater.* **31** 1803230
[20] Igbari F, Wang Z K and Liao L S 2019 Progress of lead-free halide double perovskites *Adv. Energy Mater.* **9** 1803150
[21] Correa-Baena J-P P *et al* 2018 A-site cation in inorganic $A_3Sb_2I_9$ perovskite influences structural dimensionality, exciton binding energy, and solar cell performance *Chem. Mater.* **30** 3734–42
[22] Rosales B A, White M A and Vela J 2018 Solution-grown sodium bismuth dichalcogenides: toward earth-abundant, biocompatible semiconductors *J. Am. Chem. Soc.* **140** 3736–42
[23] Swarnkar A *et al* 2019 Are chalcogenide perovskites an emerging class of semiconductors for optoelectronic properties and solar cell? *Chem. Mater.* **31** 565–75
[24] Crovetto A *et al* 2020 Parallel evaluation of the BiI_3, BiOI, and Ag_3BiI_6 layered photoabsorbers *Chem. Mater.* **32** 3385–95
[25] Audzijonis A *et al* 2007 Electronic structure of the BiSI cluster *Physica* B **391** 22–7
[26] Wei Q *et al* 2018 Synthesis of easily transferred 2D layered BiI_3 nanoplates for flexible visible-light photodetectors *ACS Appl. Mater. Interfaces* **10** 21527–33
[27] Wang W, Huang G, Jimmy C Y and Wong P K 2015 Advances in photocatalytic disinfection of bacteria:

development of photocatalysts and mechanisms *J. Environ. Sci.* **34** 232–47
[28] Wu T, Pisula W, Rashid M Y A and Gao P 2019 Application of perovskite-structured materials in field-effect transistors *Adv. Electron. Mater.* **5** 1900444
[29] Alberi K *et al* 2018 The 2019 materials by design roadmap *J. Phys. D: Appl. Phys.* **52** 13001
[30] Davies D W *et al* 2016 Computational screening of all stoichiometric inorganic materials *Chem* **1** 617–27
[31] Perdew J P *et al* 2008 Restoring the density-gradient expansion for exchange in solids and surfaces *Phys. Rev. Lett.* **100** 039902
[32] Cococcioni M and deGironcoli S 2005 Linear response approach to the calculation of the effective interaction parameters in the LDA + U method *Phys. Rev.* B **71** 35105
[33] Klimeš J, Bowler D R and Michaelides A 2011 Van der Waals density functionals applied to solids *Phys. Rev.* B **83** 195131
[34] Grimme S, Antony J, Ehrlich S and Krieg H 2010 A consistent and accurate *ab initio* parametrization of density functional dispersion correction (DFT-D) for the 94 elements H-Pu *J. Chem. Phys.* **132** 154104
[35] Jaśkaniec S, Kavanagh S R, Coelho J, Hobbs C, Walsh A, Scanlon D O and Nicolosi V 2020 Solvent Engineered Synthesis of Layered SnO Nanoparticles for High-Performance Anodes
[36] Blank B, Kirchartz T, Lany S and Rau U 2017 Selection metric for photovoltaic materials screening based on detailed-balance analysis *Phys. Rev. Appl.* **8** 24032
[37] Davies D W *et al* 2020 Descriptors for electron and hole charge carriers in metal oxides *J. Phys. Chem. Lett.* **11** 438–44
[38] Butler K T, Davies D W and Walsh A 2018 Computational design of photovoltaic materials *Computational Materials Discovery* ed A R Oganov *et al* (London, UK: Royal Society of Chemistry) pp 176–97
[39] Davies D *et al* 2019 SMACT: semiconducting materials by analogy and chemical theory *J. Open Source Softw.* **4** 1361
[40] Shockley W and Queisser H J 1961 Detailed balance limit of efficiency of p-n junction solar cells *J. Appl. Phys.* **32** 510–9
[41] Yu L and Zunger A 2012 Identification of potential photovoltaic absorbers based on first-principles spectroscopic screening of materials *Phys. Rev. Lett.* **108** 68701
[42] Savory C N, Walsh A and Scanlon D O 2016 Can Pb-free halide double perovskites support high-efficiency solar cells? *ACS Energy Lett.* **1** 949–55
[43] Yu L, Kokenyesi R S, Keszler D A and Zunger A 2013 Inverse design of high absorption thin-film photovoltaic materials *Adv. Energy Mater.* **3** 43–8
[44] Kim S *et al* 2020 Upper limit to the photovoltaic efficiency of imperfect crystals from first principles *Energy Environ. Sci.* **13** 1481–91
[45] Mitzi D B, Gunawan O, Todorov T K, Wang K and Guha S 2011 The path towards a high-performance solution-processed kesterite solar cell *Sol. Energy Mater. Sol. Cells* **95** 1421–36
[46] Yan C *et al* 2018 Cu_2ZnSnS_4 solar cells with over 10% power conversion efficiency enabled by heterojunction heat treatment *Nat. Energy* **3** 764–72
[47] Rau U, Blank B, Müller T C M and Kirchartz T 2017 Efficiency potential of photovoltaic materials and devices unveiled by detailed-balance analysis *Phys. Rev. Appl.* **7** 44016
[48] Green M A 2012 Radiative efficiency of state-of-the-art photovoltaic cells *Prog. Photovolt. Res. Appl.* **20** 472–6
[49] Nayak P K, Mahesh S, Snaith H J and Cahen D 2019 Photovoltaic solar cell technologies: analysing the state of the art *Nat. Rev. Mater.* **4** 269
[50] Walsh A and Zunger A 2017 Instilling defect tolerance in new compounds *Nat. Mater.* **16** 964–7
[51] Shockley W and Read W T 1952 Statistics of the recombinations of holes and electrons *Phys. Rev.* **87** 835–42
[52] Alkauskas A, McCluskey M D and Van deWalle C G 2016 Tutorial: defects in semiconductors—combining experiment and theory *J. Appl. Phys.* **119** 181101
[53] Das B, Aguilera I, Rau U and Kirchartz T 2020 What is a deep defect? Combining Shockley–Read–Hall statistics with multiphonon recombination theory *Phys. Rev. Mater.* **4** 14
[54] Zhang S B, Wei S-H, Zunger A and Katayama-Yoshida H 1998 Defect physics of the $CuInSe_2$ chalcopyrite semiconductor *Phys. Rev.* B **57** 9642–56
[55] Zakutayev A *et al* 2014 Defect tolerant semiconductors for solar energy conversion *J. Phys. Chem. Lett.* **5** 1117–25
[56] Giorgi G and Yamashita K 2017 *Theoretical Modeling of Organohalide Perovskites for Photovoltaic Applications* (Boca Raton, FL: CRC Press)
[57] DasSarma S and Madhukar A 1981 Study of the ideal-vacancy-induced neutral deep levels in III-V compound semiconductors and their ternary alloys *Phys. Rev.* B **24** 2051–68
[58] Shi H and Du M-H 2014 Shallow halogen vacancies in halide optoelectronic materials *Phys. Rev.* B **90** 174103
[59] Shi H, Ming W and Du M-H 2016 Bismuth chalcohalides and oxyhalides as optoelectronic materials *Phys. Rev.* B **93** 104108
[60] Kim J, Chung C-H and Hong K-H 2016 Understanding of the formation of shallow level defects from the intrinsic defects of lead tri-halide perovskites *Phys. Chem. Chem. Phys.* **18** 27143–7
[61] Kurchin R C, Gorai P, Buonassisi T and Stevanović V 2018 Structural and chemical features giving rise to defect tolerance of binary semiconductors *Chem. Mater.* **30** 5583–92
[62] Maughan A E *et al* 2016 Defect tolerance to intolerance in the vacancy-ordered double perovskite semiconductors Cs_2SnI_6 and Cs_2TeI_6 *J. Am. Chem. Soc.* **138** 8453–64
[63] Kim J, Lee S-H, Lee J H and Hong K-H 2014 The role of intrinsic defects in methylammonium lead iodide perovskite *J. Phys. Chem. Lett.* **5** 1312–7
[64] Kim S, Park J-S, Hood S N and Walsh A 2019 Lone-pair effect on carrier capture in Cu_2ZnSnS_4 solar cells *J. Mater. Chem.* A **7** 2686–93
[65] Landsberg P T 1992 *Recombination in semiconductors* (Cambridge, UK: Cambridge University Press)
[66] Walsh A, Sokol A A, Buckeridge J, Scanlon D O and Catlow C R A 2018 Oxidation states and ionicity *Nat. Mater.* **17** 958–64
[67] Yang J H, Yin W J, Park J S, Ma J and Wei S H 2016 Review on first-principles study of defect properties of CdTe as a solar cell absorber *Semicond. Sci. Technol.* **31** 83002
[68] Steirer K X *et al* 2016 Defect tolerance in methylammonium lead triiodide perovskite *ACS Energy Lett.* **1** 360–6
[69] Alkauskas A, Dreyer C E, Lyons J L and Van deWalle C G 2016 Role of excited states in Shockley–Read–Hall recombination in wide-band-gap semiconductors *Phys. Rev.* B **93** 201304
[70] Zhang X, Turiansky M E and Van deWalle C G 2020 Correctly assessing defect tolerance in halide perovskites *J. Phys. Chem.* C **124** 6022–7
[71] Xiao Z, Meng W, Wang J, Mitzi D B and Yan Y 2017 Searching for promising new perovskite-based photovoltaic absorbers: the importance of electronic dimensionality *Mater. Horizons* **4** 206–16
[72] Brandt R E, Stevanović V, Ginley D S and Buonassisi T 2015 Identifying defect-tolerant semiconductors with high minority-carrier lifetimes: beyond hybrid lead halide perovskites *MRS Commun.* **5** 265–75

[73] Whalley L D, Frost J M, Jung Y-K and Walsh A 2017 Perspective: theory and simulation of hybrid halide perovskites *J. Chem. Phys.* **146** 220901

[74] Pyykkö P 1988 Relativistic effects in structural chemistry *Chem. Rev.* **88** 563–94

[75] Li Z, Kavanagh S R *et al* 2020 Bandgap lowering in mixed alloys of $Cs_2Ag(Sb_xBi_{1-x})Br_6$ double perovskite thin films *J. Mater. Chem.* A **8** 21780–8

[76] García-Espejo G, Rodríguez-Padrón D, Luque R, Camacho L and DeMiguel G 2019 Mechanochemical synthesis of three double perovskites: $Cs_2AgBiBr_6$, $(CH_3NH_3)_2TlBiBr_6$ and $Cs_2AgSbBr_6$ *Nanoscale* **11** 16650–7

[77] Kim S and Walsh A 2020 Comment on 'Low-frequency lattice phonons in halide perovskites explain high defect tolerance toward electron–hole recombination' arXiv:2003.05394 [cond-mat]

[78] Chu W, Zheng Q, Prezhdo O V, Zhao J and Saidi W A 2020 Response to Comment on 'Low-frequency lattice phonons in halide perovskites explain high defect tolerance toward electron–hole recombination' *Sci. Adv.* **6** eaaw7453

[79] Yin W-J, Shi T and Yan Y 2014 Unusual defect physics in $CH_3NH_3PbI_3$ perovskite solar cell absorber *Appl. Phys. Lett.* **104** 63903

[80] Green M A, Ho-Baillie A and Snaith H J 2014 The emergence of perovskite solar cells *Nat. Photonics* **8** 506–14

[81] Berry J *et al* 2015 Hybrid organic–inorganic perovskites (HOIPs): opportunities and challenges *Adv. Mater.* **27** 5102–12

[82] Kirchartz T, Markvart T, Rau U and Egger D A 2018 Impact of small phonon energies on the charge-carrier lifetimes in metal-halide perovskites *J. Phys. Chem. Lett.* **9** 939–46

[83] Dereń P J, Bednarkiewicz A, Goldner P and Guillot-Noël O 2008 Laser action in $LaAlO_3:Nd^{3+}$ single crystal *J. Appl. Phys.* **103** 43102

[84] Yang W S *et al* 2017 Iodide management in formamidinium-lead-halide-based perovskite layers for efficient solar cells *Science* **356** 1376–9

[85] Kuganathan N and Islam M S 2009 Li_2MnSiO_4 lithium battery material: atomic-scale study of defects, lithium mobility, and trivalent dopants *Chem. Mater.* **21** 5196–202

[86] Freysoldt C *et al* 2014 First-principles calculations for point defects in solids *Rev. Mod. Phys.* **86** 253–305

[87] Kim S, Hood S N, Park J-S, Whalley L D and Walsh A 2020 Quick-start guide for first-principles modelling of point defects in crystalline materials *J Phys Energy* **2** 036001

[88] Kohn W and Sham L J 1965 Self-consistent equations including exchange and correlation effects *Phys. Rev.* **140** A1133–8

[89] Hohenberg P and Kohn W 1964 Inhomogeneous electron gas *Phys. Rev.* **136** B864–71

[90] Goyal A, Gorai P, Peng H, Lany S and Stevanović V 2017 A computational framework for automation of point defect calculations *Comput. Mater. Sci.* **130** 1–9

[91] Kavanagh S 2020 kavanase (Seán Kavanagh) - GitHub GitHub.com/kavanase

[92] Broberg D *et al* 2018 PyCDT: a python toolkit for modeling point defects in semiconductors and insulators *Comput. Phys. Commun.* **226** 165–79

[93] Naik M H and Jain M 2018 CoFFEE: corrections for formation energy and eigenvalues for charged defect simulations *Comput. Phys. Commun.* **226** 114–26

[94] Freysoldt C, Neugebauer J and Van deWalle C G 2009 Fully *ab initio* finite-size corrections for charged-defect supercell calculations *Phys. Rev. Lett.* **102** 16402

[95] Kim S, Hood S N, vanGerwen P, Whalley L D and Walsh A 2020 CarrierCapture.jl: anharmonic carrier capture (doi:10.5281/zenodo.3707592)

[96] Buckeridge J, Scanlon D O, Walsh A and Catlow C R A 2014 Automated procedure to determine the thermodynamic stability of a material and the range of chemical potentials necessary for its formation relative to competing phases and compounds *Comput. Phys. Commun.* **185** 330–8

[97] Buckeridge J 2019 Equilibrium point defect and charge carrier concentrations in a material determined through calculation of the self-consistent Fermi energy *Comput. Phys. Commun.* **244** 329–42

[98] Pizzi G, Cepellotti A, Sabatini R, Marzari N and Kozinsky B 2016 AiiDA: automated interactive infrastructure and database for computational science *Comput. Mater. Sci.* **111** 218–30

[99] Jain A *et al* 2015 FireWorks: a dynamic workflow system designed for high-throughput applications *Concurr. Comput. Pract. Exp.* **27** 5037–59

[100] Kim S, Hood S N and Walsh A 2019 Anharmonic lattice relaxation during nonradiative carrier capture *Phys. Rev.* B **100** 41202

[101] Alkauskas A, Yan Q and Van DeWalle C G 2014 First-principles theory of nonradiative carrier capture via multiphonon emission *Phys. Rev.* B **90** 75202

[102] Zhao Y and Zhu K 2016 Organic-inorganic hybrid lead halide perovskites for optoelectronic and electronic applications *Chem. Soc. Rev.* **45** 655–89

[103] Travis W, Glover E N K, Bronstein H, Scanlon D O and Palgrave R G 2016 On the application of the tolerance factor to inorganic and hybrid halide perovskites: a revised system *Chem. Sci.* **7** 4548–56

[104] Becker M, Klüner T and Wark M 2017 Formation of hybrid ABX_3 perovskite compounds for solar cell application: first-principles calculations of effective ionic radii and determination of tolerance factors *Dalton Trans.* **46** 3500–9

[105] Sun Y, Peng J, Chen Y, Yao Y and Liang Z 2017 Triple-cation mixed-halide perovskites: towards efficient, annealing-free and air-stable solar cells enabled by Pb $(SCN)_2$ additive *Sci. Rep.* **7** 46193

[106] Dufton J T R R *et al* 2012 Structural and electronic properties of $CuSbS_2$ and $CuBiS_2$: potential absorber materials for thin-film solar cells *Phys. Chem. Chem. Phys.* **14** 7229–33

[107] Dunlap-Shohl W A, Hill I G, Yan Y and Mitzi D B 2018 Photovoltaic effect in Indium (I) iodide thin films *Chem. Mater.* **30** 8226–32

[108] Bennett J W, Grinberg I and Rappe A M 2009 Effect of substituting of S for O: the sulfide perovskite $BaZrS_3$ investigated with density functional theory *Phys. Rev.* B **79** 235115

[109] Eya H I, Ntsoenzok E and Dzade N Y 2020 First-principles investigation of the structural, elastic, electronic, and optical properties of α- and β-$SrZrS_3$: implications for photovoltaic applications *Materials* **13** 978

[110] Stoumpos C C, Malliakas C D and Kanatzidis M G 2013 Semiconducting tin and lead iodide perovskites with organic cations: phase transitions, high mobilities, and near-infrared photoluminescent properties *Inorg. Chem.* **52** 9019–38

[111] Ma L *et al* 2016 Carrier diffusion lengths of over 500 nm in lead-free perovskite $CH_3NH_3SnI_3$ films *J. Am. Chem. Soc.* **138** 14750–5

[112] Li Q *et al* 2019 Hexagonal $MASnI_3$ exhibiting strong absorption of ultraviolet photons *Appl. Phys. Lett.* **114** 101906

[113] Ke W *et al* 2017 Efficient lead-free solar cells based on hollow {en}$MASnI_3$ perovskites *J. Am. Chem. Soc.* **139** 14800–6

[114] Takahashi Y Y, Hasegawa H, Takahashi Y Y and Inabe T 2013 Hall mobility in tin iodide perovskite $CH_3NH_3SnI_3$: Evidence for a doped semiconductor *J. Solid State Chem.* **205** 39–43

[115] Peng L and Xie W 2020 Theoretical and experimental investigations on the bulk photovoltaic effect in lead-free perovskites $MASnI_3$ and $FASnI_3$ *RSC Adv.* **10** 14679–88

[116] Noel N K *et al* 2014 Lead-free organic–inorganic tin halide perovskites for photovoltaic applications *Energy Environ. Sci.* **7** 3061–8

[117] Milot R L *et al* 2018 The effects of doping density and temperature on the optoelectronic properties of formamidinium tin triiodide thin films *Adv. Mater.* **30** 1804506

[118] Ran C *et al* 2019 Conjugated organic cations enable efficient self-healing $FASnI_3$ solar cells *Joule* **3** 3072–87

[119] Jiang X *et al* 2020 Ultra-high open-circuit voltage of tin perovskite solar cells via an electron transporting layer design *Nat. Commun.* **11** 1–7

[120] Huang L Y and Lambrecht W R L L 2013 Electronic band structure, phonons, and exciton binding energies of halide perovskites $CsSnCl_3$, $CsSnBr_3$, and $CsSnI_3$ *Phys. Rev.* B **88** 165203

[121] Marshall K P, Walker M, Walton R I and Hatton R A 2016 Enhanced stability and efficiency in hole-transport-layer-free $CsSnI_3$ perovskite photovoltaics *Nat. Energy* **1** 16178

[122] Chung I *et al* 2012 $CsSnI_3$: semiconductor or metal? High electrical conductivity and strong near-infrared photoluminescence from a single material. High hole mobility and phase-transitions *J. Am. Chem. Soc.* **134** 8579–87

[123] Wu B *et al* 2017 Long minority-carrier diffusion length and low surface-recombination velocity in inorganic lead-free $CsSnI_3$ perovskite crystal for solar cells *Adv. Funct. Mater.* **27** 1604818

[124] Luo J *et al* 2018 Efficient and stable emission of warm-white light from lead-free halide double perovskites *Nature* **563** 541–5

[125] DaSilva E L, Skelton J M, Parker S C and Walsh A 2015 Phase stability and transformations in the halide perovskite $CsSnI_3$ *Phys. Rev.* B **91** 144107

[126] Kopacic I *et al* 2018 Enhanced performance of germanium halide perovskite solar cells through compositional engineering *ACS Appl. Energy Mater.* **1** 343–7

[127] Lu X *et al* 2016 First-principles insight into the photoelectronic properties of Ge-based perovskites *RSC Adv.* **6** 86976–81

[128] Krishnamoorthy T *et al* 2015 Lead-free germanium iodide perovskite materials for photovoltaic applications *J. Mater. Chem.* A **3** 23829–32

[129] Zhou J *et al* 2017 Composition design, optical gap and stability investigations of lead-free halide double perovskite $Cs_2AgInCl_6$ *J. Mater. Chem.* A **5** 15031–7

[130] McClure E T, Ball M R, Windl W and Woodward P M 2016 Cs_2AgBiX_6 (X = Br, Cl): new visible light absorbing, lead-free halide perovskite semiconductors *Chem. Mater.* **28** 1348–54

[131] Gao W *et al* 2018 High-quality $Cs_2AgBiBr_6$ double perovskite film for lead-free inverted planar heterojunction solar cells with 2.2% efficiency *ChemPhysChem* **19** 1696–700

[132] Filip M R, Hillman S, Haghighirad A A, Snaith H J and Giustino F 2016 Band gaps of the lead-free halide double perovskites $Cs_2BiAgCl_6$ and $Cs_2BiAgBr_6$ from theory and experiment *J. Phys. Chem. Lett.* **7** 2579–85

[133] Hoye R L Z Z *et al* 2018 Fundamental carrier lifetime exceeding 1 μs in $Cs_2AgBiBr_6$ double perovskite *Adv. Mater. Interfaces* **5** 2–9

[134] Bartesaghi D *et al* 2018 Charge carrier dynamics in $Cs_2AgBiBr_6$ double perovskite *J. Phys. Chem.* C **122** 4809–16

[135] Pan W *et al* 2017 $Cs_2AgBiBr_6$ single-crystal x-ray detectors with a low detection limit *Nat. Photonics* **11** 726–32

[136] Yang X *et al* 2020 Simultaneous power conversion efficiency and stability enhancement of $Cs_2AgBiBr_6$ lead-free inorganic perovskite solar cell through adopting a multifunctional dye interlayer *Adv. Funct. Mater.* **30** 2001557

[137] Slavney A H *et al* 2017 Defect-induced band-edge reconstruction of a bismuth-halide double perovskite for visible-light absorption *J. Am. Chem. Soc.* **139** 5015–8

[138] Zhang C *et al* 2018 Design of a novel and highly stable lead-free Cs_2NaBiI_6 double perovskite for photovoltaic application *Sustain. Energy Fuels* **2** 2419–28

[139] Zhao S, Yamamoto K, Iikubo S, Hayase S and Ma T 2018 First-principles study of electronic and optical properties of lead-free double perovskites Cs_2NaBX_6 (B = Sb, Bi; X = Cl, Br, I) *J. Phys. Chem. Solids* **117** 117–21

[140] Volonakis G *et al* 2017 $Cs_2InAgCl_6$: a new lead-free halide double perovskite with direct band gap *J. Phys. Chem. Lett.* **8** 772–8

[141] Cheng P *et al* 2017 Combining theory and experiment in the design of a lead-free $((CH_3NH_3)_2AgBiI_6)$ double perovskite *New J. Chem.* **41** 9598–601

[142] Wei F *et al* 2017 Synthesis and properties of a lead-free hybrid double perovskite:$(CH_3NH_3)_2AgBiBr_6$ *Chem. Mater.* **29** 1089–94

[143] Meyer E, Mutukwa D, Zingwe N and Taziwa R 2018 Lead-free halide double perovskites: a review of the structural, optical, and stability properties as well as their viability to replace lead halide perovskites *Metals* **8** 667

[144] Park B W *et al* 2015 Bismuth based hybrid perovskites $A_3Bi_2I_9$ (a: methylammonium or cesium) for solar cell application *Adv. Mater.* **27** 6806–13

[145] Hoye R L Z *et al* 2016 Methylammonium bismuth iodide as a lead-free, stable hybrid organic–inorganic solar absorber *Chem. Eur. J.* **22** 2605–10

[146] Kim S-Y Y *et al* 2019 Wide range tuning of band gap energy of $A_3B_2X_9$ perovskite-like halides *Scr. Mater.* **166** 107–11

[147] Zheng X *et al* 2020 Ultrasensitive and stable x-ray detection using zero-dimensional lead-free perovskites *J. Energy Chem.* **49** 299–306

[148] Jain S M *et al* 2018 An effective approach of vapour assisted morphological tailoring for reducing metal defect sites in lead-free, $(CH_3NH_3)_3Bi_2I_9$ bismuth-based perovskite solar cells for improved performance and long-term *Nano Energy* **49** 614–24

[149] Pazoki M *et al* 2016 Bismuth iodide perovskite materials for solar cell applications: electronic structure, optical transitions, and directional charge transport *J. Phys. Chem.* C **120** 29039–46

[150] Szklarz P *et al* 2019 Lead-free hybrid ferroelectric material based on formamidine:$[NH_2CHNH_2]_3Bi_2I_9$ *J. Mater. Chem.* C **7** 3003–14

[151] Bai F *et al* 2018 Lead-free, air-stable ultrathin $Cs_3Bi_2I_9$ perovskite nanosheets for solar cells *Sol. Energy Mater. Sol. Cells* **184** 15–21

[152] Lehner A J *et al* 2015 Crystal and electronic structures of complex bismuth iodides $A_3Bi_2I_9$ (A = K, Rb, Cs) related to perovskite: aiding the rational design of photovoltaics *Chem. Mater.* **27** 7137–48

[153] Li W G, Wang X D, Liao J F, Jiang Y and Kuang D B 2020 Enhanced on–off ratio photodetectors based on lead-free $Cs_3Bi_2I_9$ single crystal thin films *Adv. Funct. Mater.* **30** 1909701

[154] Sun S *et al* 2016 Synthesis, crystal structure, and properties of a perovskite-related bismuth phase, $(NH_4)_3Bi_2I_9$ *APL Mater.* **4** 031101

[155] Zhuang R *et al* 2019 Highly sensitive x-ray detector made of layered perovskite-like $(NH_4)_3Bi_2I_9$ single crystal with anisotropic response *Nat. Photonics* **13** 602–8

[156] Singh A *et al* 2018 Photovoltaic performance of vapor-assisted solution-processed layer polymorph of $Cs_3Sb_2I_9$ *ACS Appl. Mater. Interfaces* **10** 2566–73

[157] Umar F *et al* 2019 Dimensionality controlling of $Cs_3Sb_2I_9$ for efficient all-inorganic planar thin film solar cells by HCl-assisted solution method *Adv. Opt. Mater.* **7** 1801368

[158] Chonamada T D, Dey A B and Santra P K 2019 Degradation studies of $Cs_3Sb_2I_9$: a lead-free perovskite *ACS Appl. Energy Mater.* **3** 47–55

[159] Yang B *et al* 2018 Constructing sensitive and fast lead-free single-crystalline perovskite photodetectors *J. Phys. Chem. Lett.* **9** 3087–92

[160] Ju D *et al* 2018 Narrow band gap and high mobility of lead-free perovskite single crystal Sn-doped $MA_3Sb_2I_9$ *J. Mater. Chem.* A **6** 20753–9

[161] Li F, Wang Y, Xia K, Hoye R L Z and Pecunia V 2020 Microstructural and photoconversion efficiency enhancement of compact films of lead-free perovskite derivative $Rb_3Sb_2I_9$ *J. Mater. Chem.* A **8** 4396–406

[162] Hebig J-C, Kühn I, Flohre J and Kirchartz T 2016 Optoelectronic properties of $(CH_3NH_3)_3Sb_2I_9$ thin films for photovoltaic applications *ACS Energy Lett.* **1** 309–14

[163] Harikesh P C *et al* 2016 Rb as an alternative cation for templating inorganic lead-free perovskites for solution processed photovoltaics *Chem. Mater.* **28** 7496–504

[164] Johnston A *et al* 2020 Narrow emission from $Rb_3Sb_2I_9$ nanoparticles *Adv. Opt. Mater.* **8** 1901606

[165] Weber S *et al* 2018 Influence of the iodide to bromide ratio on crystallographic and optoelectronic properties of rubidium antimony halide perovskites *ACS Appl. Energy Mater.* **2** 539–47

[166] Zumeta-Dube I, Ruiz-Ruiz V–F, Diaz D, Rodil-Posadas S and Zeinert A 2014 TiO_2 sensitization with Bi_2S_3 quantum dots: the inconvenience of sodium ions in the deposition procedure *J. Phys. Chem.* C **118** 11495–504

[167] Patterson R J *et al* 2017 Oxygen substitution and sulfur vacancies in $NaBiS_2$: a Pb-free candidate for solution processable solar cells *2017 IEEE 44th Photovoltaic Specialist Conf. (PVSC)* (Piscataway, NJ: IEEE) pp 2392–4

[168] Medina-Gonzalez A M, Rosales B A, Hamdeh U H, Panthani M G and Vela J 2020 Surface chemistry of ternary nanocrystals: engineering the deposition of conductive $NaBiS_2$ films *Chem. Mater.* **32** 6085–96

[169] Xia Z *et al* 2017 Synthesis and characterization of $NaSbS_2$ thin film for potential photodetector and photovoltaic application *Chin. Chem. Lett.* **28** 881–7

[170] Rahayu S U *et al* 2016 Sodium antimony sulfide ($NaSbS_2$): turning an unexpected impurity into a promising, environmentally friendly novel solar absorber material *APL Mater.* **4** 116103

[171] Leung W W W, Savory C N, Palgrave R G and Scanlon D O 2019 An experimental and theoretical study into $NaSbS_2$ as an emerging solar absorber *J. Mater. Chem.* C **7** 2059–67

[172] Huang P C, Yang W C and Lee M W 2013 $AgBiS_2$ semiconductor-sensitized solar cells *J. Phys. Chem.* C **117** 18308–14

[173] Diedenhofen S L, Bernechea M, Felter K M, Grozema F C and Siebbeles L D A 2019 Charge photogeneration and transport in $AgBiS_2$ nanocrystal films for photovoltaics *Sol. RRL* **3** 1900075

[174] Pejova B, Nesheva D, Aneva Z and Petrova A 2011 Photoconductivity and relaxation dynamics in sonochemically synthesized assemblies of $AgBiS_2$ quantum dots *J. Phys. Chem.* C **115** 37–46

[175] Öberg V A, Johansson M B, Zhang X and Johansson E M J 2020 Cubic $AgBiS_2$ colloidal nanocrystals for solar cells *ACS Appl. Nano Mater.* **3** 4014–24

[176] Balci G K and Ayhan S 2018 *Ab-initio* calculations of structural, optical and electronic properties of $AgBiS_2$ *Int. Adv. Res. Eng. J.* **2** 1–8

[177] Burgués-Ceballos I, Wang Y, Akgul M Z and Konstantatos G 2020 Colloidal $AgBiS_2$ nanocrystals with reduced recombination yield 6.4% power conversion efficiency in solution-processed solar cells *Nano Energy* **75** 104961

[178] Septina W, Ikeda S, Iga Y, Harada T and Matsumura M 2014 Thin film solar cell based on $CuSbS_2$ absorber fabricated from an electrochemically deposited metal stack *Thin Solid Films* **550** 700–4

[179] Banu S, Ahn S J, Ahn S K, Yoon K and Cho A 2016 Fabrication and characterization of cost-efficient $CuSbS_2$ thin film solar cells using hybrid inks *Sol. Energy Mater. Sol. Cells* **151** 14–23

[180] Colombara D, Peter L M, Rogers K D, Painter J D and Roncallo S 2011 Formation of $CuSbS_2$ and $CuSbSe_2$ thin films via chalcogenisation of Sb–Cu metal precursors *Thin Solid Films* **519** 7438–43

[181] McCarthy C L *et al* 2016 Earth abundant $CuSbS_2$ thin films solution processed from thiol—amine mixtures *J. Mater. Chem.* C **4** 6230–3

[182] deSouza Lucas F W *et al* 2016 Effects of thermochemical treatment on $CuSbS_2$ photovoltaic absorber quality and solar cell reproducibility *J. Phys. Chem.* C **120** 18377–85

[183] Gassoumi A, Alfaify S, Nasr T B and Bouarissa N 2017 The investigation of crystal structure, elastic and optoelectronic properties of $CuSbS_2$ and $CuBiS_2$ compounds for photovoltaic applications *J. Alloys Compd.* **725** 181–9

[184] Welch A W *et al* 2015 $CuSbSe_2$ photovoltaic devices with 3% efficiency *Appl. Phys. Express* **8** 082301

[185] Yang B *et al* 2017 Hydrazine solution processed $CuSbSe_2$: temperature dependent phase and crystal orientation evolution *Sol. Energy Mater. Sol. Cells* **168** 112–8

[186] Welch A W *et al* 2017 Trade-offs in thin film solar cells with layered chalcostibite photovoltaic absorbers *Adv. Energy Mater.* **7** 1601935

[187] Zhang D *et al* 2016 Ternary $CuSbSe_2$ chalcostibite: facile synthesis, electronic-structure and thermoelectric performance enhancement *J. Mater. Chem.* A **4** 4188–93

[188] Xue D J *et al* 2015 $CuSbSe_2$ as a potential photovoltaic absorber material: studies from theory to experiment *Adv. Energy Mater.* **5** 1501203

[189] Bu K *et al* 2018 Observation of high seebeck coefficient and low thermal conductivity in [SrO]-intercalated $CuSbSe_2$ compound *Chem. Mater.* **30** 5539–43

[190] Temple D J, Kehoe A B, Allen J P, Watson G W and Scanlon D O 2012 Geometry, electronic structure, and bonding in $CuMCh_2$ (M = Sb, Bi; Ch = S, Se): alternative solar cell absorber materials? *J. Phys. Chem.* C **116** 7334–40

[191] Ohno N, Yoshida M, Nakamura K and Nakai Y 1980 Photoluminescence of indium iodide *Solid State Commun.* **35** 775–9

[192] Liu P *et al* 2017 Electronic structures and band alignments of monolayer metal trihalide semiconductors MX_3 *J. Mater. Chem.* C **5** 9066–71

[193] Xiao M *et al* 2020 Symmetry-reduction enhanced polarization-sensitive photodetection in core–shell SbI_3/Sb_2O_3 van der Waals heterostructure *Small* **16** 1907172

[194] Brandt R E *et al* 2015 Investigation of bismuth triiodide (BiI_3) for photovoltaic applications *J. Phys. Chem. Lett.* **6** 4297–302

[195] Lintereur A T, Qiu W, Nino J C and Baciak J 2011 Characterization of bismuth tri-iodide single crystals for wide band-gap semiconductor radiation detectors *Nucl. Instrum. Methods Phys. Res.* A **652** 166–9

[196] Tiwari D, Alibhai D and Fermin D J 2018 Above 600 mV open-circuit voltage BiI_3 solar cells *ACS Energy Lett.* **3** 1882–6

[197] K\kepińska M, Nowak M, Duka P, Kotyczka-Morańska M and Szperlich P 2011 Optical properties of SbI_3 single crystalline platelets *Opt. Mater.* **33** 1753–9

[198] Trotter J and Zobel T 1966 The crystal structure of SbI_3 and BiI_3 *Z. Krist. Mater.* **123** 67–72

[199] Zeng W *et al* 2019 Synthesis of large-area atomically thin BiOI crystals with highly sensitive and controllable photodetection *Adv. Funct. Mater.* **29** 1900129

[200] Dai W-W and Zhao Z-Y 2016 Electronic structure and optical properties of BiOI as a photocatalyst driven by visible light *Catalysts* **6** 133

[201] Hoye R L Z *et al* 2017 Strongly enhanced photovoltaic performance and defect physics of air-stable bismuth oxyiodide (BiOI) *Adv. Mater.* **29** 1702176

[202] Tiwari D, Cardoso-Delgado F, Alibhai D, Mombrú M and Fermín D J 2019 Photovoltaic performance of phase-pure orthorhombic BiSI thin-films *ACS Appl. Energy Mater.* **2** 3878–85

[203] Sasaki Y 1965 Photoconductivity of a ferroelectric photoconductor BiSI *Japan. J. Appl. Phys.* **4** 614

[204] Demartin F, Gramaccioli C M and Campostrini I 2010 Demicheleite-(I), BiSI, a new mineral from La Fossa Crater, Vulcano, Aeolian Islands, Italy *Mineral. Mag.* **74** 141–5

[205] Nie R and Seok S I L 2020 Efficient antimony-based solar cells by enhanced charge transfer *Small Methods* **4** 1900698

[206] Choi Y C, Hwang E and Kim D-H 2018 Controlled growth of SbSI thin films from amorphous Sb_2S_3 for low-temperature solution processed chalcohalide solar cells *APL Mater.* **6** 121108

[207] Grigas J, Talik E and Lazauskas V 2003 Splitting of the XPS in ferroelectric SbSI crystals *Ferroelectrics* **284** 147–60

[208] Wei X *et al* 2020 Realization of $BaZrS_3$ chalcogenide perovskite thin films for optoelectronics *Nano Energy* **68** 104317

[209] Kuhar K *et al* 2017 Sulfide perovskites for solar energy conversion applications: computational screening and synthesis of the selected compound $LaYS_3$ *Energy Environ. Sci.* **10** 2579–93

[210] Niu S *et al* 2017 Bandgap control via structural and chemical tuning of transition metal perovskite chalcogenides *Adv. Mater.* **29** 16–21

[211] Lee C-S, Kleinke K M and Kleinke H 2005 Synthesis, structure, and electronic and physical properties of the two $SrZrS_3$ modifications *Solid State Sci.* **7** 1049–54

[212] Crovetto A *et al* 2019 Shining light on sulfide perovskites: $LaYS_3$ material properties and solar cells *Chem. Mater.* **31** 3359–69

[213] Nasti G and Abate A 2020 Tin halide perovskite ($ASnX_3$) solar cells: a comprehensive guide toward the highest power conversion efficiency *Adv. Energy Mater.* **10** 1902467

[214] Hao F *et al* 2015 Solvent-mediated crystallization of $CH_3NH_3SnI_3$ films for heterojunction depleted perovskite solar cells *J. Am. Chem. Soc.* **137** 11445–52

[215] Hao F, Stoumpos C C, Cao D H, Chang R P H H and Kanatzidis M G 2014 Lead-free solid-state organic-inorganic halide perovskite solar cells *Nat. Photonics* **8** 489–94

[216] Jeon N J *et al* 2014 Solvent engineering for high-performance inorganic-organic hybrid perovskite solar cells *Nat. Mater.* **13** 897–903

[217] Yang M *et al* 2017 Perovskite ink with wide processing window for scalable high-efficiency solar cells *Nat. Energy* **2** 17038

[218] Chen Q *et al* 2014 Planar heterojunction perovskite solar cells via vapor-assisted solution process *J. Am. Chem. Soc.* **136** 622–5

[219] Ke W *et al* 2015 Efficient fully-vacuum-processed perovskite solar cells using copper phthalocyanine as hole selective layers *J. Mater. Chem.* A **3** 23888–94

[220] Yu Y *et al* 2016 Thermally evaporated methylammonium tin triiodide thin films for lead-free perovskite solar cell fabrication *RSC Adv.* **6** 90248–54

[221] Yokoyama T *et al* 2016 Overcoming short-circuit in lead-free $CH_3NH_3SnI_3$ perovskite solar cells via kinetically controlled gas-solid reaction film fabrication process *J. Phys. Chem. Lett.* **7** 776–82

[222] Kumar M H *et al* 2014 Lead-free halide perovskite solar cells with high photocurrents realized through vacancy modulation *Adv. Mater.* **26** 7122–7

[223] Gupta S, Bendikov T, Hodes G and Cahen D 2016 $CsSnBr_3$, a lead-free halide perovskite for long-term solar cell application: insights on SnF_2 addition *ACS Energy Lett.* **1** 1028–33

[224] Shum K *et al* 2010 Synthesis and characterization of $CsSnI_3$ thin films *Appl. Phys. Lett.* **96** 221903

[225] Wang L *et al* 2017 Pressure-induced structural evolution, optical and electronic transitions of nontoxic organometal halide perovskite-based methylammonium tin chloride *Appl. Phys. Lett.* **111** 233901

[226] Li Y *et al* 2016 50% Sn-based planar perovskite solar cell with power conversion efficiency up to 13.6% *Adv. Energy Mater.* **6** 1601353

[227] Goyal A *et al* 2018 Origin of pronounced nonlinear band gap behavior in lead–tin hybrid perovskite alloys *Chem. Mater.* **30** 3920–8

[228] Parrott E S *et al* 2016 Effect of structural phase transition on charge-carrier lifetimes and defects in $CH_3NH_3SnI_3$ perovskite *J. Phys. Chem. Lett.* **7** 1321–6

[229] Ke W *et al* 2017 Enhanced photovoltaic performance and stability with a new type of hollow 3D perovskite {en}$FASnI_3$ *Sci. Adv.* **3** e1701293

[230] Bowman A R *et al* 2019 Microsecond carrier lifetimes, controlled p-doping, and enhanced air stability in low-bandgap metal halide perovskites *ACS Energy Lett.* **4** 2301–7

[231] Zhao B *et al* 2017 High open-circuit voltages in tin-rich low-bandgap perovskite-based planar heterojunction photovoltaics *Adv. Mater.* **29** 1604744

[232] Stoumpos C C *et al* 2015 Hybrid germanium iodide perovskite semiconductors: active lone pairs, structural distortions, direct and indirect energy gaps, and strong nonlinear optical properties *J. Am. Chem. Soc.* **137** 6804–19

[233] Pantaler M, Fettkenhauer C, Nguyen H L, Anusca I and Lupascu D C 2018 Deposition routes of $Cs_2AgBiBr_6$ double perovskites for photovoltaic applications *MRS Adv.* **3** 1819–23

[234] Zhou L, Xu Y F, Chen B X, Kuang D B and Su C Y 2018 Synthesis and photocatalytic application of stable lead-free $Cs_2AgBiBr_6$ perovskite nanocrystals *Small* **14** 1703762

[235] Creutz S E, Crites E N, DeSiena M C and Gamelin D R 2018 Colloidal nanocrystals of lead-free double-perovskite (elpasolite) semiconductors: synthesis and anion exchange to access new materials *Nano Lett.* **18** 1118–23

[236] Wu C *et al* 2018 The dawn of lead-free perovskite solar cell: highly stable double perovskite $Cs_2AgBiBr_6$ film *Adv. Sci.* **5** 2–9

[237] Slavney A H, Hu T, Lindenberg A M and Karunadasa H I 2016 A bismuth-halide double perovskite with long carrier recombination lifetime for photovoltaic applications *J. Am. Chem. Soc.* **138** 2138–41

[238] Volonakis G *et al* 2016 Lead-free halide double perovskites via heterovalent substitution of noble metals *J. Phys. Chem. Lett.* **7** 1254–9

[239] Greul E, Petrus M L, Binek A, Docampo P and Bein T 2017 Highly stable, phase pure $Cs_2AgBiBr_6$ double perovskite thin films for optoelectronic applications *J. Mater. Chem.* A **5** 19972–81

[240] Meng W *et al* 2017 Parity-forbidden transitions and their impact on the optical absorption properties of lead-free metal halide perovskites and double perovskites *J. Phys. Chem. Lett.* **8** 2999–3007

[241] Tran T T, Panella J R, Chamorro J R, Morey J R and McQueen T M 2017 Designing indirect-direct bandgap transitions in double perovskites *Mater. Horizons* **4** 688–93

[242] Giesecke J A, Michl B, Schindler F, Schubert M C and Warta W 2011 Spatially resolved carrier lifetime calibrated via quasi-steadystate photoluminescence *Energy Procedia* **8** 64–70

[243] Slavney A H *et al* 2017 Chemical approaches to addressing the instability and toxicity of lead-halide perovskite absorbers *Inorg. Chem.* **56** 46–55

[244] Xiao Z, Du K-Z, Meng W, Mitzi D B and Yan Y 2017 Chemical origin of the stability difference between copper (I)-and silver (I)-based halide double perovskites *Angew. Chem.* **129** 12275–9

[245] Xiao Z *et al* 2017 Intrinsic instability of $Cs_2In(I)M(III)X_6$ (M = Bi, Sb; X = halogen) double perovskites: a combined density functional theory and experimental study *J. Am. Chem. Soc.* **139** 6054–7

[246] Perera S *et al* 2016 Chalcogenide perovskites—an emerging class of ionic semiconductors *Nano Energy* **22** 129–35

[247] Meng W *et al* 2016 Alloying and defect control within chalcogenide perovskites for optimized photovoltaic application *Chem. Mater.* **28** 821–9

[248] Wei X *et al* 2020 Ti-alloying of $BaZrS_3$ chalcogenide perovskite for photovoltaics *ACS Omega* **5** 18579–83

[249] Herz L M 2017 Charge-carrier mobilities in metal halide perovskites: fundamental mechanisms and limits *ACS Energy Lett.* **2** 1539–48

[250] Peng Y *et al* 2020 Enhanced photoconversion efficiency in cesium-antimony-halide perovskite derivatives by tuning crystallographic dimensionality *Appl. Mater. Today* **19** 100637

[251] Saparov B *et al* 2015 Thin-film preparation and characterization of $Cs_3Sb_2I_9$: a lead-free layered perovskite semiconductor *Chem. Mater.* **27** 5622–32

[252] McCall K M, Stoumpos C C, Kostina S S, Kanatzidis M G and Wessels B W 2017 Strong electron–phonon coupling and self-trapped excitons in the defect halide perovskites $A_3M_2I_9$ (A = Cs, Rb; M = Bi, Sb) *Chem. Mater.* **29** 4129–45

[253] Hodgkins T L *et al* 2019 Anionic order and band gap engineering in vacancy ordered triple perovskites *Chem. Commun.* **55** 3164–7

[254] McCall K M *et al* 2019 From 0D $Cs_3Bi_2I_9$ to 2D $Cs_3Bi_2I_6Cl_3$: dimensional expansion induces a direct band gap but enhances electron—phonon coupling *Chem. Mater.* **31** 2644–50

[255] Yu B B *et al* 2019 Alloy-induced phase transition and enhanced photovoltaic performance: the case of $Cs_3Bi_2I_{9-x}Br_x$ perovskite solar cells *J. Mater. Chem.* A **7** 8818–25

[256] D'innocenzo V *et al* 2014 Excitons versus free charges in organo-lead tri-halide perovskites *Nat. Commun.* **5** 3586

[257] Saba M *et al* 2014 Correlated electron–hole plasma in organometal perovskites *Nat. Commun.* **5** 5049

[258] DeWolf S *et al* 2014 Organometallic halide perovskites: sharp optical absorption edge and its relation to photovoltaic performance *J. Phys. Chem. Lett.* **5** 1035–9

[259] Park Y, Mccarthy T J, Sutorlk A C, Kanatzidis M G and Gillan E G 1995 Synthesis of ternary chalcogenides in molten polychalcogenide salts: α-$KCuQ_4$, $KAuS_5$, $NaBiS_2$, $KFeQ_2$ (Q = S, Se) *Inorg. Synth. Nonmol. Solids* **30** 88–95 Synthesis of ternary chalcogenides in molten polychalcogenide salts: α-KCuQ4, KAuS5, NaBiS2, KFeQ2 (Q=S, Se)

[260] Kang S, Hong Y and Jeon Y 2014 A facile synthesis and characterization of sodium bismuth sulfide ($NaBiS_2$) under hydrothermal condition *Bull. Korean Chem. Soc.* **35** 1887–90

[261] Zhong T *et al* 2019 Sodium bismuth dichalcogenides: candidates for ferroelectric high-mobility semiconductors for multifunctional applications *Phys. Chem. Chem. Phys.* **21** 8553–8

[262] Sun W-C, Rahayu S U and Lee M-W 2018 Eco-friendly $NaSbS_2$ quantum dot-sensitized solar cells *IEEE J. Photovolt.* **8** 1011–6

[263] Pai N *et al* 2018 Spray deposition of $AgBiS_2$ and Cu_3BiS_3 thin films for photovoltaic applications *J. Mater. Chem.* C **6** 2483–94

[264] Bernechea M *et al* 2016 Solution-processed solar cells based on environmentally friendly $AgBiS_2$ nanocrystals *Nat. Photonics* **10** 521

[265] Pejova B, Grozdanov I, Nesheva D and Petrova A 2008 Size-dependent properties of sonochemically synthesized three-dimensional arrays of close-packed semiconducting $AgBiS_2$ quantum dots *Chem. Mater.* **20** 2551–65

[266] Akgul M Z, Figueroba A, Pradhan S, Bi Y and Konstantatos G 2020 Low-cost RoHS compliant solution processed photovoltaics enabled by ambient condition synthesis of $AgBiS_2$ nanocrystals *ACS Photonics* **7** 588–95

[267] Vines F, Bernechea M, Konstantatos G and Illas F 2016 Matildite versus schapbachite: first-principles investigation of the origin of photoactivity in $AgBiS_2$ *Phys. Rev.* B **94** 235203

[268] Ju M-G G, Dai J, Ma L, Zhou Y and Zeng X C 2020 $AgBiS_2$ as a low-cost and eco-friendly all-inorganic photovoltaic material: nanoscale morphology-property relationship *Nanoscale Adv.* **2** 770–6

[269] Wan L *et al* 2016 Two-stage co-evaporated $CuSbS_2$ thin films for solar cells *J. Alloys Compd.* **680** 182–90

[270] Chen W-L, Kuo D-H and Tuan T T A 2016 Preparation of $CuSbS_2$ thin films by Co-sputtering and solar cell devices with band gap-adjustable n-type InGaN as a substitute of ZnO *J. Electron. Mater.* **45** 688–94

[271] Nair M T S *et al* 2004 Absorber films of antimony chalcogenides via chemical deposition for photovoltaic application *MRS Online Proc. Libr. Arch.* **836** L5.37

[272] Rastogi A C and Janardhana N R 2014 Properties of $CuSbS_2$ thin films electrodeposited from ionic liquids as p-type absorber for photovoltaic solar cells *Thin Solid Films* **565** 285–92

[273] Riha S C, Koegel A A, Emery J D, Pellin M J and Martinson A B F 2017 Low-temperature atomic layer deposition of $CuSbS_2$ for thin-film photovoltaics *ACS Appl. Mater. Interfaces* **9** 4667–73

[274] Shi L, Li Y, Wu C and Dai Y 2015 Preparation, formation mechanism and photoelectric properties of well-aligned $CuSbS_2$ nanowires *J. Alloys Compd.* **648** 507–11

[275] Su H, Xie Y, Wan S, Li B and Qian Y 1999 A novel one-step solvothermal route to nanocrystalline $CuSbS_2$ and Ag_3SbS_3 *Solid State Ion.* **123** 319–24

[276] Ikeda S *et al* 2014 Selective production of $CuSbS_2$, Cu_3SbS_3, and Cu_3SbS_4 nanoparticles using a hot injection protocol *RSC Adv.* **4** 40969–72

[277] Yang B *et al* 2014 $CuSbS_2$ as a promising earth-abundant photovoltaic absorber material: a combined theoretical and experimental study *Chem. Mater.* **26** 3135–43

[278] Birkett M *et al* 2018 Band gap temperature-dependence and exciton-like state in copper antimony sulphide, $CuSbS_2$ *APL Mater.* **6** 84904

[279] Soliman L I, Elsoad A M A B O, Zayed H A and ElGhfar S A 2002 Structural and electrical properties of $CuSbTe_2$, $CuSbSe_2$ and $CuSbS_2$ chalcogenide this films *Fizika A* A **11** 139–52

[280] Tang D *et al* 2012 Growth and characterization of $CuSbSe_2$ thin films prepared by electrodeposition *Electrochim. Acta* **76** 480–6

[281] Hsiang H-I, Yang C-T and Tu J-H 2016 Characterization of $CuSbSe_2$ crystallites synthesized using a hot injection method *RSC Adv.* **6** 99297–305

[282] Tiwari K J, Vinod V, Subrahmanyam A and Malar P 2017 Growth and characterization of chalcostibite $CuSbSe_2$ thin films for photovoltaic application *Appl. Surf. Sci.* **418** 216–24

[283] Peccerillo E and Durose K 2018 Copper–antimony and copper–bismuth chalcogenides—research opportunities and review for solar photovoltaics *MRS Energy Sustain.* **5** 1–59

[284] Shah K S, Bennett P, Moy L P, Misra M M and Moses W W 1996 Characterization of indium iodide detectors for scintillation studies *Nucl. Instrum. Methods Phys. Res.* A **380** 215–9

[285] Biswas K and Du M-H 2011 First principles study of native defects in InI *J. Appl. Phys.* **109** 113518

[286] Nason D and Keller L 1995 The growth and crystallography of bismuth tri-iodide crystals grown by vapor transport *J. Cryst. Growth* **156** 221–6

[287] Hamdeh U H *et al* 2016 Solution-processed BiI_3 thin films for photovoltaic applications: improved carrier collection via solvent annealing *Chem. Mater.* **28** 6567–74

[288] Podraza N J *et al* 2013 Band gap and structure of single crystal BiI_3: resolving discrepancies in literature *J. Appl. Phys.* **114** 33110

[289] Sellin P J 2006 Thick film compound semiconductors for x-ray imaging applications *Nucl. Instrum. Methods Phys. Res.* A **563** 1–8

[290] Fornaro L, Saucedo E, Mussio L, Gancharov A and Cuña A 2004 Bismuth tri-iodide polycrystalline films for digital x-ray radiography applications *IEEE Trans. Nucl. Sci.* **51** 96–100

[291] Han H *et al* 2014 Defect engineering of BiI_3 single crystals: enhanced electrical and radiation performance for room temperature gamma-ray detection *J. Phys. Chem.* C **118** 3244–50

[292] Du M-H and Singh D J 2010 Enhanced Born charges in III-VII, IV-VII_2, and V-VII_3 compounds *Phys. Rev.* B **82** 45203

[293] Virko S V, Motsnyi F V and Telbiz G M 1998 Absorption diagnostics of quantum size effect on the excited states of SbI_3 clusters in FAU zeolite *Optical Diagnostics of Materials and Devices for Opto-, Micro-, and Quantum Electronics* 3359 (Bellingham, Washington USA: SPIE) 72–4

[294] Mohan D B, Philip A and Sunandana C S 2008 Iodization of antimony thin films: XRD, SEM and optical studies of nanostructured SbI_3 *Vacuum* **82** 561–5

[295] Chen G, Li W, Yu Y and Yang Q 2015 Fast and low-temperature synthesis of one-dimensional (1D) single-crystalline SbSI microrod for high performance photodetector *RSC Adv.* **5** 21859–64

[296] Bhachu D S *et al* 2016 Bismuth oxyhalides: synthesis, structure and photoelectrochemical activity *Chem. Sci.* **7** 4832–41

[297] Sfaelou S, Raptis D, Dracopoulos V and Lianos P 2015 BiOI solar cells *RSC Adv.* **5** 95813–6

[298] Jagt R A *et al* 2020 Controlling the preferred orientation of layered BiOI solar absorbers *J. Mater. Chem.* C **8** 10791–7

[299] Ahmmad B, Kurawaki J, Ohkubo T and Hirose F 2013 TiO_2/TaON-and TiO_2/BiOI-based solid-state solar cells *J. Energy Eng.* **139** 338–42

[300] Huq T *et al* 2020 Electronic structure and optoelectronic properties of bismuth oxyiodide robust against percent-level iodine-, oxygen-, and bismuth-related surface defects *Adv. Funct. Mater.* **30** 1909983

[301] Hahn N T, Self J L and Mullins C B 2012 BiSI micro-rod thin films: efficient solar absorber electrodes? *J. Phys. Chem. Lett.* **3** 1571–6

[302] Wang W, Wang S-Y and Liu M 2005 Growth of rod-like crystal BiSI films by ultrasonic spray pyrolysis *Mater. Res. Bull.* **40** 1781–6

[303] Su X *et al* 2006 A facile and clean synthesis of pure bismuth sulfide iodide crystals *Russ. J. Inorg. Chem.* **51** 1864–8

[304] Zhu L, Xie Y, Zheng X, Yin X and Tian X 2002 Growth of compound BiIII-VIA-VIIA crystals with special morphologies under mild conditions *Inorg. Chem.* **41** 4560–6

[305] Desai C C and Hanchinal A N 1999 Morphological aspects of bismuth sulpho iodide grown by silica gel technique *Asian J. Chem.* **11** 344

[306] Aliev Z S *et al* 2014 The phase equilibria in the Bi—S—I ternary system and thermodynamic properties of the BiSI and $Bi_{19}S_{27}I_3$ ternary compounds *J. Alloys Compd.* **610** 522–8

[307] Kvedaravičius S, Audzijonis A, Mykolaitienė N and Jcancerevičius A 1996 The electronic potential of the V-VI-VII compounds in the region of phase transition *Phase Trans.* **58** 235–46

[308] Wang C *et al* 2001 Synthesis of novel SbSI nanorods by a hydrothermal method *Inorg. Chem. Commun.* **4** 339–41

[309] Nie R *et al* 2018 Efficient solar cells based on light-harvesting antimony sulfoiodide *Adv. Energy Mater.* **8** 1701901

[310] Hyun S-C *et al* 1995 Optical properties of undoped and chromium-doped V A-VI A-VII A single crystals *J. Mater. Sci.* **30** 6113–7

[311] Hamano K, Nakamura T, Ishibashi Y and Ooyane T 1965 Piezoelectric property of SbSI single crystal *J. Phys. Soc. Japan* **20** 1886–8

[312] Butler K T *et al* 2016 Quasi-particle electronic band structure and alignment of the V-VI-VII semiconductors SbSI, SbSBr, and SbSeI for solar cells *Appl. Phys. Lett.* **108** 112103

[313] Szperlich P, Nowak M, Bober Ł, Szala J and Stróż D 2009 Ferroelectric properties of ultrasonochemically prepared SbSI ethanogel *Ultrason. Sonochem.* **16** 398–401

[314] Nako K and Balkanski M 1973 Electronic band structures of SbSI in the para-and ferroelectric phases *Phys. Rev.* B **8** 5759

[315] Steele J A *et al* 2018 Giant electron–phonon coupling and deep conduction band resonance in metal halide double perovskite *ACS Nano* **12** 8081–90

[316] Saitoh A, Komatsu T and Karasawa T 2000 Exciton–phonon interaction and conversion of excitons from free to self-trapped states in layered metal iodide crystals under hydrostatic pressure *J. Lumin.* **87** 633–5

[317] Wright A D *et al* 2016 Electron–phonon coupling in hybrid lead halide perovskites *Nat. Commun.* **7** 11755

[318] Morkoç H 2013 *Nitride Semiconductors and Devices* 32 (Berlin/Heidelberg, Germany: Springer Science & Business Media)

[319] Wolf C, Cho H, Kim Y-H and Lee T-W 2017 Polaronic charge carrier–lattice interactions in lead halide perovskites *ChemSusChem* **10** 3705–11

[320] Zelewski S J *et al* 2019 Revealing the nature of photoluminescence emission in the metal-halide double perovskite $Cs_2AgBiBr_6$ *J. Mater. Chem.* C **7** 8350–6

[321] Marongiu D, Saba M, Quochi F, Mura A and Bongiovanni G 2019 The role of excitons in 3D and 2D lead halide perovskites *J. Mater. Chem.* C **7** 12006–18

[322] Etgar L 2018 The merit of perovskite's dimensionality; Can this replace the 3D halide perovskite? *Energy Environ. Sci.* **11** 234–42

[323] Gregg B A 2003 Excitonic solar cells *J. Phys. Chem.* B **107** 4688–98

[324] Saparov B and Mitzi D B 2016 Organic-inorganic perovskites: structural versatility for functional materials design *Chem. Rev.* **116** 4558–96

[325] Takanabe K 2017 Photocatalytic water splitting: quantitative approaches toward photocatalyst by design *ACS Catal.* **7** 8006–22

[326] Baranowski M and Plochocka P 2020 Excitons in metal-halide perovskites *Adv. Energy Mater.* **10** 1903659

[327] Miyata A *et al* 2015 Direct measurement of the exciton binding energy and effective masses for charge carriers in organic-inorganic tri-halide perovskites *Nat. Phys.* **11** 582–7

[328] Galkowski K *et al* 2016 Determination of the exciton binding energy and effective masses for methylammonium and formamidinium lead tri-halide perovskite semiconductors *Energy Environ. Sci.* **9** 962–70

[329] Hebig J C, Kühn I, Flohre J and Kirchartz T 2016 Optoelectronic properties of $(CH_3NH_3)_3Sb_2I_9$ thin films for photovoltaic applications *ACS Energy Lett.* **1** 309–14

[330] Pal J *et al* 2018 Synthesis and optical properties of colloidal $M_3Bi_2I_9$ (M = Cs, Rb) perovskite nanocrystals *J. Phys. Chem.* C **122** 10643–9

[331] Kawai T and Shimanuki S 1993 Optical studies of $(CH_3NH_3)_3Bi_2I_9$ single crystals *Phys. Status Solidi* **177** K43–5

[332] Maughan A E *et al* 2018 Anharmonicity and octahedral tilting in hybrid vacancy-ordered double perovskites *Chem. Mater.* **30** 472–83

[333] Jong U G, Yu C J and Kye Y H 2019 Computational prediction of structural, electronic, and optical properties and phase stability of double perovskites K_2SnX_6 (X = I, Br, Cl) *RSC Adv.* **10** 201–9

[334] Smith M D and Karunadasa H I 2018 White-light emission from layered halide perovskites *Acc. Chem. Res.* **51** 619–27

[335] Zhang L *et al* 2019 Tuning emission and electron—phonon coupling in lead-free halide double perovskite $Cs_2AgBiCl_6$ under pressure *ACS Energy Lett.* **4** 2975–82

[336] IEC 61215-1-3:2016, IEC Webstore, Terrestrial photovoltaic (PV) modules - Design qualification and type approval - Part 1-3: Special requirements for testing of thin-film amorphous silicon based photovoltaic (PV) modules, retrieved December 13, 2020 (https://webstore.iec.ch/publication/29787)

[337] Khenkin M V *et al* 2020 Consensus statement for stability assessment and reporting for perovskite photovoltaics based on ISOS procedures *Nat. Energy* **5** 35–49

[338] Kim H S *et al* 2012 Lead iodide perovskite sensitized all-solid-state submicron thin film mesoscopic solar cell with efficiency exceeding 9% *Sci. Rep.* **2** 591

[339] Lee M M, Teuscher J, Miyasaka T, Murakami T N and Snaith H J 2012 Efficient hybrid solar cells based on meso-superstructured organometal halide perovskites *Science* **338** 643–7

[340] Stranks S D *et al* 2013 Electron–hole diffusion lengths exceeding 1 micrometer in an organometal trihalide perovskite absorber *Science* **342** 341–4

[341] Liu M, Johnston M B and Snaith H J 2013 Efficient planar heterojunction perovskite solar cells by vapour deposition *Nature* **501** 395–8

[342] Yoo J J *et al* 2019 An interface stabilized perovskite solar cell with high stabilized efficiency and low voltage loss *Energy Environ. Sci.* **12** 2192–9

[343] Tang J *et al* 2018 High-performance inverted planar perovskite solar cells based on efficient hole-transporting layers from well-crystalline NiO nanocrystals *Sol. Energy* **161** 100–8

[344] Sahli F *et al* 2018 Fully textured monolithic perovskite/silicon tandem solar cells with 25.2% power conversion efficiency *Nat. Mater.* **17** 820–6

[345] Han Q *et al* 2018 High-performance perovskite/Cu(In, Ga)Se_2 monolithic tandem solar cells *Science* **361** 904–8

[346] Shen H *et al* 2018 Mechanically-stacked perovskite/CIGS tandem solar cells with efficiency of 23.9% and reduced oxygen sensitivity *Energy Environ. Sci.* **11** 394–406

[347] Chen B *et al* 2020 Enhanced optical path and electron diffusion length enable high-efficiency perovskite tandems *Nat. Commun.* **11** 1257

[348] Manekkathodi A *et al* 2019 Solution-processed perovskite-colloidal quantum dot tandem solar cells for photon collection beyond 1000 nm *J. Mater. Chem.* A **7** 26020–8

[349] Zhao D *et al* 2017 Low-bandgap mixed tin—lead iodide perovskite absorbers with long carrier lifetimes for all-perovskite tandem solar cells *Nat. Energy* **2** 17018

[350] Tong J *et al* 2019 Carrier lifetimes of >1 μs in Sn–Pb perovskites enable efficient all-perovskite tandem solar cells *Science* **364** 475–9

[351] Löper P *et al* 2015 Organic—inorganic halide perovskite/crystalline silicon four-terminal tandem solar cells *Phys. Chem. Chem. Phys.* **17** 1619–29

[352] Jacobs D A *et al* 2019 Light management: a key concept in high-efficiency perovskite/silicon tandem photovoltaics *J. Phys. Chem. Lett.* **10** 3159–70

[353] Werner J *et al* 2016 Efficient near-infrared-transparent perovskite solar cells enabling direct comparison of 4-terminal and monolithic perovskite/silicon tandem cells *ACS Energy Lett.* **1** 474–80

[354] Jošt M *et al* 2018 Textured interfaces in monolithic perovskite/silicon tandem solar cells: advanced light management for improved efficiency and energy yield *Energy Environ. Sci.* **11** 3511–23

[355] Werner J *et al* 2016 Efficient monolithic perovskite/silicon tandem solar cell with cell area >1 cm^2 *J. Phys. Chem. Lett.* **7** 161–6

[356] Snaith H J *et al* 2014 Anomalous hysteresis in perovskite solar cells *J. Phys. Chem. Lett.* **5** 1511–5

[357] Kim H-S and Park N-G 2014 Parameters affecting I–V hysteresis of $CH_3NH_3PbI_3$ perovskite solar cells: effects of perovskite crystal size and mesoporous TiO_2 layer *J. Phys. Chem. Lett.* **5** 2927–34

[358] Christians J A, Manser J S and Kamat P V 2015 Best practices in perovskite solar cell efficiency measurements. Avoiding the error of making bad cells look good *J. Phys. Chem. Lett.* **6** 852–7

[359] Jiang Y *et al* 2019 Reduction of lead leakage from damaged lead halide perovskite solar modules using self-healing polymer-based encapsulation *Nat. Energy* **4** 585–93

[360] Li X *et al* 2020 On-device lead sequestration for perovskite solar cells *Nature* **578** 555–8

[361] Park S Y *et al* 2020 Sustainable lead management in halide perovskite solar cells *Nat. Sustain.* **3** 1044–51

[362] Zhu Z, Chueh C C, Li N, Mao C and Jen A K Y Y 2018 Realizing efficient lead-free formamidinium tin triiodide perovskite solar cells via a sequential deposition route *Adv. Mater.* **30** 1703800

[363] Ke W *et al* 2018 Dopant-free tetrakis-triphenylamine hole transporting material for efficient tin-based perovskite solar cells *J. Am. Chem. Soc.* **140** 388–93

[364] Shao S *et al* 2018 Highly reproducible Sn-based hybrid perovskite solar cells with 9% efficiency *Adv. Energy Mater.* **8** 1702019

[365] Liao Y *et al* 2017 Highly oriented low-dimensional tin halide perovskites with enhanced stability and photovoltaic performance *J. Am. Chem. Soc.* **139** 6693–9

[366] Cao D H *et al* 2017 Thin films and solar cells based on semiconducting two-dimensional Ruddlesden–Popper $(CH_3(CH_2)_3NH_3)_2(CH_3NH_3)_{n-1}Sn_nI_{3n+1}$ *ACS Energy Lett.* **2** 982–90

[367] Jokar E, Chien C-H, Tsai C-M, Fathi A and Diau E W-G 2019 Robust tin-based perovskite solar cells with hybrid organic cations to attain efficiency approaching 10% *Adv. Mater.* **31** 1804835

[368] Lee S J *et al* 2016 Fabrication of efficient formamidinium tin iodide perovskite solar cells through SnF_2-pyrazine complex *J. Am. Chem. Soc.* **138** 3974–7

[369] Zhang Z *et al* 2017 High-quality $(CH_3NH_3)_3Bi_2I_9$ film-based solar cells: pushing efficiency up to 1.64% *J. Phys. Chem. Lett.* **8** 4300–7

[370] Ghosh B *et al* 2018 Limitations of $Cs_3Bi_2I_9$ as lead-free photovoltaic absorber materials *ACS Appl. Mater. Interfaces* **10** 35000–7

[371] Shin S S *et al* 2018 Solvent-engineering method to deposit compact bismuth-based thin films: mechanism and application to photovoltaics *Chem. Mater.* **30** 336–43

[372] Choi Y C, Yeom E J, Ahn T K and Seok S I L 2015 $CuSbS_2$-sensitized inorganic–organic heterojunction solar cells fabricated using a metal–thiourea complex solution *Angew. Chem. Int. Ed.* **54** 4005–9

[373] Claybourn M, Brinkman A W, Russell G J and Woods J 1987 Electron traps in single-crystal CdS *Phil. Mag.* B **56** 385–95

[374] Baciak J E, Nino J C, Qiu W and Lintereur A 2012 *Single-Crystal Bismuth Iodide Gamma-Ray Spectrometers*

[375] Kulkarni A *et al* 2018 Vapor annealing controlled crystal growth and photovoltaic performance of bismuth triiodide embedded in mesostructured configurations *ACS Appl. Mater. Interfaces* **10** 9547–54

[376] Zhang Y *et al* 2015 Mesoporous TiO_2-based photoanode sensitized by BiOI and investigation of its photovoltaic behavior *Langmuir* **31** 10279–84

[377] Hahn N T, Rettie A J E E, Beal S K, Fullon R R and Mullins C B 2012 N-BiSI thin films: selenium doping and solar cell behavior *J. Phys. Chem.* C **116** 24878–86

[378] Ganose A M, Matsumoto S, Buckeridge J and Scanlon D O 2018 Defect engineering of earth-abundant solar absorbers BiSI and BiSeI *Chem. Mater.* **30** 3827–35

[379] Miller O D, Yablonovitch E and Kurtz S R 2012 Strong internal and external luminescence as solar cells approach the Shockley–Queisser limit *IEEE J. Photovolt.* **2** 303–11

[380] Lin K *et al* 2018 Perovskite light-emitting diodes with external quantum efficiency exceeding 20 per cent *Nature* **562** 245–8

[381] Stranks S D, Hoye R L Z, Di D, Friend R H and Deschler F 2019 The physics of light emission in halide perovskite devices *Adv. Mater.* **31** 1803336

[382] Mondal N, De A and Samanta A 2018 Achieving near-unity photoluminescence efficiency for blue-violet-emitting perovskite nanocrystals *ACS Energy Lett.* **4** 32–9

[383] Wu Y *et al* 2018 *In situ* passivation of $PbBr_6^{4-}$ octahedra toward blue luminescent $CsPbBr_3$ nanoplatelets with near 100% absolute quantum yield *ACS Energy Lett.* **3** 2030–7

[384] Zhao B *et al* 2018 High-efficiency perovskite—polymer bulk heterostructure light-emitting diodes *Nat. Photonics* **12** 783–9

[385] Chiba T *et al* 2018 Anion-exchange red perovskite quantum dots with ammonium iodine salts for highly efficient light-emitting devices *Nat. Photonics* **12** 681–7

[386] Shamsi J, Urban A S, Imran M, DeTrizio L and Manna L 2019 Metal halide perovskite nanocrystals: synthesis, post-synthesis modifications, and their optical properties *Chem. Rev.* **119** 3296–348

[387] Hoye R L Z *et al* 2015 Enhanced performance in fluorene-free organometal halide perovskite light-emitting diodes using tunable, low electron affinity oxide electron injectors *Adv. Mater.* **27** 1414–9

[388] Adjokatse S, Fang H-H and Loi M A 2017 Broadly tunable metal halide perovskites for solid-state light-emission applications *Mater. Today* **20** 413–24

[389] Moody N *et al* 2020 Assessing the regulatory requirements of lead-based perovskite photovoltaics *Joule* **4** 970–4

[390] Swarnkar A, Ravi V K and Nag A 2017 Beyond colloidal cesium lead halide perovskite nanocrystals: analogous metal halides and doping *ACS Energy Lett.* **2** 1089–98

[391] Khalfin S and Bekenstein Y 2019 Advances in lead-free double perovskite nanocrystals, engineering band-gaps and enhancing stability through composition tunability *Nanoscale* **11** 8665–79

[392] Ravi V K, Singhal N and Nag A 2018 Initiation and future prospects of colloidal metal halide double-perovskite nanocrystals: Cs_2AgBiX_6 (X = Cl, Br, I) *J. Mater. Chem.* A **6** 21666–75 Initiation and future prospects of colloidal metal halide double-perovskite nanocrystals: Cs2AgBiX (X=Cl, Br, I)6

[393] Sun J, Yang J, Lee J I, Cho J H and Kang M S 2018 Lead-free perovskite nanocrystals for light-emitting devices *J. Phys. Chem. Lett.* **9** 1573–83

[394] Ma Z *et al* 2019 Electrically-driven violet light-emitting devices based on highly stable lead-free perovskite $Cs_3Sb_2Br_9$ quantum dots *ACS Energy Lett.* **5** 385–94

[395] Zhang J *et al* 2017 High quantum yield blue emission from lead-free inorganic antimony halide perovskite colloidal quantum dots *ACS Nano* **11** 9294–302

[396] Leng M *et al* 2018 All-inorganic bismuth-based perovskite quantum dots with bright blue photoluminescence and excellent stability *Adv. Funct. Mater.* **28** 1704446

[397] Tan Z *et al* 2018 Highly efficient blue-emitting Bi-doped Cs_2SnCl_6 perovskite variant: photoluminescence induced by impurity doping *Adv. Funct. Mater.* **28** 1801131

[398] Yang B *et al* 2018 Lead-free direct band gap double-perovskite nanocrystals with bright dual-color emission *J. Am. Chem. Soc.* **140** 17001–6

[399] Han P *et al* 2019 Lead-free sodium—indium double perovskite nanocrystals through doping silver cations for bright yellow emission *Angew. Chem. Int. Ed.* **58** 17231–5

[400] Han P *et al* 2020 Manganese-doped, lead-free double perovskite nanocrystals for bright orange-red emission *ACS Cent. Sci.* **6** 566–72

[401] Lai M L *et al* 2016 Tunable near-infrared luminescence in tin halide perovskite devices *J. Phys. Chem. Lett.* **7** 2653–8

[402] Qiu W *et al* 2019 Mixed lead—tin halide perovskites for efficient and wavelength-tunable near-infrared light-emitting diodes *Adv. Mater.* **31** 1806105

[403] Lanzetta L, Marin-Beloqui J M, Sanchez-Molina I, Ding D and Haque S A 2017 Two-dimensional organic tin halide perovskites with tunable visible emission and their use in light-emitting devices *ACS Energy Lett.* **2** 1662–8

[404] Zhang X *et al* 2018 Bright orange electroluminescence from lead-free two-dimensional perovskites *ACS Energy Lett.* **4** 242–8

[405] Wang W, Tadé M O and Shao Z 2015 Research progress of perovskite materials in photocatalysis-and photovoltaics-related energy conversion and environmental treatment *Chem. Soc. Rev.* **44** 5371–408

[406] Huang H, Pradhan B, Hofkens J, Roeffaers M B J and Steele J A 2020 Solar-driven metal halide perovskite photocatalysis: design, stability, and performance *ACS Energy Lett.* **5** 1107–23

[407] Fujishima A and Honda K 1972 Electrochemical photolysis of water at a semiconductor electrode *Nature* **238** 37–8

[408] Fujishima A 1969 Photosensitized electrolytic oxidation at a TiO_2 electrode *J. Chem. Soc. Japan* **72** 108–13

[409] deKrol R and Grätzel M 2012 *Photoelectrochemical Hydrogen Production* vol 90 (Berlin: Springer)

[410] Grätzel M 2001 Photoelectrochemical cells *Nature* **414** 338–44

[411] Park S S *et al* 2017 Photocatalytic hydrogen generation from hydriodic acid using methylammonium lead iodide in dynamic equilibrium with aqueous solution *Nat. Energy* **2** 16185

[412] Ahmad S *et al* 2019 Triple-cation-based perovskite photocathodes with AZO protective layer for hydrogen production applications *ACS Appl. Mater. Interfaces* **11** 23198–206

[413] Andrei V *et al* 2018 Scalable triple cation mixed halide perovskite—$BiVO_4$ tandems for bias-free water splitting *Adv. Energy Mater.* **8** 1801403

[414] Andrei V, Reuillard B and Reisner E 2020 Bias-free solar syngas production by integrating a molecular cobalt catalyst with perovskite—$BiVO_4$ tandems *Nat. Mater.* **19** 189–94

[415] Murphy A B *et al* 2006 Efficiency of solar water splitting using semiconductor electrodes *Int. J. Hydrog. Energy* **31** 1999–2017

[416] Bhosale S S *et al* 2019 Mechanism of photocatalytic CO_2 reduction by bismuth-based perovskite nanocrystals at the gas-solid interface *J. Am. Chem. Soc.* **141** 20434–42

[417] Lu C *et al* 2020 Synthesis of lead-free $Cs_3Sb_2Br_9$ perovskite alternative nanocrystals with enhanced photocatalytic CO_2 reduction activity *Nanoscale* **12** 2987–91

[418] Wang X-D *et al* 2019 *In situ* construction of a Cs_2SnI_6 perovskite nanocrystal/SnS_2 nanosheet heterojunction with boosted interfacial charge transfer *J. Am. Chem. Soc.* **141** 13434–41

[419] Burton L A *et al* 2016 Electronic and optical properties of single crystal SnS_2: an earth-abundant disulfide photocatalyst *J. Mater. Chem.* A **4** 1312–8

[420] Ke J C R *et al* 2018 Ambient-air-stable inorganic Cs_2SnI_6 double perovskite thin films: via aerosol-assisted chemical vapour deposition *J. Mater. Chem.* A **6** 11205–14

[421] Wang T, Yue D, Li X and Zhao Y 2020 Lead-free double perovskite $Cs_2AgBiBr_6$/RGO composite for efficient visible light photocatalytic H_2 evolution *Appl. Catal.* B **268** 118399

[422] Guo Y *et al* 2019 Stable lead-free $(CH_3NH_3)_3Bi_2I_9$ perovskite for photocatalytic hydrogen generation *ACS Sustain. Chem. Eng.* **7** 15080–5

[423] Pan L *et al* 2018 Boosting the performance of Cu_2O photocathodes for unassisted solar water splitting devices *Nat. Catal.* **1** 412–20

[424] Zhang Z *et al* 2019 Stable and highly efficient photocatalysis with lead-free double-perovskite of $Cs_2AgBiBr_6$ *Angew. Chem. Int. Ed.* **58** 7263–7

[425] Bargozideh S and Tasviri M 2018 Construction of a novel BiSI/MoS_2 nanocomposite with enhanced visible-light driven photocatalytic performance *New J. Chem.* **42** 18236–41

[426] Bu Y, Xu J, Li Y, Liu Q and Zhang X 2017 Enhanced photocatalytic activity of BiOI under visible light irradiation by the modification of MoS_2 *RSC Adv.* **7** 42398–406

[427] Tamilselvan M and Bhattacharyya A J 2016 Antimony sulphoiodide (SbSI), a narrow band-gap non-oxide ternary semiconductor with efficient photocatalytic activity *RSC Adv.* **6** 105980–7

[428] Wang C *et al* 2018 SbSI nanocrystals: an excellent visible light photocatalyst with efficient generation of singlet oxygen *ACS Sustain. Chem. Eng.* **6** 12166–75

[429] McCall K M *et al* 2018 α-Particle detection and charge transport characteristics in the A3M2I9 defect perovskites (A = Cs, Rb; M = Bi, Sb) *ACS Photonics* **5** 3748–62

[430] Kong X Y, Lee W P C, Ong W-J, Chai S-P and Mohamed A R 2016 Oxygen-deficient BiOBr as a highly stable photocatalyst for efficient CO_2 reduction into renewable carbon-neutral fuels *ChemCatChem* **8** 3074–81

[431] Zhang L, Wang W, Jiang D, Gao E and Sun S 2015 Photoreduction of CO_2 on BiOCl nanoplates with the assistance of photoinduced oxygen vacancies *Nano Res.* **8** 821–31

[432] Hahn N T, Hoang S, Self J L and Mullins C B 2012 Spray pyrolysis deposition and photoelectrochemical properties of n-type BiOI nanoplatelet thin films *ACS Nano* **6** 7712–22

[433] Yakunin S *et al* 2016 Detection of gamma photons using solution-grown single crystals of hybrid lead halide perovskites *Nat. Photonics* **10** 585–9

[434] Wei H and Huang J 2019 Halide lead perovskites for ionizing radiation detection *Nat. Commun.* **10** 1066

[435] Gao L and Yan Q 2020 Recent advances in lead halide perovskites for radiation detectors *Sol. RRL* **4** 1900210

[436] He Y *et al* 2019 Perovskite $CsPbBr_3$ single crystal detector for alpha-particle spectroscopy *Nucl. Instrum. Methods Phys. Res.* A **922** 217–21

[437] Schlesinger T E *et al* 2001 Cadmium zinc telluride and its use as a nuclear radiation detector material *Mater. Sci. Eng.* R **32** 103–89

[438] Jeong D-N, Yang J-M and Park N-G 2020 Roadmap on halide perovskite and related devices *Nanotechnology* **31** 152001

[439] Johns P M, Baciak J E and Nino J C 2016 Enhanced gamma ray sensitivity in bismuth triiodide sensors through volumetric defect control *Appl. Phys. Lett.* **109** 92105

[440] Birowosuto M D *et al* 2016 X-ray scintillation in lead halide perovskite crystals *Sci. Rep.* **6** 37254

[441] Guerra M, Manso M, Longelin S, Pessanha S and Carvalho M L 2012 Performance of three different Si x-ray detectors for portable XRF spectrometers in cultural heritage applications *J. Instrum.* **7** C10004

[442] Rikner G and Grusell E 1983 Effects of radiation damage on p-type silicon detectors *Phys. Med. Biol.* **28** 1261

[443] Häcker R and Hangleiter A 1994 Intrinsic upper limits of the carrier lifetime in silicon *J. Appl. Phys.* **75** 7570–2

[444] Lutz G *et al* 2007 *Semiconductor Radiation Detectors* (Berlin: Springer)

[445] Kasap S O 2000 X-ray sensitivity of photoconductors: application to stabilized a-Se *J. Phys. D: Appl. Phys.* **33** 2853

[446] Hunter D M, Belev G, Kasap S and Yaffe M J 2012 Measured and calculated K-fluorescence effects on the MTF of an amorphous-selenium based CCD x-ray detector *Med. Phys.* **39** 608–22

[447] Ivanov Y M *et al* 2003 The possibilities of using semi-insulating CdTe crystals as detecting material for x-ray imaging radiography *Phys. Status Solidi* 840–4

[448] Zhao J *et al* 2017 Strained hybrid perovskite thin films and their impact on the intrinsic stability of perovskite solar cells *Sci. Adv.* **3** eaao5616

[449] Dmitriyev Y N, Bennett P R, Cirignano L J, Klugerman M B and Shah K S 1999 Bismuth iodide crystals as a detector material: some optical and electrical properties *Hard X-Ray, Gamma-Ray, and Neutron Detector Physics* 3768 (Bellingham, Washington USA: SPIE) 521–9

[450] Sun H *et al* 2018 Preparation and characterization of free-standing BiI_3 single-crystal flakes for x-ray detection application *J. Mater. Sci., Mater. Electron.* **29** 20003–9

[451] Saito T, Iwasaki T, Kurosawa S, Yoshikawa A and Den T 2016 BiI_3 single crystal for room-temperature gamma ray detectors *Nucl. Instrum. Methods Phys. Res.* A **806** 395–400

[452] Matsumoto M, Hitomi K, Shoji T and Hiratate Y 2002 Bismuth tri-iodide crystal for nuclear radiation detectors *IEEE Trans. Nucl. Sci.* **49** 2517–20

[453] Chen Q *et al* 2018 All-inorganic perovskite nanocrystal scintillators *Nature* **561** 88–93

[454] Cao J *et al* 2020 Preparation of lead-free two-dimensional-layered $(C_8H_{17}NH_3)_2SnBr_4$ perovskite scintillators and their application in x-ray imaging *ACS Appl. Mater. Interfaces* **12** 19797–804

[455] He Y *et al* 2018 High spectral resolution of gamma-rays at room temperature by perovskite $CsPbBr_3$ single crystals *Nat. Commun.* **9** 1609

[456] Owens A and Peacock A 2004 Compound semiconductor radiation detectors *Nucl. Instrum. Methods Phys. Res.* A **531** 18–37

[457] Yang G *et al* 2015 Study on the properties of high purity germanium crystals. in *J. Phys. Conf. Ser.* **606** 12013

[458] Zhang F *et al* 2012 Characterization of the H3D ASIC readout system and 6.0 cm^3 3D position sensitive CdZnTe detectors *IEEE Trans. Nucl. Sci.* **59** 236–42

[459] Limousin O 2003 New trends in CdTe and CdZnTe detectors for x-and gamma-ray applications *Nucl. Instrum. Methods Phys. Res.* A **504** 24–37
[460] Cho H Y, Lee J H, Kwon Y K, Moon J Y and Lee C S 2011 Measurement of the drift mobilities and the mobility-lifetime products of charge carriers in a CdZnTe crystal by using a transient pulse technique *J. Instrum.* **6** C01025
[461] Amman M S, Lee J S and Luke P N 2001 Alpha particle response characterization of CdZnTe *Hard X-Ray and Gamma-Ray Detector Physics III* 4507 (Bellingham, Washington USA: SPIE) 1–11
[462] Kagan C R, Mitzi D B and Dimitrakopoulos C D 1999 Organic-inorganic hybrid materials as semiconducting channels in thin-film field-effect transistors *Science* **286** 945–7
[463] Zeidell A M *et al* 2018 Enhanced charge transport in hybrid perovskite field-effect transistors via microstructure control *Adv. Electron. Mater.* **4** 1800316
[464] Wu Y *et al* 2016 Organic—inorganic hybrid $CH_3NH_3PbI_3$ perovskite materials as channels in thin-film field-effect transistors *RSC Adv.* **6** 16243–9
[465] Matsushima T *et al* 2016 Solution-processed organic—inorganic perovskite field-effect transistors with high hole mobilities *Adv. Mater.* **28** 10275–81
[466] Gao Y *et al* 2019 Highly stable lead-free perovskite field-effect transistors incorporating linear π-conjugated organic ligands *J. Am. Chem. Soc.* **141** 15577–85
[467] Qian W-H *et al* 2020 Lead-free perovskite $MASnBr_3$-based memristor for quaternary information storage *InfoMat* **2** 743–51
[468] Chua L 1971 Memristor-the missing circuit element *IEEE Trans. Circuit Theory* **18** 507–19
[469] Strukov D B, Snider G S, Stewart D R and Williams R S 2008 The missing memristor found *Nature* **453** 80–3
[470] Han J S *et al* 2019 Lead-free all-inorganic cesium tin iodide perovskite for filamentary and interface-type resistive switching toward environment-friendly and temperature-tolerant nonvolatile memories *ACS Appl. Mater. Interfaces* **11** 8155–63
[471] Mao J-Y *et al* 2020 Lead-free monocrystalline perovskite resistive switching device for temporal information processing *Nano Energy* **71** 104616
[472] Zeng F *et al* 2020 Opportunity of the lead-free all-inorganic $Cs_3Cu_2I_5$ perovskite film for memristor and neuromorphic computing applications *ACS Appl. Mater. Interfaces* **12** 23094–101
[473] Wang H *et al* 2020 Memristive devices based on 2D-BiOI nanosheets and their applications to neuromorphic computing *Appl. Phys. Lett.* **116** 93501
[474] Butler K T, Frost J M, Skelton J M, Svane K L and Walsh A 2016 Computational materials design of crystalline solids *Chem. Soc. Rev.* **45** 6138–46
[475] Kononova O *et al* 2019 Text-mined dataset of inorganic materials synthesis recipes *Sci. Data* **6** 203
[476] Morita K, Davies D W, Butler K T and Walsh A 2020 Modelling the dielectric constants of crystals using machine learning *J. Chem. Phys.* **153** 024503
[477] Momma K and Izumi F 2011 VESTA 3 for three-dimensional visualization of crystal, volumetric and morphology data *J. Appl. Crystallogr.* **44** 1272–6